OPTIMUM CURRENT INJECTION STRATEGY FOR MAGNETIC
RESONANCE ELECTRICAL IMPEDANCE TOMOGRAPHY

HALUK ALTUNEL

FEBRUARY 2008

OPTIMUM CURRENT INJECTION STRATEGY FOR MAGNETIC
RESONANCE ELECTRICAL IMPEDANCE TOMOGRAPHY

A THESIS SUBMITTED TO
THE GRADUATE SCHOOL OF NATURAL AND APPLIED SCIENCES
OF
MIDDLE EAST TECHNICAL UNIVERSITY

BY

HALUK ALTUNEL

IN PARTIAL FULFILLMENT OF THE REQUIREMENTS
FOR
THE DEGREE OF DOCTOR OF PHILOSOPHY
IN
ELECTRICAL AND ELECTRONICS ENGINEERING

FEBRUARY 2008

OPTIMUM CURRENT INJECTION STRATEGY FOR MAGNETIC
RESONANCE ELECTRICAL IMPEDANCE TOMOGRAPHY

submitted by HALUK ALTUNEL in partial fulfillment of the requirements for the degree of Doctor of Philosophy in Electrical and Electronics Engineering Department, Middle East Technical University by,

Prof. Dr. Canan Özgen _____
Dean, Graduate School of Natural and Applied Sciences

Prof. Dr. İsmet Erkmen _____
Head of Department, Electrical and Electronics Engineering

Prof. Dr. B. Murat Eyüboğlu _____
Supervisor, Electrical and Electronics Engineering

Examining Committee Members:

Prof. Dr. Kemal Leblebicioğlu
Electrical and Electronics Engineering Dept., METU _____

Prof. Dr. B. Murat Eyüboğlu
Electrical and Electronics Engineering Dept., METU _____

Prof. Dr. Adnan Köksal
Electrical and Electronics Engineering Dept., Hacettepe University _____

Ass. Prof. Dr. Yeşim S. Doğrusöz _____
Electrical and Electronics Engineering Dept., METU

Ass. Prof. Dr. Çağatay Candan _____
Electrical and Electronics Engineering Dept., METU

Date: 08.02.2008

I hereby declare that all information in this document has been obtained and presented in accordance with academic rules and ethical conduct. I also declare that, as required by these rules and conduct, I have fully cited and referenced all material and results that are not original to this work.

Name, Last Name   :HALUK ALTUNEL

Signature   :

ABSTRACT

OPTIMUM CURRENT INJECTION STRATEGY FOR MAGNETIC RESONANCE ELECTRICAL IMPEDANCE TOMOGRAPHY

Altunel, Haluk

Ph. D., Department of Electrical and Electronics Engineering

Supervisor: Prof. Dr. B. Murat Eyüboğlu

February 2008, 107 pages

In this thesis, optimum current injection strategy for Magnetic Resonance Electrical Impedance Tomography (MREIT) is studied. Distinguishability measure based on magnetic flux density is defined for MREIT. Limit of distinguishability is analytically derived for an infinitely long cylinder with concentric and eccentric inhomogeneities. When distinguishability limits of MREIT and Electrical Impedance Tomography (EIT) are compared, it is found that MREIT is capable of detecting smaller perturbations than EIT. When conductivities of inhomogeneity and background object are equal to 0.8S and 1S respectively, MREIT provides improvement of %74 in detection capacity. Optimum current injection pattern is found based on the distinguishability definition. For 2-D cylindrical body with concentric and eccentric inhomogeneities, opposite drive provides best result. As for the 3-D case, a sphere with azimuthal symmetry is considered. Distinguishability limit expression is obtained and optimum current injection pattern is again opposite drive. Based these results, optimum current injection

principles are provided and Regional Image Reconstruction (RIR) using optimum currents is proposed. It states that conductivity distribution should be reconstructed for a region rather than for the whole body. Applying current injection principles and RIR provides reasonable improvement in image quality when there is noise in the measurement data. For the square geometry, when SNR is 13dB, RIR provides decrement of nearly %50 in conductivity error rate of small inhomogeneity. Pulse sequence optimization is done for Gradient Echo (GE) and it is compared with Spin Echo (SE) in terms of their capabilities for MREIT.

ÖZ

MANYETİK REZONANS ELEKTRİKSEL EMPEDANS TOMOGRAFİSİ İÇİN OPTİMUM AKIM UYGULAMA STRATEJİSİ

Altunel, Haluk

Doktora, Elektrik ve Elektronik Mühendisliği Bölümü

Tez Yöneticisi: Prof. Dr. B. Murat Eyüboğlu

Şubat 2008, 107 Sayfa

Bu tezde, Manyetik Rezonans Elektriksel Empedans Tomografisi (MREIT) için optimum akım uygulama stratejisi üzerinde çalışılmıştır. Manyetik akı yoğunluğunu temel alarak MREIT için ayırt edilebilirlik tanımlanmıştır. Sonsuz uzunluktaki bir silindir ve içindeki merkezi ve merkez dışında konumlanmış yabancı cisimler için ayırt edilebilirlik sınırı analitik olarak elde edilmiştir. Ayırt edilebilirlik limitleri MREIT ve Elektriksel Empedans Tomografisi (EIT) için karşılaştırıldığı zaman MREIT nin daha küçük yabancı cisimleri fark edebilme kapasitesine sahip olduğu bulunmuştur. Yabancı cisim ve arka plan objesinin iletkenlikleri sırasıyla 0.8S ve 1S olduğu durumda, MREIT bulma kapsitesinde %74 oranında iyileşme sağlar. En iyi akım verme yöntemi ayırt edilebilirlik temel alınarak bulunmuştur. 2 boyutlu silindirik cisim ve içindeki merkezi ve merkez dışında konumlanmış yabancı

cisimler için zıt kutuplu akım verme yöntemi en iyi sonucu vermiştir. 3 boyutlu cisim olarak küre düşünülmüştür. Ayırt edilebilirlik limitinin ifadesi bulunmuş ve en iyi akım verme yönteminin yine zıt kutuplu akım verme yöntemi olduğu ortaya çıkarılmıştır. Bu sonuçlardan yola çıkarak optimum akım verme prensipleri belirlenmiş ve optimum akımları kullanan Bölgesel Görüntü Oluşturma (RIR) yöntemi önerilmiştir. Buna göre iletkenlik dağılımı tüm cisim yerine bölgesel olarak oluşturulmalıdır. Akım verme prensiplerini ve RIR yöntemini uygulamak ölçümde gürültü olması durumunda önemli iyileştirme sağlamıştır. Kare bir geometri için, SNR 13 dB olduğu durumda, RIR, iletkenlik hata oranında yaklaşık %50 oranında düşüş sağlar. Gradyant Eko (GE) için darbe dizilim optimizasyon problemi çözülmüş ve bunun Spin Eko (SE) ile MREIT deki kapasiteleri yönüyle kıyaslaması yapılmıştır.

Anahtar Kelimeler: Ayırt Edilebilirlik, Elektriksel Empedans Tomografisi, Manyetik Rezonans, En İyi Akım Verme Yöntemi, Gradyant Eko

To My Family

ACKNOWLEDGEMENTS

TABLE OF CONTENTS

LIST OF TABLES

LIST OF FIGURES

xv

CHAPTER 1

INTRODUCTION

Conductivity differences between tissues and conductivity changes during physiological events have made conductivity imaging as an interesting and popular imaging modality among researchers. Apart from monitoring healthy tissues with a new parameter, anomaly detection is another focus of conductivity imaging.

Conductivity imaging techniques have been evolved for monitoring the earth strata in 1930s [1]. Then these techniques were adapted to medical field in the form of Electrical Impedance Tomography (EIT). EIT is a conductivity imaging modality based on application of a current to a subject and measurement of the surface potentials. Many methods have been developed based on this principle [1]-[5]. Later to improve conductivity imaging, magnetic flux density measurement of magnetic resonance imaging (MRI) system is employed together with potential measurements of EIT system. This new modality is called as Magnetic Resonance Electrical Impedance Tomography (MREIT). Nowadays, MREIT is the focus of the some researchers that work on conductivity imaging [6]-[10].

Distinguishability is a measure of ability for detecting an inhomogeneity in a conductor object. It is used to compare different modalities and it is the heart of the current optimization problems in EIT [11], [12].

Application of current on subject is the first step of both EIT and MREIT. Although many options exist to take into account in current injection; in literature few studies on the current optimization in EIT and MREIT theme can be found. Thus, this thesis is focused to determine optimum current injection strategies for

MREIT. During this study, the answers to following questions were looked for:
"What is the best current injection pattern?",
"What is the effect of number of electrodes in MREIT?",
"What are the best positions of electrodes on the body surface?",
"What is the effect of electrode size on the resultant image quality?"

The literature, research can be classified under three main headings. The first part aims to review the Electrical Impedance Tomography (EIT) and conductivity reconstruction algorithms based on EIT. The second part aims to review the magnetic flux density measurement based conductivity imaging techniques especially Magnetic Resonance Electrical Impedance Tomography (MREIT). The final part concentrates on the distinguishability concept which plays a crucial role in current injection optimization problems of EIT based imaging modalities.

1.1.   Electrical Impedance Tomography (EIT)

Conductivity imaging was first emerged in 1930s for determining different layers of earth strata [1]. Similar to medical EIT problem, current is applied to the earth surface and resultant potential is measured. To reach better conductivity imaging, different algorithms were proposed and electrode locations on the surface were searched [13], [14].

In vivo conductivity distribution of human body can be used as a new imaging method of tissues by medicine especially in anomaly detection and monitoring of impedance related physiological events. EIT is an emerging technique aiming to reconstruct conductivity distribution by generating current distribution inside the body and then measuring the resultant surface potential values. There are two ways of generating a current distribution inside a subject such as direct injection to surface of the subject called as injected-EIT and induction due to coils near the subject surface, called as induced-EIT [15]. In the following subsections, injection and induction will be considered further by giving their underlying principles. Before analyzing these two approaches separately, the basic principles of EIT will be taken into account.

To find the inner conductivities for all points in a subject precisely, one should know the inside current densies and potential distributions. Then with the help of Ohm's Law, conductivities can be obtained. In reality, problem is not so simple and only known parameters are the current injection or induction modality and surface potentials. Therefore finding conductivity distribution has been handled as an inverse problem. Moreover, conductivity reconstruction is a non-linear problem due mainly to dependence of internal current paths on unknown conductivity distribution [16].

1.1.1. Mathematical formulation of EIT

To make the analysis manageable, there exist several assumptions and these are also accepted by the recent researchers [1]. Assumptions are as follows:

- Quasi-static condition applies. This assumption includes the following tails:
  - ➤ Wavelength of the electric field in the region is large compared to the dimension of the body. Then current is independent of time [17].
  - ➤ Impedance is purely real that means capacitive and inductive effects are negligible [17].
- There are no electric sources at the same frequency level of applied current within the region.
- Conductivity is isotropic.
- Conductivity is independent of current density.

Now, consider a subject with volume Ω and surface S. Ω has a given conductivity distribution $\sigma(x,y,z)$. The assumptions that are mentioned above are considered to hold. Then potential $V(x,y,z)$ and current density $\vec{J}(x,y,z)$ satisfies

$$\nabla \cdot \vec{J} = 0 \text{ in } \Omega \tag{1.1}$$

$$\vec{J} = -\sigma \nabla \cdot V$$

$$\text{therefore } \nabla \cdot \sigma \nabla V = 0. \tag{1.2}$$

On the other hand, normal component of the current on the surface is continuous, and then one can write

$$-\sigma \frac{\partial V}{\partial n} = j_n \tag{1.3}$$

where

j_n: external current pattern that is applied to the surface.

When Equation (1.1) and (1.3) are combined, the governing equation set for EIT concept is obtained:

$$\nabla \cdot \sigma \nabla V = 0 \qquad\qquad (1.4.a)$$

$$-\sigma \frac{\partial V}{\partial n} = j_n . \qquad\qquad (1.4.b)$$

Above equation set forms a Neumann type boundary value problem.

1.1.2.   Types of EIT

As mentioned previously, EIT can be classified into two categories as injected and induced current EIT. These will be explained next.

1.1.2.1   Injected current EIT

In this modality, electrodes are placed on the body surface to inject currents and potentials are measured [1]-[5]. The current passing through the body creates a current density distribution inside. This distribution implies a potential distribution inside and at the surface of the body. Different conductivity distributions cause different potential distributions as well as surface potentials.

1.1.2.2   Induced current EIT

In this modality, induction of current using a coil or a set of coils is employed as the source of current and potential distribution [15], [18]. To obtain independent potential distributions, for the single coil case, position of the coil according to the object is changed. In order to satisfy the independent surface potentials, discrete coil structure have been proposed [19]. In this structure, by changing the currents in the coils, one can obtain different current distributions inside the subject and potential distribution as well. Researchers have attempted the problem from the simple structure in 2-D as the concentric inhomogeneity in the circular object [15], [19]. For the eccentric inhomogeneity case, multiple discrete coil structure was applied [20]. A nonlinear optimization problem is formulated to maximize the difference between surface potentials when the inhomogeneity is present and not present while limiting the peak coil current and keeping the applied power constant. It is found

that cosine pattern is the best current for the limited power case and opposite pattern provides the higher difference between surface potentials for the limited current case.

1.1.3. Recent investigations on EIT

Injected-current EIT methods are dominant in the literature and these will be examined in the following parts according to their special topics.

1.1.3.1 Accuracy of EIT

The accuracy of the EIT is investigated for a realistic head model [21]. Sensitivity to a change in the conductivity is analyzed and it is found out that conductivity change in the inner compartment affects the surface potentials less than the outer compartments. Sensitivity to additional tumor is analyzed and it is showed that location of tumor and electrodes affect surface potentials and detect ability of the tumor. Conductivity estimation of compartments shows that structures close to the outer surface can be estimated better than the internal structures.

1.1.3.2 A priori information in EIT

Knowledge on geometrical shape, tissue resistivity range and instrumentation noise can be employed to improve the accuracy in the reconstructed values of tissue resistivity [22]. In the same work, minimum mean square error estimator (MIMSEE) is found to have better performance than least squares error estimator (LSEE) in terms of error performance. However, MIMSEE employs the priori information mentioned above. A similar analysis is conducted with the application of current between all of the opposite electrodes [23]. Increasing the number of applied drives makes the error performance better when compared to the single drive case.

1.1.3.3 Adaptive current tomography

An adaptive approach for determining the best current pattern to maximize the distinguishability is proposed [4], [5]. As the current pattern database, different drives are considered. The algorithm tests all of these drives and finds out which one maximizes the distinguishability. The drives are chosen as the same maximum absolute value. For the concentric cylindrical inhomogeneities, cosine pattern

provides the better result while adjacent current injection approach provides the poorest results.

A microcomputer based EIT was designed by Newell *et al* [3]. This system applies current at 15KHz and employs 32 electrodes for current injection as well as potential measurements. It has the capability of distinguishing 9mm diameter inhomogeneity in a 30cm diameter body. It realizes the adaptive current application methodology of the same research group [4], [5].

1.1.3.4   Anomaly location with EIT

Kwon *et al* introduced an EIT based algorithm for estimation of location and size of the perturbation [16]. In this approach, location of the inhomogeneity is found by a weighted combination of injection current and potentials on the boundary. In this modality, uniform electric field inside the subject with a current injection pattern is created. Furthermore, the algorithm is applied to multiple anomalies and it estimates the center of mass of the anomalies with a reasonable accuracy. However, uniform electric field requirement limits the application of the algorithm to arbitrary conductivity distribution.

1.1.3.5   Regularization in EIT

The relation between conductivity and surface potential is governed by Maxwell's equations, hence the relation is non-linear. In literature, many approaches are developed to deal with this non-linear structure mainly by explicit formulation of the potential as a function of conductivity distribution (forward problem) and inverting the formulation to find out conductivity distribution based on potential values [24], [25]. Inverse relation between conductivity and potential is not in closed form and therefore iterative modalities are employed [24]. Linearization of the forward problem is also used for the same situation [26]. In addition to linearization of the governing equations, regularization techniques are adopted to deal with the attenuation problem of EIT [27]. The attenuation problem is due to scattering in the body. Hence surface potentials contain more information about the conductivity of outer regions than inner structures.

1.2. Magnetic Resonance Electrical Impedance Tomography (MREIT)

As mentioned in the previous section, the sensitivity of surface potential measurements to inner regions is low, therefore EIT is incapable of reconstructing precisely the deeper conductivities in the body and unable to detect the conductivity perturbations. This situation causes low spatial resolution and unsatisfactory accuracy. To obtain high resolution conductivity images, an alternative method based on the measurement of the inner magnetic flux density is proposed by Zhang [6]. This new approach employs magnetic resonance imaging (MRI) technique to obtain inner magnetic flux density values. Together with EIT measurements, this new technique is named as Magnetic Resonance Electrical Impedance Tomography (MREIT). This modality is capable of providing higher conductivity resolution and better sensitivity to inner conductivity perturbations.

In the following subsection, Magnetic Resonance Current Density Imaging (MRCDI) will be examined first, because it is the basis of MREIT. Then different MREIT techniques will be considered according to their basis as current density based namely J-based and magnetic field based namely H-based.

1.2.1. Magnetic Resonance Current Density Imaging (MRCDI)

Based on magnetic flux density measurements, current density $\vec{J}$ distribution can be reconstructed. This imaging modality is called magnetic resonance current density imaging (MRCDI) and the concept was introduced by Scott *et al* [28].

In MRCDI, similar to EIT, current is injected from the surface. Injected current causes a magnetic flux density ($\vec{B}$) distribution inside. Incremental phase (Φ) of magnetic resonance imaging system is proportional to the magnetic flux density created by injected current. Hence, magnetic flux density distribution inside the body due to the injected current can be determined. On the other hand, as in EIT, quasi-static condition is assumed to hold in the mathematical model of the MRCDI reconstruction modality. Then current density and magnetic flux density are related through Maxwell's relation, as follows:

$$\vec{J} = \nabla \times \vec{H} = \nabla \times \frac{\vec{B}}{\mu} \qquad (1.5)$$

where

$\vec{H}$: magnetic field

μ : permeability.

In theory, it is possible to solve Equation (1.5) for $\vec{J}$. However to be able to handle Equation (1.5), $\vec{B}$ should be measured in three dimensions as $\vec{B}_x$, $\vec{B}_y$, and $\vec{B}_z$. This requires either rotation of the body or magnet of the MRI system. This difficulty is later overcome and in a new MRCDI technique, measurement of only one component of magnetic flux density is enough [29], [30]. This new approach employs two current injection patterns that create not collinear current density inside. Moreover, in MREIT, many techniques are developed based on the same principle to eliminate the need to rotate the body and they will be taken into account in the following subsection. On the other hand, images of uniform and non-uniform current densities are reconstructed successfully by MRCDI for conductor phantoms [31], [32].

1.2.2.   MREIT techniques

In addition to MRCDI, peripheral potential values are measured due to injected current and MREIT conductivity reconstruction modality is established. MREIT can either use magnetic field $\vec{H}$ or current density $\vec{J}$ in addition to surface potential measurements. In the following parts, MREIT will be analyzed as magnetic field and current density based modalities.

1.2.2.1   J-Based MREIT techniques

An algorithm that employs internal current density and surface potential measurements is introduced [6]. The potential difference between two points on the surface is related to the internal current density as:

$$V_d = \int_C \rho \vec{J} \cdot d\vec{l} \qquad (1.6)$$

where

V_d : potential difference between two surface points

C : arbitrary path connecting these surface points

ρ : resistivity.

When different paths are used between the same surface points and when the above procedure is repeated for different surface point pairs, a set of equations are obtained where the unknown is the internal resistivity values. Although this modality is valid for 2-D and 3-D imaging problems, it requires too many surface potential measurements to obtain more linearly independent equations and consequently higher resolution and better accuracy.

Another conductivity reconstruction algorithm was proposed based on minimizing the error between internal current density obtained by MRCDI and calculated by Finite Element Method (FEM) [7]. However, conductivities obtained by this method are not correct. This technique was further developed [9], [33]. This new modality employs two current injection strategies which create anti-parallel current density distribution as

$$\left| J^1 \times J^2 \right| \neq 0. \tag{1.7}$$

To satisfy Equation (1.7), current is applied from north-south and west-east directions in this iterative approach. This modality is applied to saline phantoms and magnetic field density distribution is measured by a 0.3T MRI system. Denoising and signal processing techniques are employed in addition to J-substitution algorithm in order to improve the accuracy and resolution of the resultant images.

Another group has presented the magnetic resonance conductivity imaging based on the fact that magnetic field due to injected current can be reconstructed from the phase images of MRI and they have applied this technique to real experimental data [34], [35]. Later, potential measurements from EIT and magnetic flux density measurements from the MRI were combined together to obtain conductivity distribution inside the body [36]-[39]. Furthermore, they have presented the Current Constrained Voltage Scaled Reconstruction (CCVSR) algorithm [10]. In this modality, peripheral potential measurements are used to scale the conductivity distribution. Although it is in the core similar to the J-substitution algorithm, it employs eight current injection patterns and in the same study, the performance of

the different current injection strategies are compared under different constraints such as same total power (SP), same maximum (SM) and same total current (ST). Cosine current injection pattern provides better results when SP and SM are concerned, while the opposite current injection pattern performs better when ST case is considered. According to the existing patient auxiliary current safety regulations, total current that can be applied is limited [12]. Therefore, ST is a more reasonable reference when different current patterns are compared. Based on this fact, the authors have suggested the usage of the opposite drive with eight rotations. A sensitivity matrix based reconstruction technique is employed in order to eliminate the need to body rotation [30]. Saline phantom with more conductor region at the centre has been reconstructed with reasonable error performance.

Non-iterative reconstruction algorithms based on equipotential lines are proposed [8], [40], and [41]. In this approach, current density in the body is created by only one current injection pattern and its distribution is measured by MRCDI. Underlying fact in this method is that current lines and equipotential lines are orthogonal for isotropic conductivity distributions. By finding the equipotential lines, potential distribution inside the body can be found by projecting the surface potential measurements into the field of view (FOV) along equipotential lines. Hence, intersection of the current lines and the equipotential lines form a grid. The relation between current density and potential at the grid points can be stated as follows

$$\vec{j}(x,y,z) = \sigma(x,y,z)\nabla\phi(x,y,z) \qquad (1.8)$$

where

$\vec{j}(x,y,z)$: local current density

$\sigma(x,y,z)$: local conductivity

$\phi(x,y,z)$: local potential.

In Equation (1.8), $\vec{j}(x,y,z)$ is measured by MRCDI, ϕ and $\nabla\phi$ are calculated as explained above. Then, for all local grid points, σ can be found.

Current density distribution due to injected dc current can be reconstructed by magnetic resonance imaging [28], [42]. Similarly injected RF current distribution inside the body can be measured by MRI [43]. In both cases, measurement of magnetic flux density distribution due to current pattern is the first step of the reconstruction. Current density distribution is reconstructed according to Maxwell's relation between current density and magnetic flux density as in Equation (1.5). Moreover, current injection is synchronized with the magnetic resonance pulse sequence. Later, it has been showed that AC currents can be measured by using MRI [44], [45]. Burst sine wave in audio frequency range is applied synchronously with the magnetic resonance pulse sequence. Current is not directly injected on the surface rather passed through an external wire. For 100Hz and 200Hz sine waves, internal ac magnetic flux density and though current density distribution is successfully reconstructed.

Recently, some new MREIT modalities were introduced. The first one utilizes the method of characteristics and it reconstructs the conductivity distribution inside a body apart from a multiplicative constant by applying two current injection patterns given some uniqueness conditions are satisfied [46].

For the following differential equation

$$\vec{A}.\nabla u = b \qquad (1.9)$$

where

$\vec{A}$: vector field

b : scalar field.

Then characteristic curve is given by

$$x'(s) = A(x(s)) \qquad (1.10)$$

$$x(s) = x(s_0) + \int_{s_0}^{s} A(x(t))dt \qquad (1.11)$$

$$u(s) = u(s_1) + \int_{s_1}^{s} u(x(t))dt \qquad (1.12)$$

where $x(s_0)$ and $u(s_1)$ are known. u can be recovered along the characteristic curve in Equation (1.12), when it is known at a point on this curve. In this work,

equipotential lines are shown to be characteristic curves and when a conductivity value on an equipotential line is known all values along this line can be calculated. When two current patterns which are transverse to each other are applied, then only one resistivity value in the body is sufficient to reconstruct all conductivity values. Although this method seems to be challenging, the underlying logic is the same as the previous MREIT algorithms that employed two current injection strategies. Moreover, this method adds up all the error along integration line. When real applications are concerned, knowing the conductivity on the surface is enough to determine the inner conductivities according to this modality. However, error addition characteristic worsens the inner conductivity values and decreases the resolution.

The second modality is named as gradient B_z decomposition algorithm [47]. Although the general procedure of the modality is similar to the previous MREIT algorithms, in this algorithm, current density is decomposed as

$$J = \nabla w + \nabla W \tag{1.13}$$

where

$$J := (-J_y, J_x, 0).$$

With this decomposition, MREIT equations re-evaluated and at the end it is claimed that such decomposition improves the noise tolerance and generality of the algorithm. However, physical meanings of w and W are not provided and under what conditions Equation (1.13) holds, is missing.

1.2.2.2   H-Based MREIT techniques

It is also possible to reconstruct the conductivity distribution from measured magnetic flux density data without calculating the current distribution inside [34], [45]. In this type of reconstruction, measurement of only a single component of magnetic field is enough because there is no need to take the curl of the magnetic field to find the current density. However, J-based algorithms are much preferred by the researchers due its ability to employ Ohm's law when potential data is available and current density distribution is alone an imaging modality.

1.2.3.   Recent investigations on MREIT

Although new MREIT algorithms are developed recently, some of the studies are focused on extending the capabilities of existing algorithms. Minimizing the injected current is one of the main research interests and obtaining high resolution with lower currents attracts MREIT scientists.

1.2.3.1   New algorithms

Equipotential projection-based MREIT is developed based on the fact that current and equipotential lines are orthogonal to each other [48]. This algorithm is composed of determining the surface potentials, obtaining equipotential lines by projecting surface potentials, obtaining current density distribution by MRCDI and calculating conductivity at each pixel based the following equation

$$\sigma(x,y) = \frac{|J(x,y)|}{|\nabla \phi(x,y)|}.$$

(1.14)

This algorithm is not iterative and thus faster. Since conductivity is calculated for each pixel and errors of neighboring pixels do not affect others. However, any possible error in projecting equipotential lines can propagate.

Response surface methodology (RSM) MREIT algorithm utilizes RSM technique for optimizing the conductivity distribution through minimizing the error between calculated and measured magnetic flux density data [49]. Only one component of the magnetic flux density is utilized and surface potential measurements are not used in this modality.

Sensitivity matrix based modality defined by Birgül *et al* [30] is further developed by utilizing conjugate gradient solver (CGS) instead of truncated SVD [50]. Moreover Tikhonov regularization is used and algorithm is iterated. By this way requirement of large decomposition matrices is eliminated and faster imaging is obtained and accuracy for larger conductivity perturbations is improved. Peak current of 1mA is used for injection and resolution and accuracy are improved.

1.2.3.2   Noise estimation in MREIT

Noise estimation methods are proposed as deriving an expression for the standard deviation of magnetic flux density data in MREIT [51] as

$$sd(B_z) = \frac{1}{\sqrt{2}\gamma T_c \Upsilon_M} \tag{1.15}$$

where

γ : gyromagnetic constant

T_c : current pulse width

Υ_M : SNR of the magnitude image.

Standard deviation of B_z values as less than 0.25 and 0.05nT are measured from 3 and 11T MREIT systems with current magnitude of 10mA and $T_c = 16ms$. Higher SNR values are obtained when higher field strength magnets are used in MR. Based on this fact, 11T MRI system is utilized in MREIT [52]. With this magnet, conductivity imaging of biological tissues are tried with different injected currents. Reasonable conductivity images are obtained with minimum current of 5mA.

1.2.3.3   Pulse sequence in MREIT

So far in MREIT studies, mostly spin echo pulse sequence has been used that was proposed by Joy et al [53] and modified by Mikac et al [54]. Current is injected in this pulse sequence. When current application overlaps with slice-selection or readout gradients, slice or readout distortions occur [55]. Then current could be applied between slice selection and readout periods. On the other hand, noise level is inversely proportional to width of the current injection pulse. As mentioned previously decreasing application current level is also targeted in MREIT studies. Therefore, optimization of current injection time becomes crucial. Based on the noise standard deviation defined in Equation (1.15), optimum current injection and data acquisition times are calculated for spin echo pulse sequence by Lee et al [56] as

$$T_s^* = T_c^* = \frac{2}{3}\left(T_E - \frac{3\tau_{rf}}{2}\right) \tag{1.16}$$

where

T_s^* : optimum data acquisition time

T_c^* : optimum current injection time

T_E : echo time

τ_{rf} : RF pulse time.

Injection current nonlinear encoding (ICNE) pulse sequence is proposed by Park *et al* [57]. In this pulse sequence, injection current pulse is extended to the end of reading gradient. Injection current during reading period disturbs gradient linearity. This problem is overcome by measuring conventional and extended signals together with Taylor expansion for linearization. In the same study, it is claimed that extending current injection time in this way, reduces noise up to %24. Noise analysis is done for ICNE method by Kwon *et al* [58]. In obtaining noise standard deviation of B_z, some approximations are made including Taylor series expansion and standard deviation of noise in ICNE is found 42.3% smaller than conventional MREIT pulse sequence. However, with experiments this result is not proved. Experimental outcomes provide in some cases conventional way is better and in other cases ICNE provides about 20% reduction in noise level in the expense of undesirable side effects such as blurring and chemical shift which decrease image quality.

1.3. Distinguishability

Distinguishability is a way of measuring the ability of n imaging system to distinguish between different conductivity distributions and it is applied to EIT modality [2]. For this specific case, it is defined as the ratio of norm of the potential difference measured on the surface and norm of the applied current. When current is kept constant, two conductivity distributions σ_1 and σ_2 are said to be distinguishable if the difference between the surface potentials is greater than the measurement precision; mathematically it is stated as follows

$$\left\| V(\cdot; \sigma_1; j) - V(\cdot; \sigma_2; j) \right\| > \varepsilon \tag{1.17}$$

where ε is the precision degree.

Distinguishability definition is used to find the optimum current injection strategies. These problems are formulated as "Which injection pattern provides the greater difference between surface potentials?" or "Which injection pattern can detect the smallest inhomogeneity in a given object?" provided that injected current satisfies some conditions. When same maximum current value is the condition, then based on Equation (1.17) cosine injection pattern provides better results than opposite drive case [2]. When same applied power condition is considered, similar to the previous case, cosine performs slightly better than the opposite drive topology [11]. However, in a more realistic approach, same total injected current is considered, because existing patient auxiliary current safety regulations limit the total current that can be applied to the patient [12]. In this case, opposite drive reaches a better distinguishability level than the cosine case.

Different norm definitions are employed for distinguishability definition [11]. In the same study, distinguishability definition in continuous model is extended to the discrete electrode model. On the other hand, an adaptive algorithm is introduced that tries to find the best current injection strategy based on the same distinguishability concept [4], [5]. In these pioneer studies, concentric inhomogeneities are considered and potential difference and though distinguishability is calculated from the presence and non-presence of such an inhomogeneity concentrically. Köksal and Eyüboğlu [59] have extended the distinguishability and current optimization issues to the eccentric inhomogeneities by employing conformal transformation. Moreover, it is shown in the same study that opposite current injection pattern performs better both in concentric and eccentric cases and detects smaller inhomogeneities provided that total current is limited. The same idea is applied to induced-current EIT case and parallel results to injected-current EIT are found. For concentric inhomogeneity, cosine topology performs better when same total power constraint is considered and opposite drive provides superior results for the limited coil current case [19].

1.4. Outline of the Thesis

In Chapter 2, general distinguishability definition for MREIT is given first. In the same chapter, analytical expression of the distinguishability measure is calculated for a 2-D cylindrical body with concentric inhomogeneity. Eccentric inhomogeneity case for the same subject is solved with the help of conformal transform. In Chapter 3, optimum current injection pattern is searched for a 2-D cylindrical body with concentric and eccentric perturbations. Current application patterns are also provided. In Chapter 4, distinguishability problem is extended to 3-D geometries and specifically sphere with concentric spherical inhomogeneity is considered. In Chapter 5, Regional Image Reconstruction (RIR) is proposed for MREIT based on optimum current injection pattern. Error performances of conventional conductivity reconstruction techniques and regional image reconstruction utilization are compared. In Chapter 6, current optimization is made for gradient echo pulse sequence. Spin Echo (SE) and Gradient Echo (GE) are compared in terms of their ability to decrease applied current in MREIT. The thesis concludes with Chapter 7 and final conclusions and future work are stated there.

CHAPTER 2

DISTINGUISHABILITY IN MREIT

2.1. Introduction

Definition of a distinguishability measure which states the necessary criterion to optimize the probing current pattern in Magnetic Resonance Electrical Impedance Tomography (MREIT) is an important concept. Distinguishability measure for electrical impedance tomography (EIT) is defined by Isaacson which is based on the finite precision of surface potential measurements [2]. Presence of an inhomogeneity should cause a measurable change in the surface potentials in order to be distinguishable. This definition is based on the surface potentials because it is the only measurable output quantity in EIT. Cosine current pattern is found to be the best for 2-D circular body with concentric circular inhomogeneity according to this definition [2]. In 1987, an adaptive system based on iteratively determining the best current pattern with finite number of electrodes was reported by Gisser *et al* [4]. Based on this approach, cosine pattern provides the best performance for concentric inhomogeneity [5], [11]. Cheney *et al* further developed the distinguishability definition, by employing different norms [11]. Moreover, it was shown that by keeping the dissipated power constant, one can obtain the best results with cosine current injection pattern for the concentric case. It is shown that the best current injection strategy depends on the constraint imposed on the current. Opposite current injection pattern is shown to be the best when total injected current is kept constant [12]. This result is important because current patient safety regulations put a limit to the total current that can be injected to a patient. Lionheart *et al* also compared different constraints on current and suggested that limiting the current on each electrode to a safe level as the constraint is a proper choice for many applications [60].

In Section 2.2, definition of magnetic flux density based distinguishability is stated. Then this definition is applied to 2-D cylindrical body with concentric inhomogeneity in Section 2.3. Surface potential based and magnetic flux density based distinguishabilities are compared for 2-D cylindrical case in Section 2.4. Analytical expression for 2-D cylindrical body with eccentric inhomogeneity is obtained in Section 2.5.

2.2. Definition of the Magnetic Flux Density Based Distinguishability Measure

In MREIT, conductivity distributions are reconstructed using magnetic flux density distribution induced by current flow. Surface potential measurements may be used to scale this distribution. Since magnetic flux density is the primary measured quantity in MREIT, distinguishability measure is referenced directly to magnetic flux density. The relation between a quasi-static current density and magnetic flux density is given as:

$$\vec{J} = \frac{\nabla \times \vec{B}}{\mu_0} \tag{2.1}$$

where

$\vec{J}$: current density

$\vec{B}$: magnetic flux density

μ_0 : permeability of the free space

and $\vec{B}$ can be calculated by Biot-Savart relation as:

$$\vec{B} = \frac{\mu_0}{4\pi} \int \frac{\vec{J}.ds \times \hat{a}_R}{R^2} \tag{2.2}$$

where

R : distance between source and observation points

$\hat{a}_R$: unit vector from source to observation point.

Magnetic flux density is a function of position, conductivity distribution and current density.

Two conductivity distributions namely σ_1 and σ_2 are distinguishable with precision ε iff:

$$\left\| \vec{B}(\bullet, \sigma_1, j) - \vec{B}(\bullet, \sigma_2, j) \right\| > \varepsilon .\qquad(2.3)$$

Above definition states that if the difference between magnetic flux density measurements of two different conductivity distributions is not greater than the measurement precision, then these two conductivity distributions cannot be differentiated by the MREIT system. This definition is valid for both 2-D and 3-D distributions.

In the next section, distiguishability function is formulated for a simple but an illustrative 2-D case, with cylindrical concentric inhomogeneity in order to gain further insight into the magnetic flux density based distinguishability. Then, distinguishability measures with potential and flux density measurements are compared.

2.3.   2-D Cylindrical Body with Concentric Inhomogeneity

Consider infinitely long cylinders with uniform conductivity along the longitudinal direction as shown in Figure 2.1. These assumptions simplify the analytical derivation and convert the original 3-D problem into a 2-D one. Let σ_1 and σ_2 be two conductivity distributions as:

$$\sigma_1 = \begin{cases} 1, & \text{for } \rho < r < 1 \\ \sigma, & \text{for } 0 < r < \rho \end{cases}\qquad(2.4.a)$$

and

$$\sigma_2 = 1, \text{ for } 0 < r < 1\qquad(2.4.b)$$

where ρ represents the radius of inhomogeneity as shown in Figure 2.1.
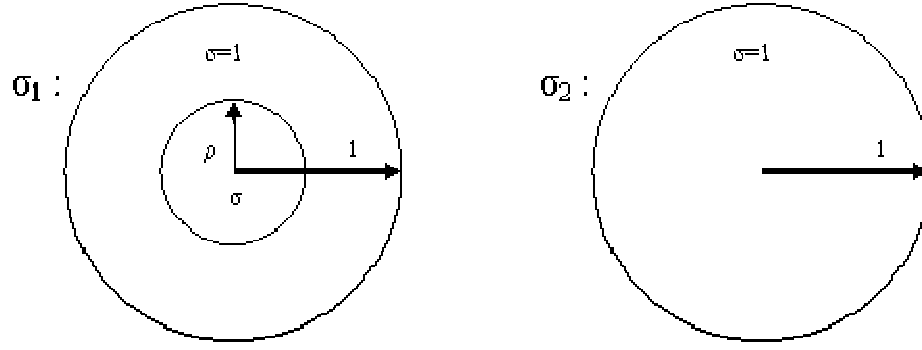
Figure 2.1 Conductivity distributions σ_1 and σ_2.

For further simplification, radii of the disks are taken to be 1 unit and background conductivities are also equated to 1.

It is known that magnetic flux density based distinguishability measure is defined in Equation (2.3), in a general sense. In 2-D MREIT problems, magnetic flux density is measured in z-direction which is orthogonal to the 2-D problem space (x-y plane). The z-component of $\vec{B}$ is given as:

$$B_z(x,y) = \frac{\mu_0}{4\pi} \int \frac{J_x(x',y')(y-y') - J_y(x',y')(x-x')}{R^3} ds' \qquad (2.5)$$

where J_x and J_y are x and y components of the current density, respectively, μ_0 is the permeability of free space, and R is the distance between the source (x',y') and the field (x,y) points. Another point to take into account is whether the current density distribution creates a unique magnetic flux density distribution or not, at a single point, the magnetic flux density can be created due to different current densities. However, when magnetic flux density distribution is concerned then a unique relation between magnetic flux density and current density exists. This topic is considered separately in appendix A.

In order to define a distinguishability measure in cylindrical coordinates, magnetic flux density needs to be transformed into cylindrical coordinates:

$$J_x(x',y') = J_r(r',\theta')\cos\theta' - J_\theta(r',\theta')\sin\theta'$$

$$J_y(x', y') = J_r(r', \theta')\sin\theta' + J_\theta(r', \theta')\cos\theta'$$

$$x = r\cos\theta \text{ and } y = r\sin\theta$$

$$x' = r'\cos\theta' \text{ and } y' = r'\sin\theta'$$

then

$$B_z(r, \theta) = \frac{\mu_0}{4\pi}\int \frac{\left[J_r(r', \theta')\cos\theta' - J_\theta(r', \theta')\sin\theta'\right](r\sin\theta - r'\sin\theta')}{R^3}ds'$$

$$- \frac{\mu_0}{4\pi}\int \frac{\left[J_r(r', \theta')\sin\theta' + J_\theta(r', \theta')\cos\theta'\right](r\cos\theta - r'\cos\theta')}{R^3}ds' \quad . (2.6)$$

Reorganizing the terms in Equation (2.6), following equation is obtained:

$$B_z(r, \theta) = \frac{\mu_0}{4\pi}\int \frac{J_r(r', \theta')r\sin(\theta - \theta') + J_\theta(r', \theta')(r' - r\cos(\theta - \theta'))}{R^3}ds' \quad . \tag{2.7}$$

When the source and observation points are the same, Equation (2.7) has a singularity. When there is no singularity, the surface integral is evaluated easily. When source and observation points overlap and at the same time uniform current flow is assumed through each infinitesimal circular element, then magnetic flux density at the center of a circular element is zero as shown in appendix B. Therefore the effect of each element on itself can be taken as zero, resolving the singularity problem.

The effect of conductivity distribution on current density and magnetic flux density should be taken into account. For σ_1 distribution:

$$B_z(r, \theta, \sigma_1) = \frac{\mu_0}{4\pi}\int \frac{J_r(r', \theta', \sigma_1)r\sin(\theta - \theta') + J_\theta(r', \theta', \sigma_1)(r' - r\cos(\theta - \theta'))}{R^3}ds'$$

$$(2.8.a)$$

and for σ_2:

$$B_z(r, \theta, \sigma_2) = \frac{\mu_0}{4\pi}\int \frac{J_r(r', \theta', \sigma_2)r\sin(\theta - \theta') + J_\theta(r', \theta', \sigma_2)(r' - r\cos(\theta - \theta'))}{R^3}ds' \quad .$$

$$(2.8.b)$$

For the 2-D problem given here, the total norm of the differences between magnetic flux density measurements over the entire region is used as a measure of distinguishability as

$$\left\|B_z(\sigma_1) - B_z(\sigma_2)\right\| \tag{2.9}$$

where, $\| \cdot \|$ denotes the L_2 norm. The difference of $B_z(\sigma_1)$ and $B_z(\sigma_2)$ can be expressed more explicitly as,

$$B_z(r,\theta,\sigma_1) - B_z(r,\theta,\sigma_2) =$$
$$\frac{\mu_0}{4\pi}\int\frac{J_r(r',\theta',\sigma_1)r\sin(\theta-\theta') + J_\theta(r',\theta',\sigma_1)(r'-r\cos(\theta-\theta'))}{R^3}ds'$$
$$-\frac{\mu_0}{4\pi}\int\frac{J_r(r',\theta',\sigma_2)r\sin(\theta-\theta') + J_\theta(r',\theta',\sigma_2)(r'-r\cos(\theta-\theta'))}{R^3}ds' . \quad (2.10)$$

Calculating the norms of both sides, the following expression can be obtained:

$$\| B_z(r,\theta,\sigma_1) - B_z(r,\theta,\sigma_2) \| \le \frac{\mu_0}{4\pi}\int\frac{\| J_r(r',\theta,\sigma_1) - J_r(r',\theta,\sigma_2) \| \| r\sin(\theta-\theta') \|}{R^3}ds'$$
$$+\frac{\mu_0}{4\pi}\int\frac{\| J_\theta(r',\theta',\sigma_1) - J_\theta(r',\theta',\sigma_2) \| \| r'-r\cos(\theta-\theta') \|}{R^3}ds' . \quad (2.11)$$

If injected current is assumed as

$$j(\theta) = \sum_{n=1}^{\infty} \left(C_n \cos n\theta + S_n \sin n\theta \right)$$

then, potential distributions can be readily found [2]. For σ_2 conductivity distribution, potential at any point is found as

$$V(r,\theta,\sigma_2) = -\sum_{n=1}^{\infty}\frac{r^n}{n}\left(C_n \cos n\theta + S_n \sin n\theta \right). \quad (2.12)$$

It is known that

$$\vec{J} = -\sigma \nabla V \quad (2.13)$$

and

$$\nabla = \vec{a}_r \frac{\partial}{\partial r} + \vec{a}_\theta \frac{1}{r}\frac{\partial}{\partial \theta} . \quad (2.14)$$

Therefore, the current density can be evaluated as follows

$$J_r(r,\theta,\sigma_2) = -\frac{\partial V(r,\theta,\sigma_2)}{\partial r} = \sum_{n=1}^{\infty}r^{n-1}\left(C_n \cos n\theta + S_n \sin n\theta \right) \quad (2.15.a)$$

$$J_\theta(r,\theta,\sigma_2) = -\frac{1}{r}\frac{\partial V(r,\theta,\sigma_2)}{\partial \theta} = \sum_{n=1}^{\infty}r^{n-1}\left(-C_n \sin n\theta + S_n \cos n\theta \right). \quad (2.15.b)$$

On the other hand, potential for σ_1 can be written as

$$V(r,\theta,\sigma_1) = -\sum_{n=1}^{\infty} \frac{r^n}{n} \cdot \frac{1-\mu\rho^{2n}}{1+\mu\rho^{2n}}\left(C_n \cos n\theta + S_n \sin n\theta\right) \tag{2.16}$$

where

$$\mu = \frac{\sigma-1}{\sigma+1}.$$

Then the cylindrical components of current density become:

$$J_r(r,\theta,\sigma_1) = -\frac{\partial V(r,\theta,\sigma_1)}{\partial r} = \sum_{n=1}^{\infty} r^{n-1} \cdot \frac{1-\mu\rho^{2n}}{1+\mu\rho^{2n}}\left(C_n \cos n\theta + S_n \sin n\theta\right) \tag{2.17.a}$$

$$J_\theta(r,\theta,\sigma_1) = -\frac{1}{r}\frac{\partial V(r,\theta,\sigma_1)}{\partial \theta} = \sum_{n=1}^{\infty} r^{n-1} \cdot \frac{1-\mu\rho^{2n}}{1+\mu\rho^{2n}}\left(-C_n \sin n\theta + S_n \cos n\theta\right). \tag{2.17.b}$$

Now, the difference between current densities can be analyzed. This difference has two components in the directions of r and θ, therefore it is written as

$$J_r(r,\theta,\sigma_2) - J_r(r,\theta,\sigma_1) = \sum_{n=1}^{\infty} r^{n-1}\frac{2\mu\rho^{2n}}{1+\mu\rho^{2n}}\left(C_n \cos n\theta + S_n \sin n\theta\right) \tag{2.18.a}$$

$$J_\theta(r,\theta,\sigma_2) - J_\theta(r,\theta,\sigma_1) = \sum_{n=1}^{\infty} r^{n-1}\frac{2\mu\rho^{2n}}{1+\mu\rho^{2n}}\left(-C_n \sin n\theta + S_n \cos n\theta\right). \tag{2.18.b}$$

Substituting the norms of these difference terms, $\left\|J_r(r',\theta',\sigma_1) - J_r(r',\theta',\sigma_2)\right\|$ and $\left\|J_\theta(r',\theta',\sigma_1) - J_\theta(r',\theta',\sigma_2)\right\|$, in Equation (2.11)

$$\left\|B_z(\sigma_1) - B_z(\sigma_2)\right\| \le \frac{\mu_0}{4\pi}\frac{2|\mu|\rho^2}{1+\mu\rho^2}\iint \frac{\left\|r\sin(\theta-\theta')\right\| + \left\|r'-r\cos(\theta-\theta')\right\|}{(r^2+r'^2-2rr'\cos(\theta-\theta'))^{\frac{3}{2}}}ds'ds = D(\sigma,\rho) \tag{2.19}$$

is obtained. Conductivity distributions σ_1 with

$$D(\sigma,\rho) \le \varepsilon \tag{2.20.a}$$

are not distinguishable from uniform conductivity distribution σ_2. On the other hand, note that not all σ_1 distributions reach the distinguishability limit given in Equation (2.19) when

$$D(\sigma,\rho) > \varepsilon. \tag{2.20.b}$$

This could be true only when the equality

$$\|B_z(\sigma_1) - B_z(\sigma_2)\| = D(\sigma, \rho) \tag{2.21}$$

holds. Determining a current injection pattern, which satisfies the equality in Equation (2.21), is not straight forward. Therefore, it is assumed that a current injection pattern that satisfies the equality in Equation (2.21) exists. In this case, when Equation (2.20.b) is satisfied, σ_1 is distinguishable from σ_2. Current injection pattern(s) satisfying Equation (2.21) provides the broadest distinguishability range in terms of σ, ρ and ε. The term in the integration in Equation (2.19) is independent of σ and ρ, hence it acts as a constant for a given inhomogeneity at the center. Numerical results demonstrating the behavior of $D(\sigma, \rho)$ are presented in the following part.

2.4.   Comparison of Surface Potential Based Distinguishability and Magnetic Flux Density Based Distinguishability

In order to investigate the relative performances of magnetic flux density and surface potential based impedance imaging, distinguishability measures of both techniques are compared. In Figure 2.2, the distinguishability measure, $D(\sigma, \rho)$ is plotted as a function conductivity (σ) and radius (ρ) of the inhomogeneity when the measurement precision $\varepsilon = 0.1$. In Figure 2.2, vertically traced region is the indistinguishable region for surface potential measurement based (EIT) case. Indistinguishable region for MREIT is indicated with horizontal shading. MREIT measurements provide a remarkable improvement in distinguishability. Distinguishability function $D(\sigma, \rho)$ of MREIT measurements is presented in Figure 2.3. At different precision levels, the performances of the techniques are similar to the one in Figure 2.2.
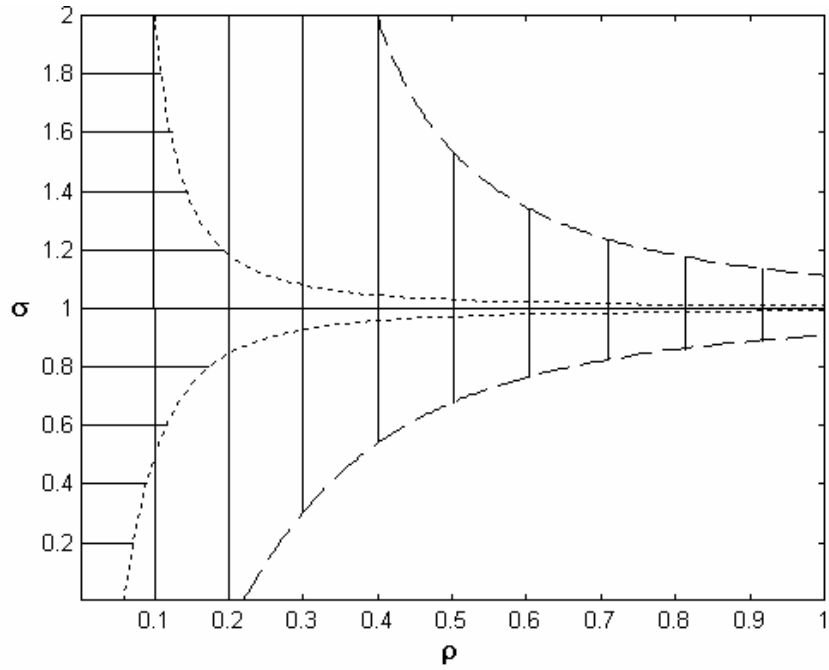
Figure 2.2 Indistinguishable inhomogeneities as a function of conductivity and radius of a concentric inhomogeneity for MREIT and EIT based measurements at the precision level equal to 0.1 are shown with horizontal and vertical shading, respectively.
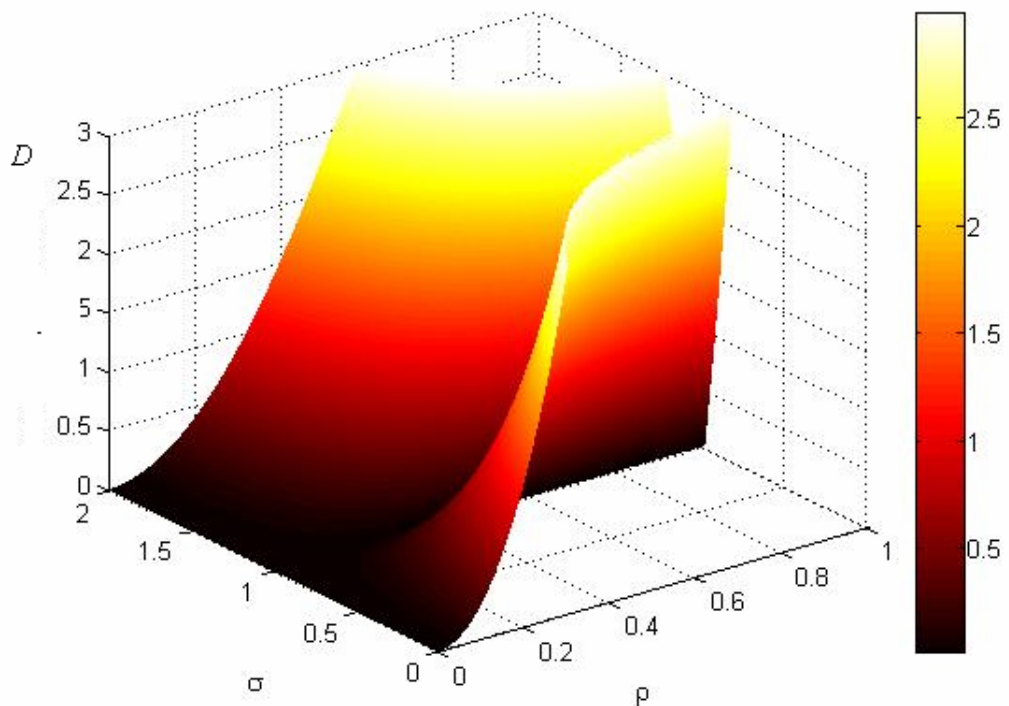
Figure 2.3 Distinguishability function for magnetic flux density based (i.e. MREIT) measurements, $D(\sigma, \rho)$, as a function of conductivity and radius of a concentric inhomogeneity.

2.5. Distinguishability Measure for a 2-D Cylindrical Body with Eccentric Inhomogeneity

Distinguishability problem of eccentric cylindrical inhomogeneity in a cylindrical body can be transformed into a 2-D problem when cylinders are assumed to have uniform cross section, to be infinitely long and have no variation in longitudinal direction. In this case, 2-D shapes of Figure 2.4 are the slices of 3-D geometries.
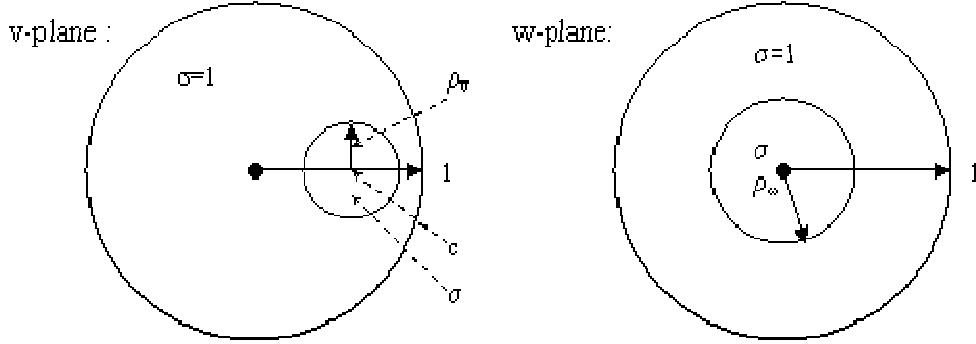
Figure 2.4 2-D views of eccentric and concentric planes. *V-plane* is the original problem plane and *w*-plane is the transform plane after conformal mapping.

In order to simplify the solution of the eccentric problem, radii of the disks and background conductivity values are taken as unity. To overcome the difficulty of solving the eccentric problem analytically, the eccentric problem in *v*-plane can be transformed to the concentric problem in *w*-plane by conformal mapping as given in Seager *et al* [26].

The relation between *v*-plane and *w*-plane are as follows:

$$w = \frac{d - v}{dv - 1} \tag{2.22}$$

with

$$d = \frac{1 + c^2 - \rho_v^2 - \left[\left(1 + c^2 - \rho_v^2\right)^2 - 4c^2\right]^{\frac{1}{2}}}{2c}$$

and therefore,

$$r_w e^{j\theta_w} = \frac{d - r_v e^{j\theta_v}}{d r_v e^{j\theta_v} - 1}. \tag{2.23}$$

(r_w, θ_w) can be represented in terms of (r_v, θ_v) as:

$$r_w = \left[\frac{(d - r_v \cos\theta_v)^2 + (r_v \sin\theta_v)^2}{(d r_v \cos\theta_v - 1)^2 + (d r_v \sin\theta_v)^2} \right]^{\frac{1}{2}} \tag{2.24.a}$$

$$\theta_w = \arctan(\frac{-r_v \sin\theta_v}{d - r_v \cos\theta_v}) - \arctan(\frac{d r_v \sin\theta_v}{d r_v \cos\theta_v - 1}). \tag{2.24.b}$$

Magnetic flux density at any point in the v-plane can be expressed as

$$B_{v,z}(r,\theta,\sigma_1) = \frac{\mu_0}{4\pi} \int \frac{J_{v,r}(r',\theta',\sigma_1) r \sin(\theta - \theta') + J_{v,\theta}(r',\theta',\sigma_1)(r' - r\cos(\theta - \theta'))}{R^3} ds'$$
$$\tag{2.25.a}$$

$$B_{v,z}(r,\theta,\sigma_2) = \frac{\mu_0}{4\pi} \int \frac{J_{v,r}(r',\theta',\sigma_2) r \sin(\theta - \theta') + J_{v,\theta}(r',\theta',\sigma_2)(r' - r\cos(\theta - \theta'))}{R^3} ds'$$
$$\tag{2.25.b}$$

where

σ_1: Conductivity distribution when eccentric inhomogeneity is present, and

σ_2: Conductivity distribution when eccentric inhomogeneity is absent, which means only background object is present.

In Equation (2.25) current distribution is unknown and it is not an easy task to solve the current density distribution in v-plane. On the other hand, current density distribution of w-plane is known from previous sections. Thus relation between current density distributions of v and w-planes should be found.

Governing equations for potential distribution in both planes are Laplacian with Neumann boundary conditions.
In v-plane:

$$\nabla \cdot \sigma_v \nabla V_v = 0 \tag{2.26.a}$$

$$\bar{J}_v = -\sigma_v \nabla V_v \tag{2.26.b}$$

In w-plane:

$$\nabla \cdot \sigma_w \nabla V_w = 0 \qquad\qquad (2.27.a)$$

$$\bar{J}_w = -\sigma_w \nabla V_w \qquad\qquad (2.27.b)$$

Therefore potential distribution is transformed with conformal mapping by only altering the positions. That means potential at a point is the same as potential at the mapped point:

$$V_v(r_v, \theta_v) = V_w(r_v(r_w, \theta_w), \theta_v(r_w, \theta_w)). \qquad\qquad (2.28)$$

It is also known that

$$\nabla = \hat{a}_r \frac{\partial}{\partial r} + \hat{a}_\theta \frac{1}{r} \frac{\partial}{\partial \theta} \qquad\qquad (2.29)$$

in cylindrical coordinates. Then r and θ components of J_v can be written as:

$$J_{v,r}(r, \theta, \sigma_1) = -\sigma_v(r, \theta) \frac{\partial V_v}{\partial r_v}\bigg|_{(r,\theta)} \qquad\qquad (2.30.a)$$

$$J_{v,\theta}(r, \theta, \sigma_1) = -\sigma_v(r, \theta) \frac{1}{r_v} \frac{\partial V_v}{\partial \theta_v}\bigg|_{(r,\theta)}. \qquad\qquad (2.30.b)$$

On the other hand, partial derivatives in v-plane can be expressed in terms of partial derivatives in w-plane as:

$$\frac{\partial V_v}{\partial r_v} = \frac{\partial V_w}{\partial r_w} \frac{\partial r_w}{\partial r_v} + \frac{\partial V_w}{\partial \theta_w} \frac{\partial \theta_w}{\partial r_v} \qquad\qquad (2.31.a)$$

$$\frac{\partial V_v}{\partial \theta_v} = \frac{\partial V_w}{\partial r_w} \frac{\partial r_w}{\partial \theta_v} + \frac{\partial V_w}{\partial \theta_w} \frac{\partial \theta_w}{\partial \theta_v}. \qquad\qquad (2.31.b)$$

It is known that,

$$\frac{\partial V_w}{\partial r_w} = \frac{-1}{\sigma_w(r_w, \theta_w)} J_{w,r}(r_w, \theta_w, \sigma) \qquad\qquad (2.32.a)$$

$$\frac{\partial V_w}{\partial \theta_w} = \frac{-r_w}{\sigma_w(r_w, \theta_w)} J_{w,\theta}(r_w, \theta_w, \sigma). \qquad\qquad (2.32.b)$$

When Equations (2.31) and (2.32) are substituted into Equation (2.30), relations between current densities in v and w-planes are found:

$$J_{v,r}(r_v, \theta_v, \sigma) = \frac{\sigma_v(r_v, \theta_v)}{\sigma_w(r_w, \theta_w)} \frac{\partial r_w}{\partial r_v} J_{w,r}(r_w, \theta_w, \sigma) + \frac{\sigma_v(r_v, \theta_v)}{\sigma_w(r_w, \theta_w)} \frac{r_w}{1} \frac{\partial \theta_w}{\partial r_v} J_{w,\theta}(r_w, \theta_w, \sigma)$$

$$(2.33.a)$$

$$J_{v,\theta}(r_v,\theta_v,\sigma) = \frac{\sigma_v(r_v,\theta_v)}{\sigma_w(r_w,\theta_w)}\frac{r_w}{r_v}\frac{\partial\theta_w}{\partial\theta_v}J_{w,\theta}(r_w,\theta_w,\sigma) + \frac{\sigma_v(r_v,\theta_v)}{\sigma_w(r_w,\theta_w)}\frac{1}{r_v}\frac{\partial r_w}{\partial\theta_v}J_{w,r}(r_w,\theta_w,\sigma).$$

(2.33.b)

Conductivity distribution is changed by the conformal mapping. However, magnitudes of conductivities are not altered, only their positions are changed, so we can write

$$\sigma_v(r_v,\theta_v) = \sigma_w(r_w,\theta_w).$$ (2.34)

Therefore equation pairs in Equation (2.33) can be rewritten as

$$J_{v,r}(r_v,\theta_v,\sigma) = \frac{\partial r_w}{\partial r_v}J_{w,r}(r_w,\theta_w,\sigma) + r_w\frac{\partial\theta_w}{\partial r_v}J_{w,\theta}(r_w,\theta_w,\sigma)$$ (2.35.a)

$$J_{v,\theta}(r_v,\theta_v,\sigma) = \frac{1}{r_v}\frac{\partial r_w}{\partial\theta_v}J_{w,r}(r_w,\theta_w,\sigma) + \frac{r_w}{r_v}\frac{\partial\theta_w}{\partial\theta_v}J_{w,\theta}(r_w,\theta_w,\sigma).$$ (2.35.b)

Now, the difference between magnetic flux densities at any point inside the object due to different conductivity distributions in v-plane is expressed as

$$B_{v,z}(r,\theta,\sigma_1) - B_{v,z}(r,\theta,\sigma_2) = \frac{\mu_0}{4\pi}\int\frac{[J_{v,r}(\sigma_1)-J_{v,r}(\sigma_2)]r_v'\sin(\theta_v-\theta_v')+[J_{v,\theta}(\sigma_1)-J_{v,\theta}(\sigma_2)](r_v'-r_v\cos(\theta_v-\theta_v'))}{R^3}ds'$$

(2.36)

From Equation (2.35) difference between current densities is obtained as follows:

$$J_{v,r}(r_v',\theta_v',\sigma_1) - J_{v,r}(r_v',\theta_v',\sigma_2) =$$
$$[J_{w,r}(r_w',\theta_w',\sigma_1)-J_{w,r}(r_w',\theta_w',\sigma_2)]\frac{\partial r_w}{\partial r_v} + r_w[J_{w,\theta}(r_w',\theta_w',\sigma_1)-J_{w,\theta}(r_w',\theta_w',\sigma_2)]\frac{\partial\theta_w}{\partial r_v}$$ (2.37.a)

$$J_{v,\theta}(r_v',\theta_v',\sigma_1) - J_{v,\theta}(r_v',\theta_v',\sigma_2) =$$
$$\frac{1}{r_v}[J_{w,r}(r_w',\theta_w',\sigma_1)-J_{w,r}(r_w',\theta_w',\sigma_2)]\frac{\partial r_w}{\partial\theta_v} + \frac{r_w}{r_v}[J_{w,\theta}(r_w',\theta_w',\sigma_1)-J_{w,\theta}(r_w',\theta_w',\sigma_2)]\frac{\partial\theta_w}{\partial\theta_v}$$ (2.37.b)

To find the measure for distinguishability, difference between magnetic flux densities at all points should be integrated. For this purpose, current density differences in Equation (2.37) are substituted into Equation (2.36) and L_2 norm of resulting expression is taken. By applying triangular inequality to the norm, the following expression is obtained:

$$\left\| B_{v,z}(\sigma_1) - B_{v,z}(\sigma_2) \right\| \leq \frac{\mu_0}{4\pi} \frac{2|\mu|\rho_v^2}{1+\mu\rho_v^2} \iint \frac{\left\| r_v \sin(\theta_v - \theta_v') \right\| \left[\left\| \frac{\partial r_w}{\partial r_v} \right\| + \left\| r_w \frac{\partial \theta_w}{\partial r_v} \right\| \right]}{R^3} ds' ds$$

$$+ \frac{\mu_0}{4\pi} \frac{2|\mu|\rho_v^2}{1+\mu\rho_v^2} \iint \frac{\left\| r_v' - r_v \cos(\theta_v - \theta_v') \right\| \left[\left\| \frac{1}{r_v} \frac{\partial r_w}{\partial \theta_v} \right\| + \left\| \frac{r_w}{r_v} \frac{\partial \theta_w}{\partial \theta_v} \right\| \right]}{R^3} ds' ds = D_v(\sigma, \rho) \quad (2.38)$$

where

μ_0 is the permeability of free space and

$$\mu = \frac{\sigma - 1}{\sigma + 1}.$$

Conductivity distributions σ_1 with

$$D_v(\sigma, \rho) \leq \varepsilon \qquad\qquad (2.39.a)$$

are not distinguishable from uniform conductivity distributions, σ_2. Here, ε represents the precision of magnetic flux density measurements in MREIT. If on the other hand,

$$D_v(\sigma, \rho) > \varepsilon \qquad\qquad (2.39.b)$$

then σ_1 is distinguishable from σ_2. However, every current injection pattern can not reach the distinguishability limit given in Equation (2.38). It is assumed that there exists a current injection pattern that satisfies

$$\left\| B_{v,z}(\sigma_1) - B_{v,z}(\sigma_2) \right\| = D_v(\sigma, \rho). \qquad\qquad (2.40)$$

In this case, if inequality in Equation (2.39.b) is satisfied, inhomogeneity is differentiated from the background. Other current injection patterns could also distinguish the inhomogeneity when

$$\left\| B_{v,z}(\sigma_1) - B_{v,z}(\sigma_2) \right\| > \varepsilon. \qquad\qquad (2.41)$$

Based on Equation (2.38), distinguishability limit of concentric and eccentric cases are drawn on the same plot in Figure 2.5. In eccentric case with $c = 0.5$ (c is the amount of shift from the centre), ρ is limited to [0, 0.5] region. When it is greater than 0.5, distinguishability is not defined since the inhomogeneity touches the surface. In Figure 2.5, distinguishability limits are identical for concentric and eccentric cases apart from small deviations for the eccentric inhomogeneity case.

These ripple like deviations are thought to occur due to numerical errors. Therefore, it is concluded that the same distinguishability limit is obtained independent of the inhomogeneity location. This is due to the uniform sensitivity of magnetic flux density measurements in MREIT over the entire field of view (FOV). However in EIT, sensitivity of surface potential measurements to conductivity perturbations is position dependent, being lowest at the centre of the FOV.
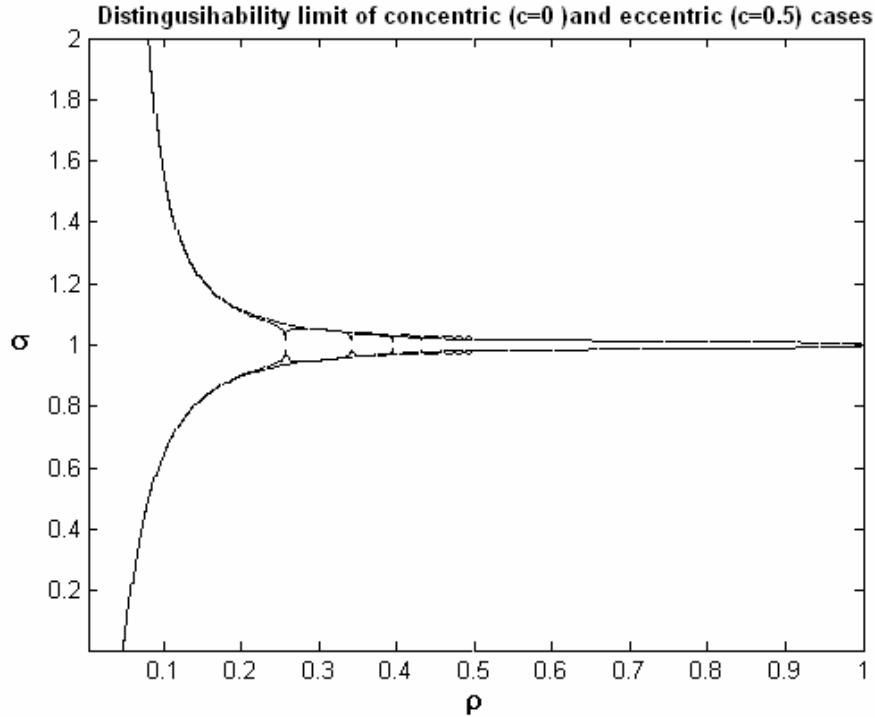
Figure 2.5 Distinguishability limit of concentric (*c*=0) and eccentric (*c*=0.5) cases when $\varepsilon = 0.1$ where ε is the measurement precision.

2.6. Discussion

In this Chapter, a definition of distinguishability measure for MREIT is presented. This definition is valid for 2D and 3D structures of any shape. As a specific case, 2D cylindrical body with concentric inhomogeneity is investigated. With the help of simplifying assumptions of unity background conductivity and radius, a bound of distinguishability is derived and presented for a given measurement precision. Then, the simulation results are compared with the distinguishability of potential based

(EIT) measurements. It is found that for a given measurement precision, magnetic flux density based measurements provide a greater distinguishable region when compared to the potential based one. In other words, MREIT is superior in detecting inner region inhomogeneities compared to EIT. When conductivity of inhomogeneity is equal to 0.8, EIT can detect inhomogeneities with the radius of 0.7, whereas MREIT can detect radius of 0.18, which points increment of %74 in detection capacity. This result is expected since magnetic flux density is measured throughout the imaged region in MREIT in contrast to the potential measurements which are carried out only at the body surface in EIT. Surface potential measurements are almost insensitive to inner conductivity perturbations. Note that measurement precisions of MREIT and EIT could be different, and they are not included in this analysis.

Determining optimum current injection pattern for the simple 2D problem is considered in the next chapter.

CHAPTER 3

OPTIMUM CURRENT INJECTION PATTERN

3.1. Introduction

Determining optimum current injection pattern is of interest in identifying smaller inhomogeneities in Magnetic Resonance Electrical Impedance Tomography (MREIT) as in Electrical Impedance Tomography (EIT). It is possible to determine the best current pattern in EIT by maximising the distinguishability. Distinguishability for MREIT is discussed in detail in Chapter 2. Here a brief overview is provided.

Distinguishability in EIT is based on the fact that the presence of a conductivity perturbation changes the current density distribution hence the potential field inside a volume conductor due to an externally applied current [2]. If this change causes detectable changes in measured potentials at the surface, then the conductivity perturbation is said to be distinguishable. Gisser *et al* introduced an adaptive current EIT system in order to realise the best current injection strategy to maximize the distinguishability in EIT [5]. Gisser *et al* limits the maximum current which can be applied to each electrode [5]. Current patterns maximizing the distinguishability in EIT is also further discussed under other constraints such as constant applied power, constant total current to the subject [11], [12], [59], and [60].

In MREIT, conductivity images are reconstructed from the measurements of magnetic flux density generated by the injected current. Conductivity distribution is obtained from magnetic flux density directly, or the current density distribution is calculated from the measured magnetic flux density first, and then the conductivity is reconstructed. Based on these two approaches, several image reconstruction

algorithms have been proposed for MREIT in recent years [6], [7], [8], [10], [30], [33], [38], [47], [48], [61], [62], and [63]. In order to further extend the limits of MREIT technique, researchers work on noise and resolution limits [51]. At this point, a distinguishability measure for MREIT based on magnetic flux density measurements is defined by Altunel *et al* as in Chapter 2 [64]. Distinguishability can be improved by increasing the system signal to noise ratio (SNR) of the magnetic resonance (MR) system using high field systems [51]. On the other hand, for a given main magnetic field strength, distinguishability should be maximized by using optimum current injection pattern. Another way of increasing the SNR of the current density measurements is to increase the magnetic flux density induced by the probing current by optimising the pulse sequence design [56] which is not in the scope of this Chapter and discussion about this topic is left to the Chapter 6.

In this Chapter, optimum MREIT current injection pattern is determined to maximize the distinguishability of concentric and eccentric inhomogeneities inside a 2-D cylindrical body in Section 3.2 and Section 3.3 respectively.

3.2. Determination of Optimum Current Injection Strategy for a Concentric Inhomogeneity

Infinitely long cylinders with uniform conductivity along the longitudinal direction can be simplified to a 2-D problem as in Figure 2.1. Considering conductivity distributions σ_1 and σ_2 given as:

$$\sigma_1 = \begin{cases} 1, & \text{for } \rho < r < 1 \\ \sigma, & \text{for } 0 < r < \rho \end{cases} \tag{3.1.a}$$

and

$$\sigma_2 = 1, \text{ for } 0 < r < 1. \tag{3.1.b}$$

The difference between the magnetic flux densities at any point between the cases where the inhomogeneity is present and not present as:

$$B_z(r,\theta,\sigma_1) - B_z(r,\theta,\sigma_2) =$$

$$\frac{\mu_0}{4\pi} \int \frac{J_r(r',\theta',\sigma_1)r\sin(\theta-\theta') + J_\varsigma(r',\theta',\sigma_1)(r'-r\cos(\theta-\theta'))}{R^3} ds'$$

$$-\frac{\mu_0}{4\pi} \int \frac{J_r(r',\theta',\sigma_2)r\sin(\theta-\theta') + J_\varsigma(r',\theta',\sigma_2)(r'-r\cos(\theta-\theta'))}{R^3} ds'. \qquad (3.2)$$

Cylindrical coordinates are preferred due to the shape of the object and of the inhomogeneity. To formulate the optimisation problem maximising the distinguishability as defined by Altunel *et al* [64], the object is divided into K sub-regions. When this is done, the aforementioned difference of magnetic flux densities at the ith sub-region is obtained as follows:

$$\Delta B_{z_i} = B_z(p_i,\sigma_2) - B_z(p_i,\sigma_1) = \frac{\pi_0}{4\pi} \sum_{\substack{k=1 \\ k\neq i}}^{K} \left[\Delta J_{r_k} f(p_i,p_k) + \Delta J_{\theta_k} g(p_i,p_k) \right] \Delta S_k \quad (3.3)$$

where

p_i : observation point , (r,θ) .

p_k : source point , (r',θ') .

Total magnetic flux difference is the sum of individual differences at all points,

$$\Delta B_z = \sum_{l=1}^{K} \left| \Delta B_{z_l} \right| \qquad (3.4)$$

or

$$\Delta B_z = \sum_{l=1}^{K} \left| \frac{\mu_0}{4\pi} \sum_{\substack{k=1 \\ k\neq l}}^{K} \left(\Delta J_{r_k} f(p_l,p_k) + \Delta J_{\theta_k} g(p_l,p_k) \right) \Delta S_k \right|. \qquad (3.5)$$

Some symbols in Equation (3.5) are given as:

$$\Delta J_{r_k} = \sum_{n=1}^{\infty} r_k^{n-1} \frac{2\mu\rho^{2n}}{1+\mu\rho^{2n}} \left(C_n \cos(n\theta_k) + S_n \sin(n\theta_k) \right)$$

$$\Delta J_{\theta_k} = \sum_{n=1}^{\infty} r_k^{n-1} \frac{2\mu\rho^{2n}}{1+\mu\rho^{2n}} \left(-C_n \sin(n\theta_k) + S_n \cos(n\theta_k) \right)$$

$$f(p_l,p_k) = r_l \sin(\theta_l - \theta_k)$$

$$g(p_l,p_k) = r_k - r_l \cos(\theta_l - \theta_k).$$

Hence, optimisation problem may be stated as:

$$\text{maximise } \Delta B_z$$

$$\text{s.t. } \frac{1}{2} \int_0^{2\pi} |j(\theta)| d\theta = 1 \text{ (total injected current is kept unity.)}$$

$$\text{where } j(\theta) = \sum_{n=1}^{N} C_n \cos n\theta + S_n \sin n\theta . \tag{3.6}$$

In this problem, coefficients of $j(\theta)$, namely C_n and S_n will be optimized. To solve the optimisation problem given in Equation (3.6), K is chosen as 96 and sub-regions are as shown in Figure 3.1.

Optimisation problem given in Equation (3.6) is solved numerically to determine the best current injection strategy. The optimisation algorithm uses the exterior penalty method with a gradient search algorithm for optimisation at each penalty level. Several N values are assigned to observe its effect on the resulting current injection pattern. In Figure 3.2, some of the resulting current patterns are presented. In all cases, current peaks converge to opposite sides (there are 180 degrees between the peaks) when total injected current is kept constant. Increasing N, the solution approaches to 180 degrees separated point electrodes for current injection. This implies that the best MREIT current injection pattern to image a 2-D concentric inhomogeneity is the opposite drive when the total injected current is kept constant. However, practically impulsive current density could be harmful to the living organism. Therefore, it should be approximated as far as the current injection pattern stays within the safety limits.
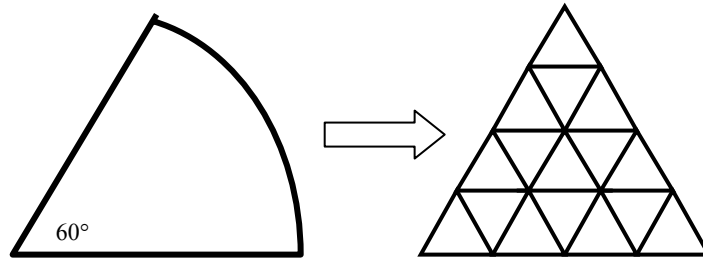
Figure 3.1 60° slice of circular object is discretised into 16 equivalent small triangles. Whole circular object is discretised as an equilateral hexagon. The hexagon is composed of 6 above equilateral triangles, and therefore of 96 small triangles.
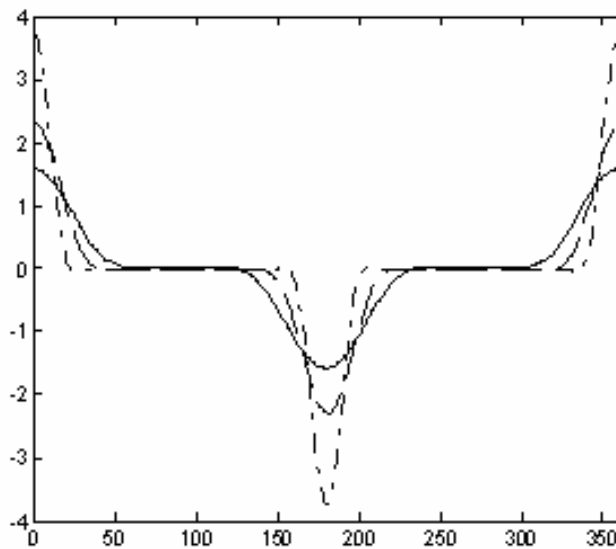
Figure 3.2 Current injection patterns when $K = 96$. Several N values are applied as 5 (solid), 10 (dashed) and 15 (dash-dot). Vertical axis is the magnitude of the current pattern. Horizontal axis is the degree of current injection angle.

3.3. Determination of Optimum Current Injection Pattern for an Eccentric Inhomogeneity

Determination of optimum current injection pattern for the case with an eccentric inhomogeneity is similar to the concentric case apart from conformal transformation step. Equation (3.3) is rewritten as

$$\Delta B_{v,z,i} = B_{v,z}(p_i, \sigma_2) - B_{v,z}(p_i, \sigma_1) = \frac{\pi_0}{4\pi} \sum_{\substack{k=1 \\ k \neq i}}^{K} \left[\Delta J_{v,r,k} f(p_i, p_k) + \Delta J_{v,\theta,k} g(p_i, p_k) \right] \Delta S_k$$

(3.7)

where

p_i: observation point, (r, θ)

p_k: source point, (r', θ').

Total flux density difference is the sum of individual differences at all points

$$\Delta B_{v,z} = \sum_{l=1}^{K} \left| \Delta B_{v,z,l} \right|.$$

(3.8)

Equations (3.7) and (3.8) are similar to (3.3) and (3.4), correspondingly. The major difference between concentric and eccentric optimisation problems is the definition of current density distributions. In eccentric case Equation (2.33) is taken into account. The rest of the optimisation problems are the same and for the eccentric case, problem definition given in Equation (3.6) is applied for the *v*-plane.

Results of the optimisation are presented in Figure 3.3, Figure 3.4, Figure 3.5 and Figure 3.6. In Figure 3.3, for a constant *c* and *K* values, two different *N* values are tried. It is observed that in both cases, injection pattern converges to opposite drive when the inhomogeneity lies on the drive axis. However, injected current closer to the inhomogeneity is larger in absolute amplitude and narrower than the current on the opposite side. As *N* increases, the optimum pattern converges to an impulsive drive. The effect of changing *c* on the current injection pattern can be seen in Figure 3.4. In this case, different *c* values give opposite drive pattern, but with varying widths. However, as the number of terms increases, they all converge to the same opposite drive. As a result, similar to the concentric case, in eccentric case opposite drive is found to be the optimum current injection pattern when total injected current is limited.
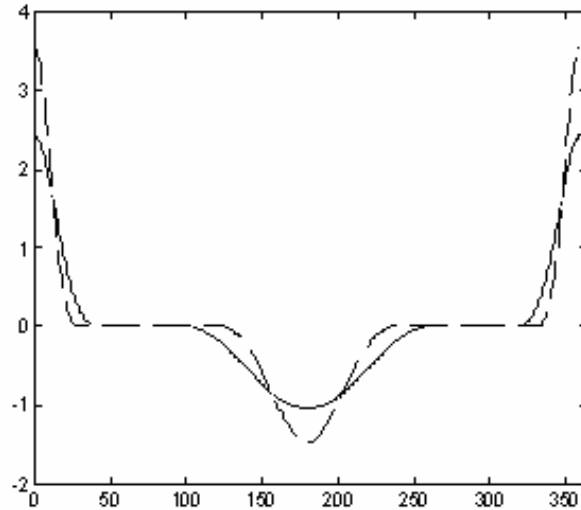
Figure 3.3 Current injection pattern when $K = 96$, ρ_v (radii of inhomogeneity)=0.2 and c (distance from the centre)=0.2. N takes two different values 5 (solid) and 10 (dashed) accordingly. Vertical axis is the magnitude of the current pattern. Horizontal axis is the degree of current injection angle.
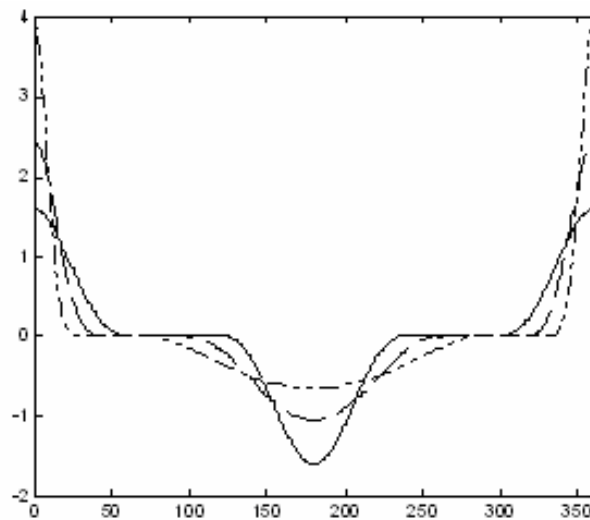
Figure 3.4 Current injection pattern when $K = 96$, $N = 5$. ρ_v (radii of inhomogeneity) is taken as 0.2. Here, c (distance from the centre) takes 3 different values as 0 (solid), 0.2 (dashed), 0.4 (dotted). Vertical axis is the magnitude of the current pattern. Horizontal axis is the degree of current injection angle.

From Figure 3.3 and Figure 3.4, it is observed that current injection pattern converges to opposite drive with the drive axis passing through the centre of the inhomogeneity. However, injected current closer to the inhomogeneity is larger in absolute amplitude and narrower than the current on the opposite side. This pattern should be expected, since the current will try to *focus* on the object, as much as the number of terms in the series allow.

An interesting case occurs when the axis in which inhomogeneity lies is forbidden for current injection axis: The resulting optimum current injection patterns are shown in Figure 3.5 and Figure 3.6. As can be seen from these figures, the current drive pattern is similar to the adjacent drive for this case. Two current peaks are at both sides of the horizontal axis which passes through the centre of the inhomogeneity. The location of the centre of these peaks is determined by the value of c, and the radius of the inhomogeneity. Because of its similarity to adjacent drive, this pattern will be called adjacent-like in this thesis. Further, these two peaks have the same width and the same height for a given number of terms in the series. As the number of terms in the series increases, these two peaks converge to an impulsive current density, with the same weight. It must be noted that the distinguishability figure obtained for these two types of aforementioned patterns are the same.

When the impact of these pattern results on electrode geometry is considered, different electrode geometries may be obtained. Optimum electrode geometry corresponding to current injection patterns defined in Figure 3.3 and Figure 3.4 is shown in Figure 3.7. On the other hand, optimum electrode geometry is shown in Figure 3.8 for the case when the axis in which inhomogeneity lies is forbidden. The length and the width of the arrows in Figure 3.7 and Figure 3.8 represents to the peak amplitude and the distribution of current on the surface.
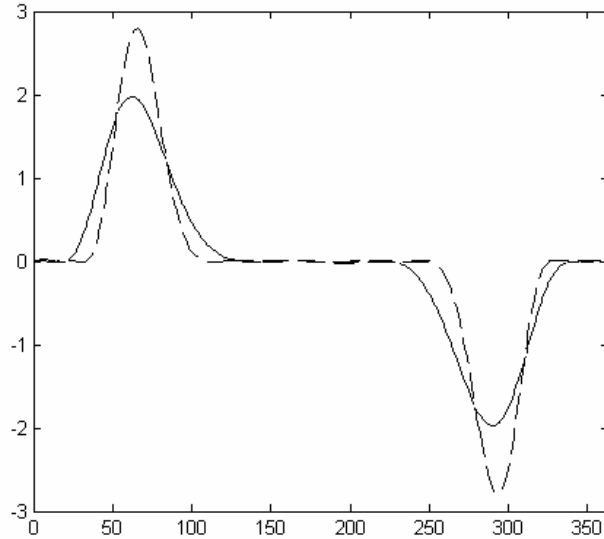
Figure 3.5 Current injection pattern when $K = 96$, $\rho_v = 0.2$ and $c = 0.2$. N takes two different values 5 (solid) and 10 (dashed) accordingly. In this case, the axis in which inhomogeneity is lying is forbidden for current injection pattern. That means another optimum current injection pattern is searched. Vertical axis is the magnitude of the current pattern. Horizontal axis is the degree of current injection angle.
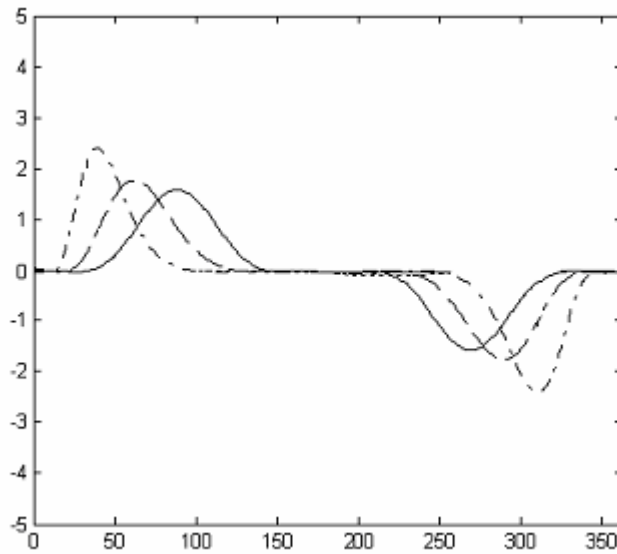
Figure 3.6 Current injection pattern when $K = 96$, $N = 5$ and $\rho_v = 0.2$. Here, c (distance from the centre) takes 3 different values as 0 (solid), 0.2 (dashed), 0.4 (dotted). In this case, the axis in which inhomogeneity is lying is forbidden for current injection pattern. That means another optimum current injection pattern is searched. Vertical axis is the magnitude of the current pattern. Horizontal axis is the degree of current injection angle.
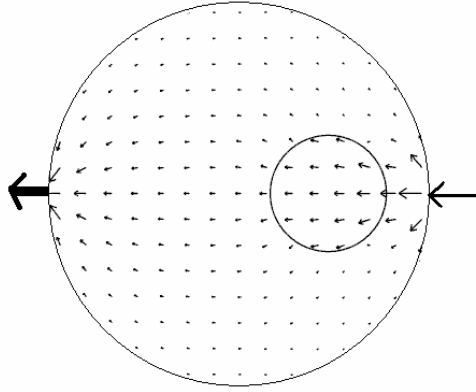
Figure 3.7 Optimum electrode geometry for 2-D cylindrical body with eccentric inhomogeneity.
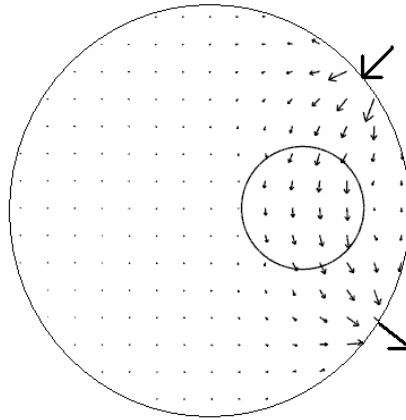
Figure 3.8 Optimum electrode geometry for 2-D cylindrical body with eccentric inhomogeneity, when the axis in which inhomogeneity is lying is forbidden for current injection pattern.

When K and N values increase, resulting pattern converges to two impulses located on opposite sides of the drive axis. To demonstrate this fact, the current injection pattern when $K = 2000$, $N = 1000$ is shown in Figure 3.9.
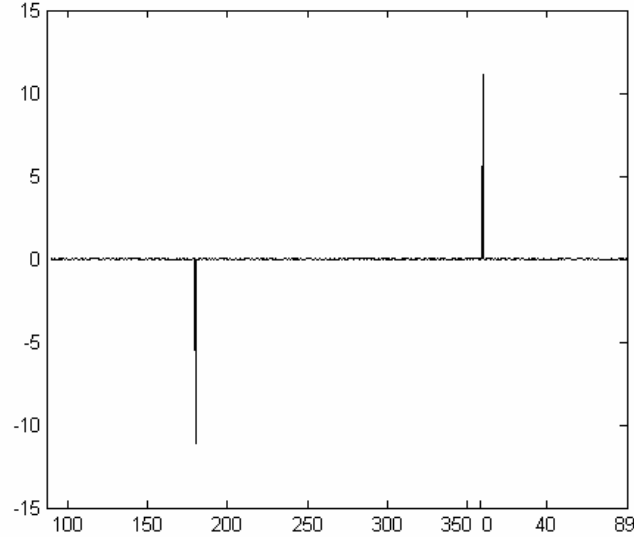
Figure 3.9 Current injection pattern when $K = 2000$, $N = 1000$. ρ_v (inhomogeneity radius) is taken as 0.5. On the other hand, c (distance from the centre) is equal to 0.5. Vertical axis is the magnitude of the current pattern. Horizontal axis is the degree of current injection angle.

Based on these results, possible optimum electrode geometry is the opposite drive with the drive axis passing through the centre of the inhomogeneity and current injection electrodes should be as small as possible. Another possibility is the adjacent-like drive that is mentioned before.

3.4.   **Discussion**

In this Chapter, the optimum current injection pattern to maximise distinguishability of concentric and eccentric conductivity inhomogeneities in MREIT are determined in a 2-D cylindrical body. When the total injected current is limited, the optimum solution converges to infinitesimally small opposite electrodes with impulsive currents. However, this kind of current application with high current density focused to a point electrode could be harmful to living organisms. Therefore, the best practical realisation of this finding should be injecting current between opposite electrodes with sizes such that patient safety limit is not exceeded. As an alterative, adjacent-like drive geometry may be utilized. This geometry may be especially useful if current density is required to be as small as possible. The reason

44

of this is that, this geometry gives the same distinguishability, although the current peak is smaller, for a given finite number of terms in the series, and in practice impulsive current density is neither possible nor desired.

The optimum current injection pattern for eccentric inhomogeneity is found to be opposite drive when the total injected current is limited. Current should be injected or sunk from a point on the side where the inhomogeneity is closest to the surface. Another possible pattern with the same distinguishability performance is obtained when the current drive axis is forced to be different from the inhomogeneity axis. These alternatives are important, and must be considered for the specific application and limitations. It is important to mention here that, although the measured parameter is the magnetic flux density in MREIT, the optimum current injection geometries for MREIT are found to be similar to the ones reported for EIT by Köksal and Eyüboğlu [59].

In MREIT studies, an important performance criterion is the spatial resolution. Improving spatial resolution limit means increased ability to resolve smaller structures. Couple of parameters such as the amplitude of the applied current and the system SNR affects the resolution limit. Amplitude of the applied current determines current density distribution inside the conductor to be imaged. Magnetic flux density distribution is related to the current density distribution via Biot-Savart relation. This means that increasing the applied current amplitude increases magnitudes of the current density and therefore magnitude of the magnetic flux density. In this Chapter, contribution to improvement in spatial resolution is made by optimising the current injection. When the system SNR and applied current are kept constant, the opposite and adjacent like current injection patterns determined above provides maximum distinguishability, which means higher spatial resolution limit.

Distinguishability definition is applied to a 3-D geometry and analytical solution will be obtained in the next chapter. Optimum current injection pattern for the 3-D geometry will also be provided there.

CHAPTER 4

DISTINGUISHABILITY AND OPTIMUM CURRENT INJECTION PATTERN FOR 3-D

4.1. Introduction

In this chapter, distinguishability definition is further extended to 3-D. A sphere with concentric inhomogeneity is adopted. An analytical expression for this geometry is obtained, in Section 4.1. Optimization of current injection pattern is formulated and solved in Section 4.2.

4.2. Distinguishability for Sphere

Potential distribution in a sphere is found after solving the Laplace equation. The Laplace equation in spherical coordinates is represented as

$$\frac{1}{r}\frac{\partial^2}{\partial^2 r}(rV) + \frac{1}{r^2 \sin\theta}\frac{\partial}{\partial\theta}(\sin\theta\frac{\partial V}{\partial\theta}) + \frac{1}{r^2 \sin^2\theta}\frac{\partial^2 V}{\partial\phi^2} = 0 \ . \tag{4.1}$$

4.2.1. Sphere with azimuthal symmetry

To simplify the problem, azimuthal symmetry condition is assumed to hold. When azimuthal symmetry condition holds, then potential distribution is in the following form [65]

$$V(r,\theta) = \sum_{l=0}^{\infty}\left[A_l r^l + B_l r^{-(l+1)}\right]P_l(\cos\theta) \tag{4.2}$$

where P_l is the Legendre polynomial of order l .

As the first step, consider a background sphere with centrally located spherical inhomogeneity as shown in Figure 4.1.
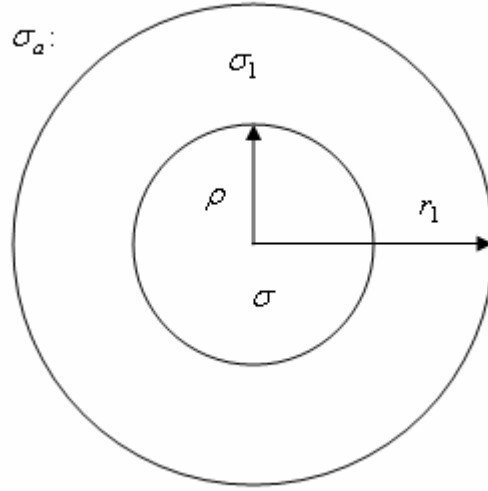
Figure 4.1 Sphere and centrally located spherical inhomogeneity.

Potential distribution inside the sphere is given by

$$
V(r,\theta) = \begin{cases} \sum_{l=0}^{\infty} C_l r^l P_l(\cos\theta), & r < \rho \\ \sum_{l=0}^{\infty} (A_l r^l + B_l r^{-(l+1)}) P_l(\cos\theta), & \rho < r < 1 \end{cases}
\tag{4.3}
$$

Continuity on the inner boundary imposes:

$$
C_l \rho^l = A_l \rho^l + B_l \rho^{-(l+1)} .
\tag{4.4}
$$

Continuity of the normal component of current density on the inner boundary yields:

$$
\sigma l C_l \rho^{(l-1)} = \sigma_1 \left[l A_l \rho^{(l-1)} - (l+1) B_l \rho^{-(l+2)} \right].
\tag{4.5}
$$

Total current on the outer boundary gives:

$$
\int \sigma_1 \frac{\partial V}{\partial r}\bigg|_{r = r_1} P_l(\theta) 2\pi r_1^2 \sin\theta d\theta = J_{app}
\tag{4.6}
$$

where J_{app} is the total current applied from the boundary. Equation (4.6) can be rewritten as

$$
\frac{4\pi\sigma_1 r_1^2}{2l+1} \left(l A_l r_1^{l-1} - (l+1) B_l r^{-(l+2)} \right) = J_{app} .
\tag{4.7}
$$

47

By combining Equations (4.4), (4.5) and (4.7), following matrix equation is obtained

$$
\begin{bmatrix}
-1 & -\rho^{-(2l+1)} & 1 \\
-\sigma_1 & \sigma_1 \dfrac{l+1}{l}\rho^{-(2l+1)} & \sigma \\
1 & -\dfrac{l+1}{l}r_1^{-(2l+1)} & 0
\end{bmatrix}
\begin{bmatrix}
A_l \\ B_l \\ C_l
\end{bmatrix}
=
\begin{bmatrix}
0 \\
0 \\
\dfrac{2l+1}{l}\dfrac{1}{4\pi\sigma_1}r_1^{-(l+1)}J_{app}
\end{bmatrix}
\tag{4.8}
$$

or equivalently in short form

$$\mathbf{D.e=F}. \tag{4.9}$$

When Equation (4.9) is solved for **e** vector, coefficients of potential distribution in Equation (4.3) is obtained as

$$
A_l = \dfrac{\begin{vmatrix}
0 & -\rho^{-(2l+1)} & 1 \\
0 & \sigma_1 \dfrac{l+1}{l}\rho^{-(2l+1)} & \sigma \\
\dfrac{2l+1}{l}\dfrac{1}{4\pi\sigma_1}r_1^{-(l+1)}J_{app} & -\dfrac{l+1}{l}r_1^{-(2l+1)} & 0
\end{vmatrix}}{|D|}
\tag{4.10.a}
$$

$$
B_l = \dfrac{\begin{vmatrix}
-1 & 0 & 1 \\
-\sigma_1 & 0 & \sigma \\
1 & \dfrac{2l+1}{l}\dfrac{r_1^{-(l+1)}}{4\pi\sigma_1}J_{app} & 0
\end{vmatrix}}{|D|}
\tag{4.10.b}
$$

$$
C_l = \dfrac{\begin{vmatrix}
-1 & -\rho^{-(2l+1)} & 0 \\
-\sigma_1 & \sigma_1 \dfrac{l+1}{l}\rho^{-(2l+1)} & 0 \\
1 & -\dfrac{l+1}{l}r_1^{-(2l+1)} & \dfrac{2l+1}{l}\dfrac{r_1^{-(l+1)}}{4\pi\sigma_1}J_{app}
\end{vmatrix}}{|D|}
\tag{4.10.c}
$$

where

$$|D| = \begin{vmatrix} -1 & -\rho^{-(2l+1)} & 1 \\ -\sigma_1 & \sigma_1 \dfrac{l+1}{l}\rho^{-(2l+1)} & \sigma \\ 1 & -\dfrac{l+1}{l}r_1^{-(2l+1)} & 0 \end{vmatrix} = \dfrac{l+1}{l}r_1^{-(2l+1)}(\sigma_1 - \sigma) - \rho^{-(2l+1)}\left(\sigma_1 \dfrac{l+1}{l} + \sigma\right).$$

Equations (4.10) can be re-organized as

$$A_l = -\frac{2l+1}{l}\frac{r_1^{-(l+1)}}{4\pi\sigma_1}J_{app}\left[\sigma\rho^{-(2l+1)} + \sigma_1\frac{l+1}{l}\rho^{-(2l+1)}\right]\bigg/|D| \qquad (4.11.a)$$

$$B_l = \frac{2l+1}{l}\frac{r_1^{-(l+1)}}{4\pi\sigma_1}J_{app}\left[\sigma - \sigma_1\right]\bigg/|D| \qquad (4.11.b)$$

$$C_l = -\frac{2l+1}{l}\frac{r_1^{-(l+1)}}{4\pi\sigma_1}J_{app}\left[\sigma\frac{l+1}{l}\rho^{-(2l+1)} + \sigma_1\rho^{-(2l+1)}\right]\bigg/|D| \qquad (4.11.c)$$

To simplify the analysis, let background conductivity is equal to 1 ($\sigma_1 = 1$) and background sphere radius is also equal to 1 ($r_1 = 1$). Then Equations (4.11) turn into the following form

$$A_l = -\frac{2l+1}{l}\frac{1}{4\pi}J_{app}\rho^{-(2l+1)}\left[\sigma + \frac{l+1}{l}\right]\bigg/|D| \qquad (4.12.a)$$

$$B_l = \frac{2l+1}{l}\frac{1}{4\pi}J_{app}\left[\sigma - 1\right]\bigg/|D| \qquad (4.12.b)$$

$$C_l = -\frac{2l+1}{l}\frac{1}{4\pi}J_{app}\rho^{-(2l+1)}\left[\frac{l+1}{l} + 1\right]\bigg/|D| \qquad (4.12.c)$$

and

$$|D| = \frac{l+1}{l}(1-\sigma) - \rho^{-(2l+1)}\left(\frac{l+1}{l} + \sigma\right).$$

On the other hand, current density distribution is obtained from potential distribution as

$$\vec{J} = -\sigma\nabla V \qquad (4.13)$$

where

$$\nabla = \vec{a}_r\frac{\partial}{\partial r} + \vec{a}_\theta\frac{1}{r}\frac{\partial}{\partial\theta}.$$

If $r < \rho$, then conductivity is equal to σ and scalar current density components at (r, θ) point are expressed as

$$j_r(r,\theta,\sigma_a) = -\sigma \sum_{l=0}^{\infty} C_l l r^{(l-1)} P_l(\cos\theta) \qquad (4.14.a)$$

$$j_\theta(r,\theta,\sigma_a) = \sigma \frac{1}{r} \sum_{l=0}^{\infty} C_l r^l P_l'(\cos\theta) \sin\theta . \qquad (4.14.b)$$

If $\rho < r < 1$, then conductivity is equal to 1 and scalar current density components at (r,θ) point are expressed as

$$j_r(r,\theta,\sigma_a) = -\sum_{l=0}^{\infty} \left[A_l l r^{(l-1)} - B_l(l-1)r^{-(l+2)} \right] P_l(\cos\theta) \qquad (4.14.c)$$

$$j_\theta(r,\theta,\sigma_a) = \frac{1}{r} \sum_{l=0}^{\infty} \left[A_l r^l + B_l r^{-(l+1)} \right] P_l'(\cos\theta) \sin\theta . \qquad (4.14.d)$$

As the second step, consider background sphere alone as shown in Figure 4.2. Conductivity distribution inside the sphere is homogeneous.
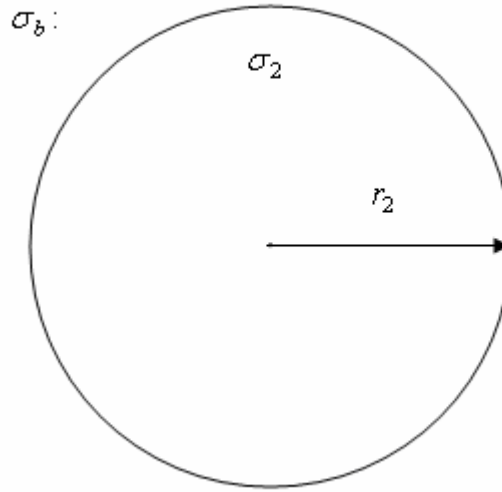
Figure 4.2 Homogeneous background sphere alone.

Potential distribution is given by

$$V(r,\theta) = \sum_{l=0}^{\infty} G_l r^l P_l(\cos\theta) . \qquad (4.15)$$

This time, there is only outer boundary, current on this boundary imposes

50

$$\int \sigma_2 \left. \frac{\partial V}{\partial r} \right|_{r=r_2} P_l(\cos\theta) 2\pi r_2^2 \sin\theta d\theta = J_{app}. \qquad (4.16)$$

After re-writing the Equation (4.16), following expression is obtained

$$\frac{4\pi\sigma_2 r_2^2}{2l+1} \left(l G_l r_2^{(l-1)} \right) = J_{app}, \qquad (4.17)$$

then

$$G_l = \frac{2l+1}{l} \frac{r_2^{-(l+1)}}{4\pi\sigma_2} J_{app}. \qquad (4.18)$$

Parallel to the first step, conductivity and radius is both equal to 1. Thus Equation (4.18) is further simplified as

$$G_l = \frac{2l+1}{l} \frac{1}{4\pi} J_{app}. \qquad (4.19)$$

Scalar components of the current density at (r, θ) point are expressed as

$$j_r(r,\theta,\sigma_b) = -\sum_{l=0}^{\infty} G_l l r^{(l-1)} P_l(\cos\theta) \qquad (4.20.\text{a})$$

$$j_\theta(r,\theta,\sigma_b) = \frac{1}{r} \sum_{l=0}^{\infty} G_l r^l P_l'(\cos\theta) \sin\theta. \qquad (4.20.\text{b})$$

Based on the distinguishability definition in Chapter 2, distinguishability is defined for 3-D sphere with centrally located perturbation as

$$D = \left\| \vec{B}(\sigma_a) - \vec{B}(\sigma_b) \right\| > \varepsilon. \qquad (4.21)$$

Change in z component of magnetic flux density at (r, θ) point due to existence of the inhomogeneity is calculated as

$$
\begin{aligned}
&B_z(r,\theta,\sigma_a) - B_z(r,\theta,\sigma_b) \\
&= \frac{\mu_0}{4\pi} \int \frac{j_r(r',\theta',\sigma_a)r\sin(\theta-\theta') + j_\theta(r',\theta',\sigma_a)(r'-r\cos(\theta-\theta'))}{R^3} ds' \\
&\quad - \frac{\mu_0}{4\pi} \int \frac{j_r(r',\theta',\sigma_b)r\sin(\theta-\theta') + j_\theta(r',\theta',\sigma_b)(r'-r\cos(\theta-\theta'))}{R^3} ds'
\end{aligned} \qquad (4.22)
$$

$$
\begin{aligned}
&\left\| B_z(r,\theta,\sigma_a) - B_z(r,\theta,\sigma_b) \right\| \\
&= \frac{\mu_0}{4\pi} \left\| \int \frac{\left[j_r(r',\theta',\sigma_a) - j_r(r',\theta',\sigma_b) \right] r\sin(\theta-\theta'))}{R^3} ds' \right. \\
&\quad \left. + \frac{\mu_0}{4\pi} \int \frac{\left[j_\theta(r',\theta',\sigma_a) - j_\theta(r',\theta',\sigma_b) \right] (r'-r\cos(\theta-\theta'))}{R^3} ds' \right\|
\end{aligned} \qquad (4.23)
$$

Based on Equation (4.23), distinguishable region for centrally located spherical perturbation is shown darker in Figure 4.3. In this case, measurement precision (ε) is taken as 0.0001 and summations in Equations (4.14) and (4.20) are upper limited to $N = 100$ terms. Distinguishability as a function of inhomogeneity conductivity (σ), radius of inhomogeneity (ρ) and measurement precision (ε) is illustrated in Figure 4.4.
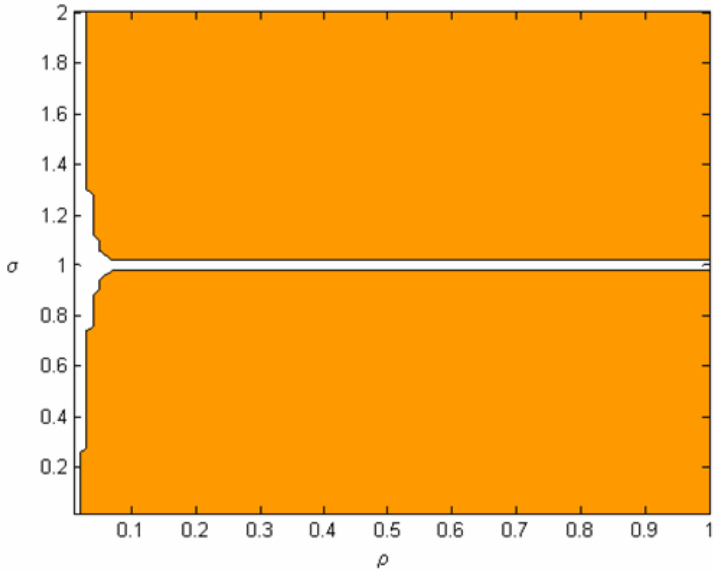
Figure 4.3 Distinguishability for sphere with centrally located spherical inhomogeneity when ε is equal to 0.0001 and N is equal to 100.
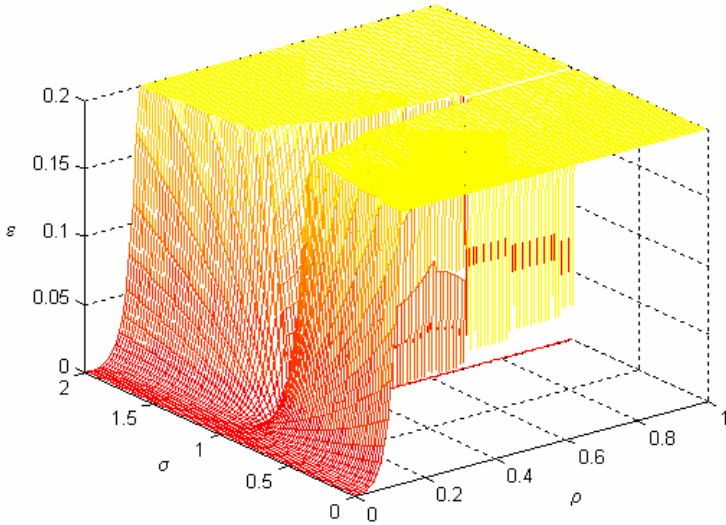
Figure 4.4 Distinguishability function for sphere with centrally located spherical inhomogeneity when N is equal to 100.

For the same conditions, 2-D defined in Chapter 2 and 3-D distinguishability values can be compared. When $N = 100$ and $\varepsilon = 0.0001$, distinguish abilities for 2-D and 3-D cases are plotted in Figure 4.5. The 2-D case has better distinguishability, since given amount of current passes through surface. However in 3-D case, the same amount of current passes through the volume.
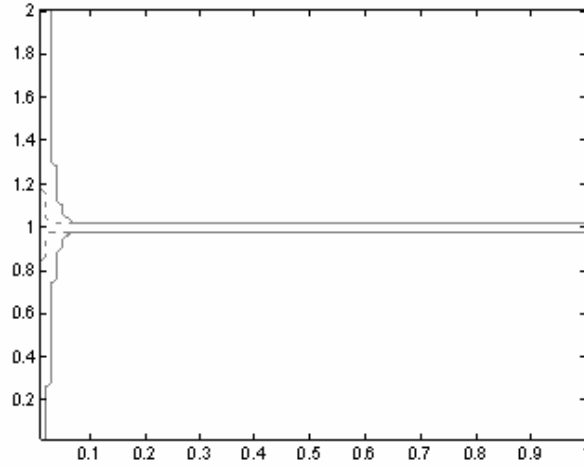
Figure 4.5 3-D (solid) and 2-D (dashed) distinguishability values, when $N = 100$ and $\varepsilon = 0.0001$.

4.3. Determination of Optimum Current Injection Strategy for Sphere with Concentric Inhomogeneity

Distinguishability for a sphere with azimuthal symmetry is defined at a point by Equation (4.23) in the previous section. Total distinguishability is the sum of all points as

$$\Delta B = \sum_{l=1}^{K} |\Delta B_l| \qquad (4.24)$$

where $|\Delta B_l|$ is the distinguishability at the lth point.

The optimization problem may be stated as:

$$\text{maximise } D = \Delta B$$

$$\text{s.t. } \frac{1}{2} \int |j(\theta)|^2 2\pi r_1^2 \sin\theta d\theta = 1 \text{ (total injected current is equal to 1)} \quad (4.25)$$

$$\text{where } j(\theta) = \sum_{l=0}^{\infty} J_l P_l(\cos\theta).$$

In this problem, coefficients of $j(\theta)$ namely J_l are optimized. Centrally located inhomogeneity is assumed to have conductivity of 10 and radius of 0.5 for simplicity. Coefficients of $j(\theta)$ are limited to N terms. The problem is solved numerically to determine best current injection strategy. In the solution, exterior penalty and Newton methods are applied. Different N values are assigned to observe the effects on the resulting pattern. In Figure 4.6, resulting patterns are presented. Both patterns have two peaks, one with positive amplitude and other with negative amplitude. Peaks are 180 degrees apart. When N is getting larger, peaks are getting narrower in width and higher in amplitude. This implies that current pattern converges to opposite drive. Resulting current injection pattern is shown in Figure 4.7 and Figure 4.8.
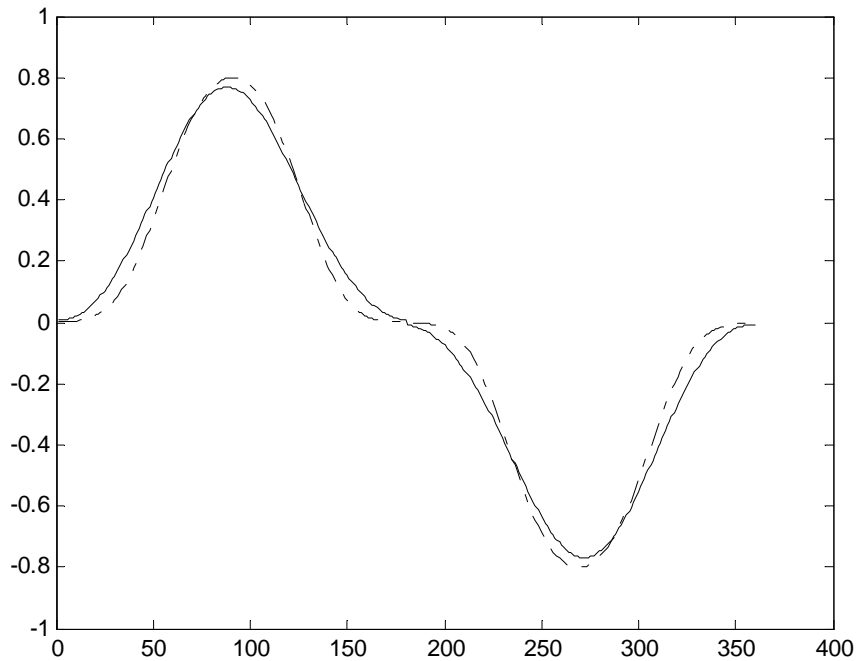
Figure 4.6 Current injection patterns with N equals to 5 (solid) and 8 (dash-dot).
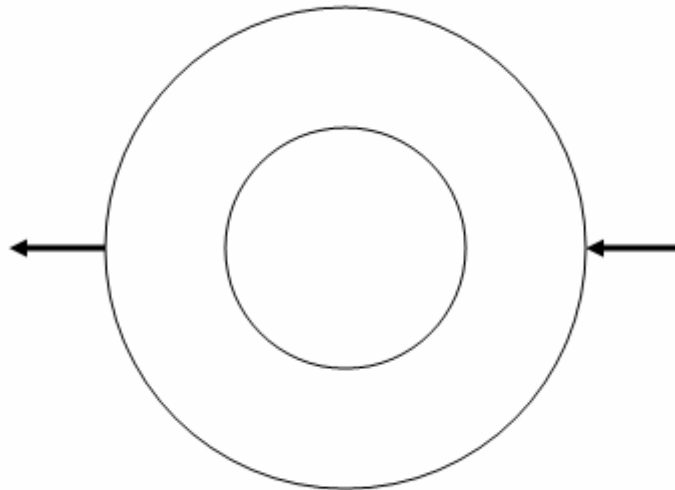
Figure 4.7 Optimum current geometry is opposite drive for sphere with azimuthal symmetry, 2-D slice view.
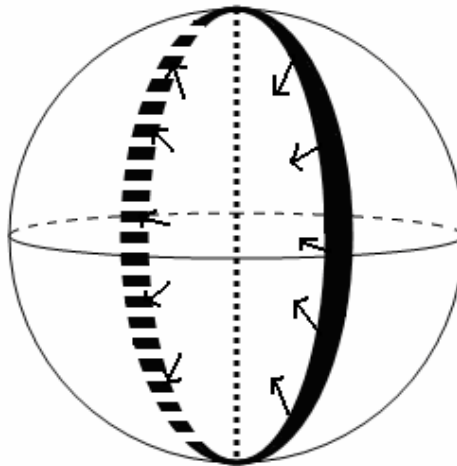
Figure 4.8 Optimum current geometry is opposite drive for sphere with azimuthal symmetry, 3-D view.

4.4. Discussion

In this chapter, MREIT distinguishability measure is calculated analytically for a sphere with azimuthal symmetry. Distinguishable and indistinguishable regions are obtained and illustrated in Figure 4.4. When measurement precision gets larger then

indistinguishable region increases. Based on these results, optimum current injection geometry is found as opposite drive and current pattern is shown for sphere with azimuthal symmetry in Figure 4.8. For 2-D circular object, optimum current injection pattern is found as opposite drive found in Chapter 3. These results are brought together and listed as the current injection principles in Chapter 5.

CHAPTER 5

REGIONAL IMAGE RECONSTRUCTION

5.1.   Introduction

Optimum current injection patterns are obtained in Chapter 3 and Chapter 4 for 2-D and 3-D geometries accordingly. Based on these results, current injection principles are summarized as

   i.   inject current with opposite drive

   ii.   inject current with small electrodes

  iii.   inject current such that drive axis (current injection axis) passing through the center of inhomogeneity

Care is required in applying principle ii, because large current density electrodes yield application of large amount of current through small area which could harm the patient. Thus patient safety is another constraint in injecting current into the body.

In this chapter, above principles are combined to form the basis of image reconstruction approach namely "Regional Image Reconstruction" (RIR). This new image reconstruction technique is interested in current injection principles and resulting image reconstruction steps. Hence, it could be used with any MREIT image reconstruction algorithm to obtain better images.

In Section 5.2, method of Regional Image Reconstruction is given. In Section 5.3, Regional Image Reconstruction is explained on a simple square geometry with two square shaped inhomogeneities inside. In the same section, performance of RIR

with noisy data is shown. In Section 5.4, RIR technique is applied to the Shepp-Logan head phantom with and without added noise.

5.2. Regional Image Reconstruction Method

The main idea behind Regional Image Reconstruction is to reconstruct conductivity distribution for a specific region for an applied current pattern. Therefore, for each current pattern, determination of best region of reconstruction is required. This is done by considering the current density distribution. If current density lines are strong which means SNR is high, then error in magnetic flux density values is small. When current density lines are weak or almost null, then SNR is lower and error in the reconstructed magnetic flux density is higher.

Current injection patterns and current density lines are shown in Figure 3.7 and Figure 3.8. For the opposite drive in Figure 3.7, reconstructing conductivity for bottom or top part of the background body includes more error, since current density lines are weak there. Similarly, for the adjacent drive in Figure 3.8, reconstructing conductivity for left part includes much more error, since current density lines are quite weak or almost zero in some parts.

Hence steps of RIR are as follows:
1. Take a current injection pattern.
    a. Determine the region of interest. That means where the current density distribution is strong. For the opposite drive, region of interest is field near the drive axis. Whereas for the adjacent drive, the region that is near the electrodes is the region of interest.
    b. Reconstruct conductivity for region of interest.
2. Reconstruct the whole image by combining regional conductivities. If region of interests are overlapping, then in the cross sections take the mean.

Applying RIR together with optimum current injection principles is proposed for best results. Because on the one side, optimum current injection principles provides best current density distributions, on the other side RIR uses this best distribution to

obtain conductivity image. If reconstruction of conductivity for a region of interest is not possible, then conductivity can be reconstructed for the whole body and just the region of interest is taken. In the following sections, optimum current injection principles and RIR are applied to a simple square geometry and to a complex Shepp Logan Head Phantom.

5.3. Application of RIR on Square Geometry

Square body with two perturbations is shown in Figure 5.1. Size of the background body is $2m \times 2m$, inhomogeneity at top-right is $0.4m \times 0.4m$ and inhomogeneity at bottom-left is $0.3m \times 0.3m$. Depths of conductors are the same and equal to $1m$. Conductivities of these three objects are 10, 2 and 4 accordingly. Four different current patterns are applied namely A1 to A4. Current density is $10A/m^2$, size of the electrodes is $0.1m \times 1m$, and then applied current is $1A$ in total.
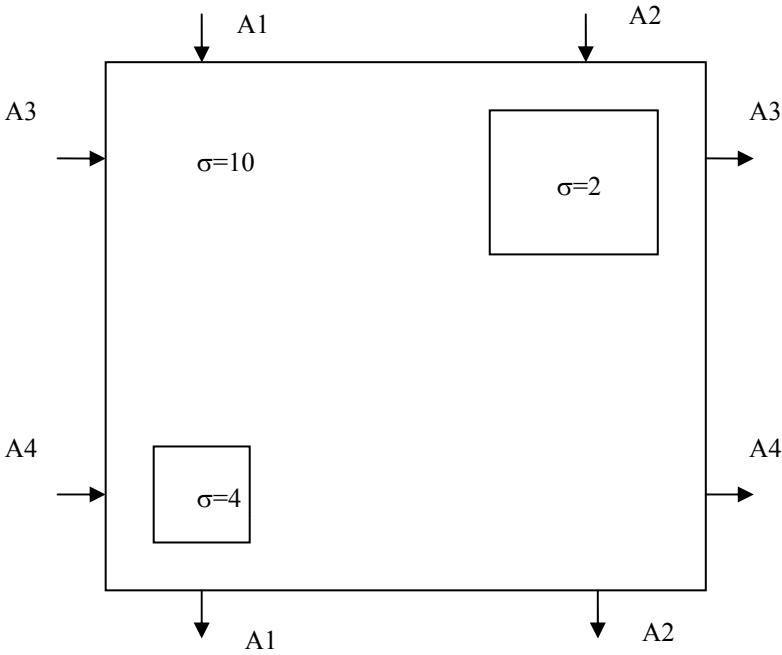
Figure 5.1 Square body with two perturbations. A1-A4 are injection currents patterns. Arrows show current injection points.

Each current injection pattern is applied separately and conductivity distribution inside is obtained by utilizing Equipotential Projection-Based MREIT algorithm

proposed by Eyüboğlu *et al* [8] and Özdemir *et al* [48]. Resulting conductivity image is obtained with two different ways:

- **First approach (No regional reconstruction):** In this way, resulting conductivity distribution is the mean of all conductivity distributions found after injecting current patterns separately. Final conductivity image is sketched in Figure 5.2.

Errors are calculated according to the definition

$$\varepsilon_\sigma = \sqrt{\frac{1}{N}\sum_{j=1}^{N}\frac{(\sigma_{jt}-\sigma_{jr})^2}{\sigma_{jt}^{\ 2}}} \times 100\% \qquad (5.1)$$

where σ_{jt} and σ_{jr} are true and reconstructed conductivity of the jth element. Whereas N is the total number of pixels in the object. For the first approach, errors are calculated for background, top-right and bottom-left objects as 25.2%, 19.2% and 17% respectively.
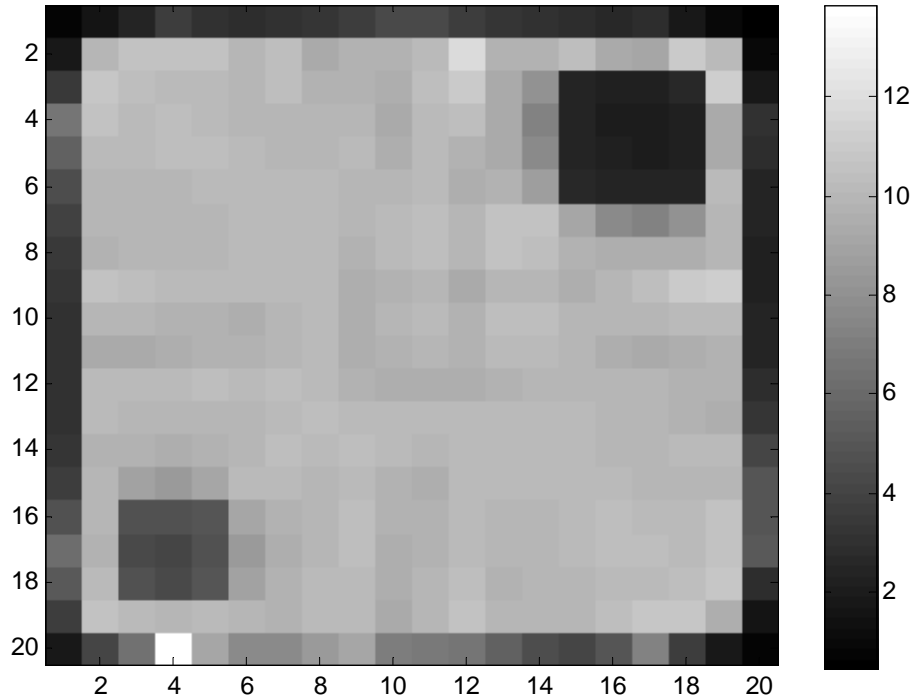
Figure 5.2 Conductivity image according to first approach with current of $1A$.

- **Second approach (Regional Image Reconstruction):** In this case, Equipotential Projection-Based MREIT algorithm is tuned such that conductivity is reconstructed for each current pattern just for the regions of interest. Because Equipotential Projection-Based MREIT allows regional reconstruction, however in some other MREIT algorithms, this could be difficult, then in such cases conductivity is reconstructed for the whole body and only relevant region is used in image reconstruction. For A1 pattern, conductivity is reconstructed for Region-I and III and the same approach is followed for other current injection patterns as in Figure 5.3. According to the current injection principles written in Section 5.1, conductivity of Region-I is equal to the mean of the conductivity distribution of A1 and A3. Similarly, for Region-II, A2 and A3 are utilized. Region-III and Region-IV are considered in the same way. Resulting conductivity distribution is illustrated in Figure 5.4. Errors in this approach are 25.8%, 19.4% and 17.1% for background, top-right and bottom-left objects correspondingly.
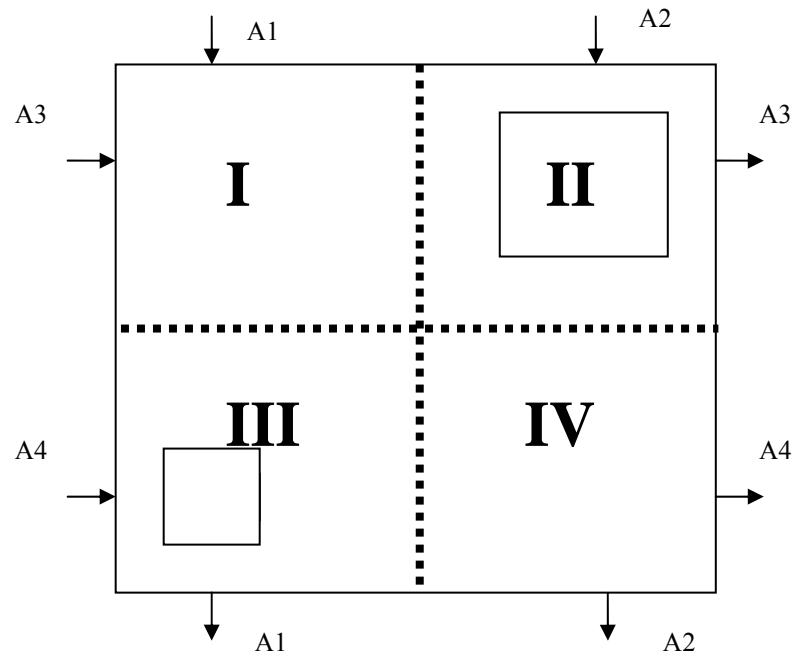
Figure 5.3 Regions of the object.
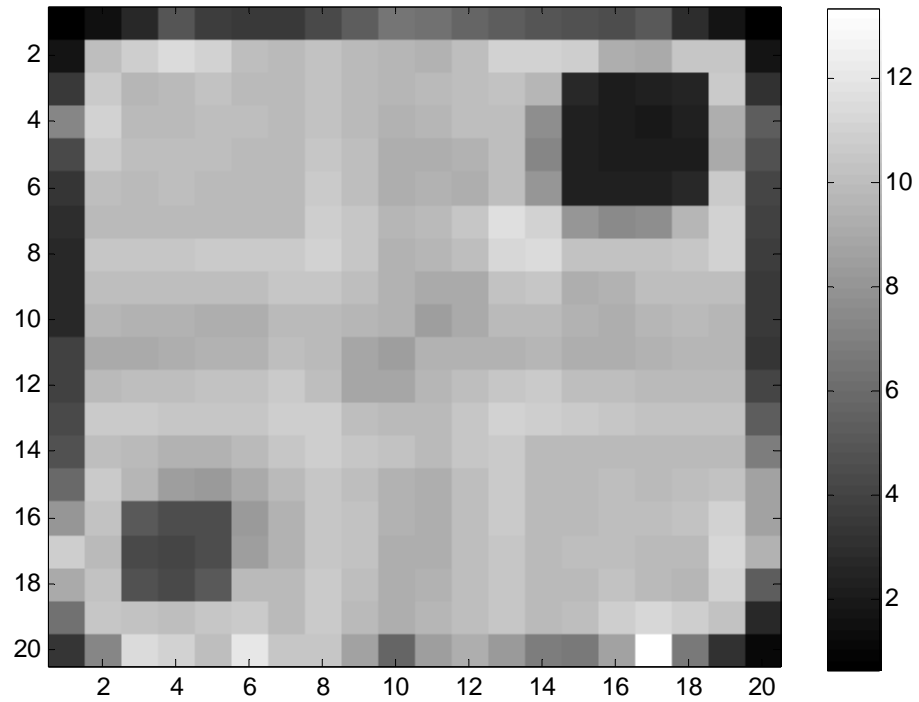
Figure 5.4 Conductivity image reconstruction according to RIR (second approach) with current of $1A$.

Effect of noise in resulting conductivity images is of interest. For each current injection pattern errors in different noise levels are listed in Table 5.1. Overall performances of 2 different ways above are listed in Table 5.2, Table 5.3 and Table 5.4 for signal to noise ratio (SNR) levels of 13dB, 20dB and 30dB respectively. When there is no noise or little noise such as SNR of 30dB, then all three approaches perform similar and there is no reasonable difference between resulting error levels. However, when noise level gets larger as SNR gets smaller as 20dB and 13dB, then Regional Image Reconstruction approach performs better especially for inhomogeneities. When SNR is 13dB, for top-right object, noise level of no regional reconstruction is as double as noise level produced by RIR approach. Similarly for bottom-left object, RIR approach again shows better performances than first approach. For the background object, both ways generated similar error rates.

Table 5.1 Errors for different noise levels ($1A$)

SNR	Current Injection Pattern	Top-Right Object	Bottom-Left Object	Background Object
No Noise	A1	% 20.93	% 18.62	% 26.40
No Noise	A2	% 22.23	% 18.51	% 26.01
No Noise	A3	% 22.27	% 18.70	% 25.89
No Noise	A4	% 20.66	% 19.05	% 26.62
30 dB	A1	% 33.78	% 19.22	% 26.64
30 dB	A2	% 22.86	% 30.31	% 26.52
30 dB	A3	% 21.35	% 20.28	% 26.49
30 dB	A4	% 34.46	% 18.41	% 26.67
20 dB	A1	% 36.72	% 19.07	% 27.55
20 dB	A2	% 22.38	% 44.92	% 28.73
20 dB	A3	% 22.60	% 58.63	% 28.28
20 dB	A4	% 40.94	% 17.44	% 27.94
13 dB	A1	% 53.83	% 22.54	% 29.64
13 dB	A2	% 28.35	% 42.77	% 30.90
13 dB	A3	% 24.13	% 85.95	% 32.64
13 dB	A4	% 69.99	% 21.84	% 37.23

Table 5.2 Errors for 13dB noise level ($1A$)

Image Reconstruction Approach	Top-Right Object	Bottom-Left Object	Background Object
First approach (No regional reconstruction)	% 38.1	% 26.9	% 26.9
Second approach (Regional Image Reconstruction)	% 18.9	% 18.6	% 26.1

Table 5.3 Errors for 20dB noise level ($1A$)

Image Reconstruction Approach	Top-Right Object	Bottom-Left Object	Background Object
First approach (No regional reconstruction)	% 31.7	% 22.8	% 26.4
Second approach (Regional Image Reconstruction)	% 19.7	% 17.7	% 25.8

Table 5.4 Errors for 30dB noise level ($1A$)

Image Reconstruction Approach	Top-Right Object	Bottom-Left Object	Background Object
First approach (No regional reconstruction)	% 22.7	% 18.7	% 25.6
Second approach (Regional Image Reconstruction)	% 18.8	% 17.1	% 25.7

5.4. Application of RIR on Shepp-Logan Head Phantom

As a complex and realistic geometry Shepp-Logan head phantom model is chosen [66]. The cross section is illustrated in Figure 5.5 and original conductivity distribution is presented in Figure 5.6. Detailed geometrical specifications and conductivity values are listed in Table 5.5. In this table, conductivities are true values of head tissues as presented in Table 5.6 [67].
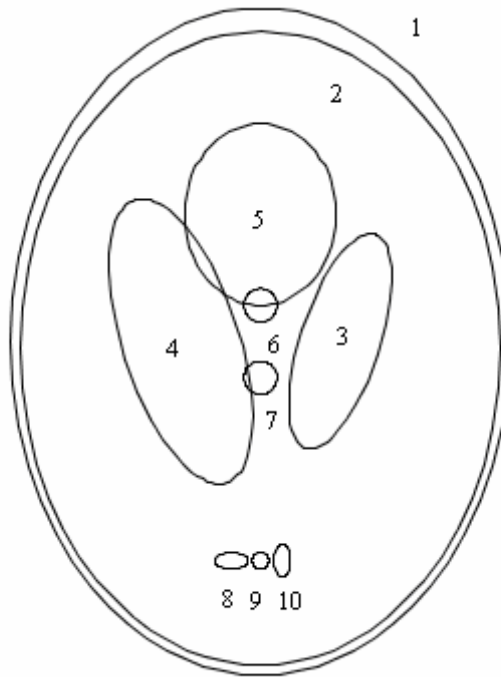
Figure 5.5 Cross section of Shepp-Logan head phantom.
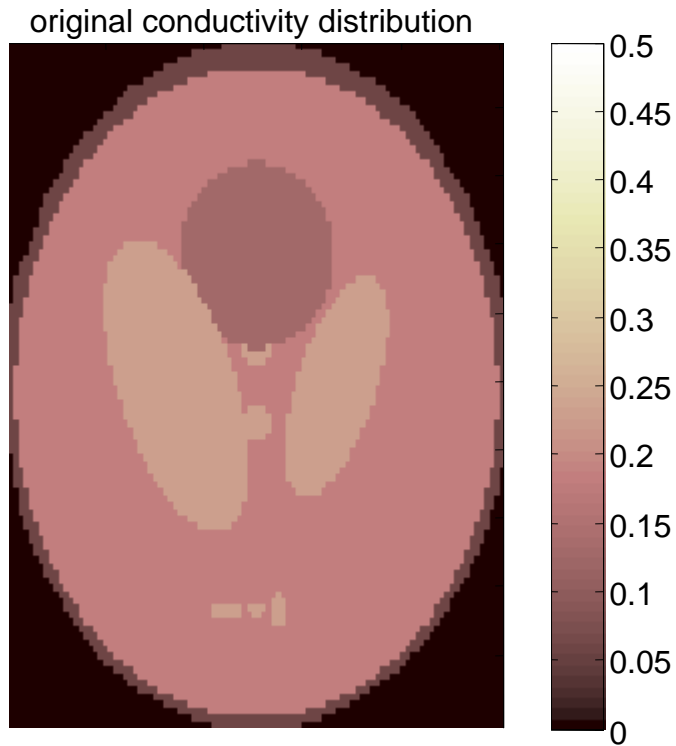
Figure 5.6 Conductivity distribution of Shepp-Logan head phantom.

Table 5.5 Geometry and conductivity of Shepp-Logan phantom.

Object	Radius (m)			Center (m)			Rotation (°)			Conductivity (S/m)
	r_x	r_y	r_z	x_0	y_0	z_0	E_x	E_y	E_z	
1	0.69	0.92	0.81	0	0	0	0	0	0	0.06
2	0.66	0.87	0.78	0	-0.02	0	0	0	0	0.18
3	0.11	0.31	0.22	0.22	0	0	-18	0	10	0.23
4	0.16	0.41	0.28	-0.22	0	0	18	0	10	0.23
5	0.21	0.25	0.41	0	0.35	-0.15	0	0	0	0.13
6	0.05	0.05	0.05	0	0.1	0.25	0	0	0	0.23
7	0.05	0.05	0.05	0	-0.1	0.25	0	0	0	0.23
8	0.05	0.02	0.05	-0.08	-0.6	0	0	0	0	0.23
9	0.02	0.02	0.02	0	-0.6	0	0	0	0	0.23
10	0.02	0.05	0.02	0.06	-0.6	0	0	0	0	0.23

Table 5.6 Conductivities of brain tissues.

Brain Tissue	Conductivity (S/m)
Average bone	0.06
Average brain	0.18
Grey matter	0.23
White matter	0.13

In the simulation, 8 electrodes are connected onto the phantom as shown in Figure 5.7. Electrode size is $0.1m \times 1m$. Total current is kept small as $0.01A$ and current density is $0.1A/m^2$, since applying smaller currents and obtaining reasonable images with MREIT is one of the main purposes of the thesis.
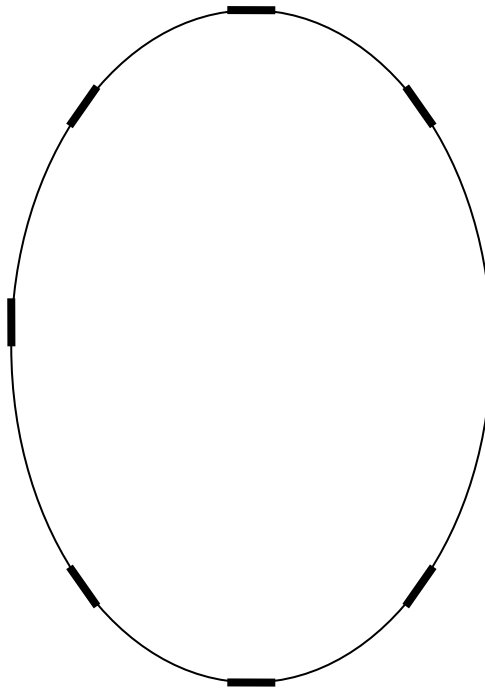
Figure 5.7 Electrodes on the Shepp-Logan head phantom.

As stated in Chapter 3 and at the beginning of this chapter, current is injected as opposite drive. Besides, in Chapter 3, it is found that adjacent drive produces reasonable results especially for eccentrically located inhomogeneities. In Shepp-Logan head phantom, there are many eccentric inhomogeneities, therefore adjacent drives are also applied by employing the same electrodes. Total of 8 current injection patterns are utilized as presented in Figure 5.8 and Figure 5.9.
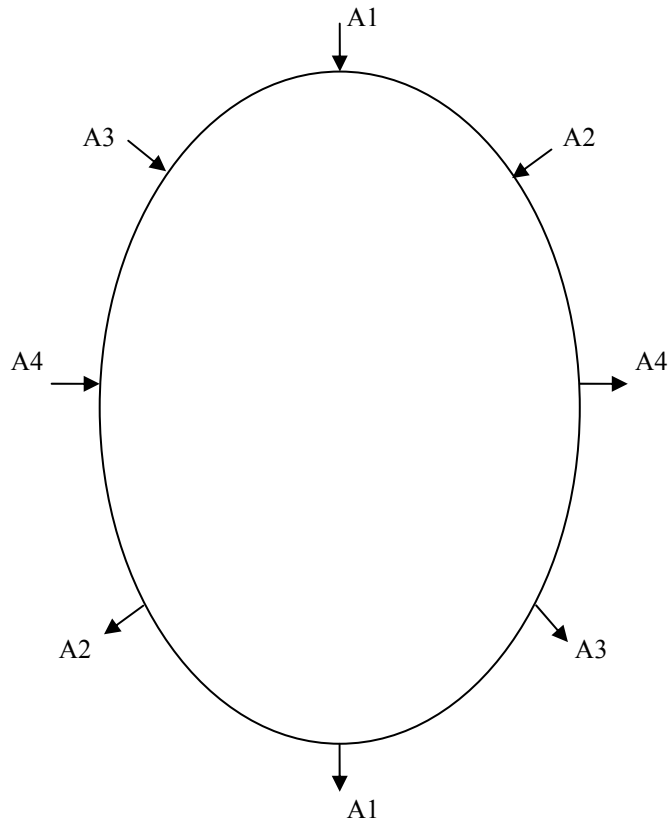
Figure 5.8 Opposite current injection patterns.
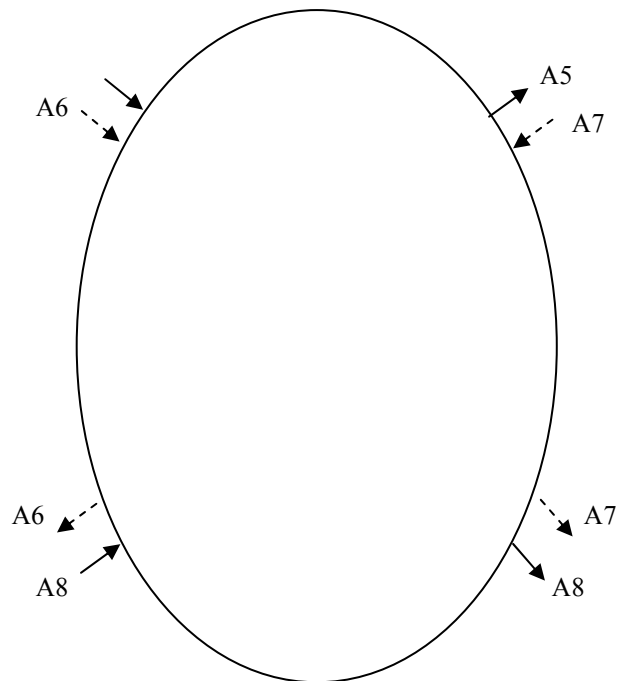
Figure 5.9 Adjacent current injection patterns.

Each current injection pattern is applied separately and conductivity distribution inside is obtained by utilizing Equipotential Projection-Based MREIT algorithm proposed by Eyüboğlu *et al* [8] and Özdemir *et al* [48]. Total of 10000 pixels are utilized in the image reconstruction, by this way even small objects inside the phantom are reconstructed. Similar to Section 5.2, regional image reconstruction and conventional image reconstruction ways are compared:

- **First approach (no regional image reconstruction):** In this way, resulting conductivity distribution is the mean of all conductivity distributions found after injecting all of the 8 current patterns separately. Final conductivity image is sketched in Figure 5.10.
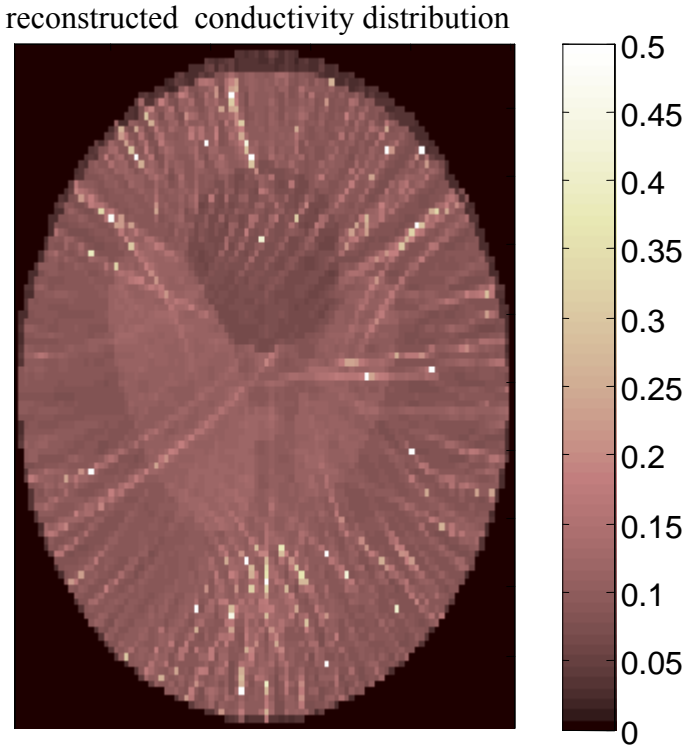
Figure 5.10 Conductivity image according to first approach with current of $0.01A$.

- **Second approach (no regional image reconstruction):** In this way, resulting conductivity distribution is the mean of all conductivity distributions found after injecting the 4 opposite current patterns separately. Final conductivity image is sketched in Figure 5.11.
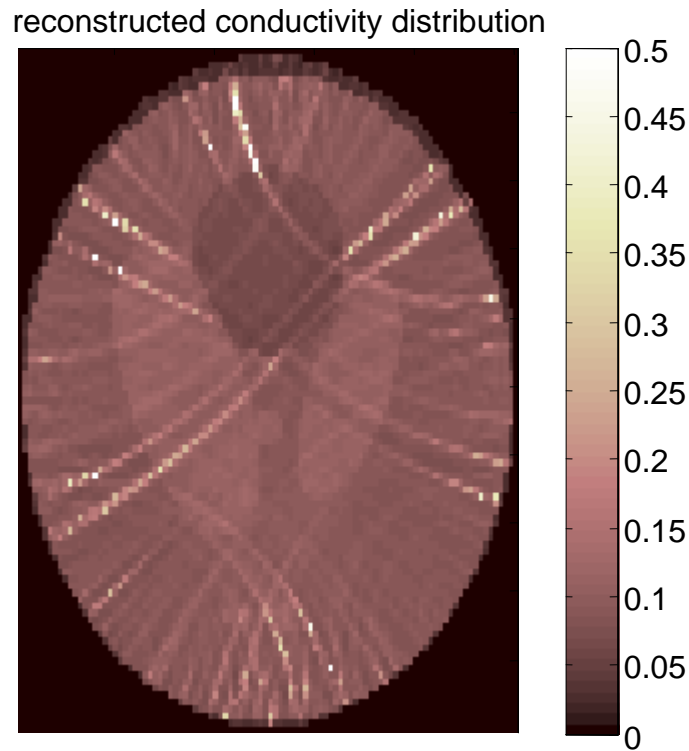
Figure 5.11 Conductivity image according to second approach with current of $0.01A$.

- **Third approach (Regional Image Reconstruction):** In this case each current injection pattern is utilized in reconstruction of a specific region. As the first step, Shepp-Logan phantom is divided into sub-regions as in Figure 5.12. Which current injection pattern is responsible for image reconstruction of which part of the phantom is listed in Table 5.7. Based on these assignments, resulting reconstructed conductivity image is found as in Figure 5.13.
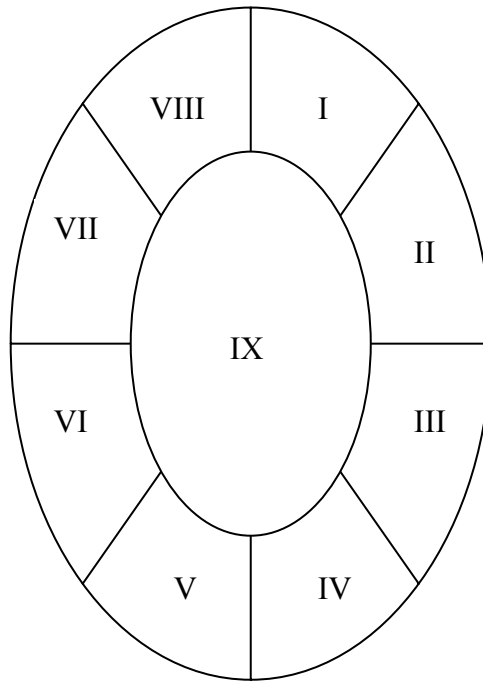
Figure 5.12 Regions of the phantom.

Table 5.7 Region assignments for current injection patterns.

Current Patterns	Regions of the phantom								
	I	II	III	IV	V	VI	VII	VIII	IX
A1	√			√	√			√	√
A2	√	√			√	√			√
A3			√	√			√	√	√
A4		√	√			√	√		√
A5	√	√					√	√	√
A6					√	√	√	√	√
A7	√	√	√	√					√
A8			√	√	√	√			√

reconstructed conductivity distribution

Figure 5.13 Conductivity image according to third approach (Regional Image Reconstruction) with current of $0.01A$.

Error of the reconstructed conductivity distribution for each object in the phantom is calculated according to Equation 5.1 and listed for both reconstruction ways in Table 5.8.

Table 5.8 Reconstructed conductivity errors.

Object	Conductivity (S/m)	Errors		
		First approach (No RIR)	Second approach (No RIR)	Third approach (RIR)
1	0.06	% 42	% 49	% 34
2	0.18	% 50	% 49	% 46
3	0.23	% 55	% 55	% 49
4	0.23	% 47	% 50	% 42
5	0.13	% 45	% 47	% 35
6	0.23	% 49	% 51	% 43
7	0.23	% 50	% 54	% 45
8	0.23	% 48	% 49	% 21
9	0.23	% 49	% 50	% 29
10	0.23	% 51	% 51	% 31

Utilization of RIR improves the image quality of the resulting conductivity distribution as can be observed in Figure 5.10, Figure 5.11 and Figure 5.13. Especially small objects in the bottom of the phantom are not easily recognizable in conventional case. Whereas, when RIR is utilized, all objects are easily recognizable. Error performances also show the improvement introduced by RIR as in Table 5.8. Two conventional cases are tried, on the one side all opposite and adjacent drives total of 8 drives are utilized together, on the other hand just opposite drives employed. Utilization of all drives provides better error performance than just opposite drive case.

In this analysis, noise free data are utilized. Addition of noise and decreasing SNR makes the resulting images worse. Since total applied current is small as $10mA$ whereas the size of the phantom is relatively big, addition of noise makes it more difficult to obtain reasonable reconstructed conductivity distribution. Noise performance analysis is done with higher current levels. Noise added data provides reasonable results on the order of $100mA$ and higher current levels let noise analysis possible. Overall noise performances of first and third approaches are listed in Table 5.9, Table 5.10 and Table 5.11. When SNR is 30dB which means noise level is small relative to signal level, Regional Image Reconstruction performs better in terms of error rates. However differences between error rates are not relatively high in this case. When SNR level decreases as 20dB and 13dB, the error rates increase in both cases. The increment in error rates is higher in conventional case especially for inhomogeneities. For example, for bottom small inhomogeneities the error rates are higher than %70 for conventional case for SNR level of 13dB. On the contrary for the same objects, RIR provides error rates of below %50.

Table 5.9 Errors for 13dB noise level ($100mA$)

Object	Conductivity (S/m)	Errors	
		First approach (No RIR)	Third approach (RIR)
1	0.06	% 56	% 51
2	0.18	% 59	% 54
3	0.23	% 62	% 53
4	0.23	% 58	% 51
5	0.13	% 59	% 48
6	0.23	% 64	% 53
7	0.23	% 66	% 49
8	0.23	% 75	% 48
9	0.23	% 71	% 44
10	0.23	% 73	% 46

Table 5.10 Errors for 20dB noise level ($100mA$)

Object	Conductivity (S/m)	Errors	
		First approach (No RIR)	Third approach (RIR)
1	0.06	% 55	% 49
2	0.18	% 56	% 52
3	0.23	% 59	% 52
4	0.23	% 57	% 50
5	0.13	% 56	% 45
6	0.23	% 62	% 50
7	0.23	% 63	% 47
8	0.23	% 70	% 46
9	0.23	% 66	% 43
10	0.23	% 69	% 44

Table 5.11 Errors for 30dB noise level ($100mA$)

Object	Conductivity (S/m)	Errors	
		First approach (No RIR)	Third approach (RIR)
1	0.06	% 52	% 47
2	0.18	% 51	% 48
3	0.23	% 55	% 51
4	0.23	% 52	% 49
5	0.13	% 51	% 43
6	0.23	% 57	% 47
7	0.23	% 55	% 45
8	0.23	% 58	% 45
9	0.23	% 56	% 41
10	0.23	% 54	% 40

5.5. Discussion

In this chapter, basic current injection and conductivity image reconstruction principles found in Chapter 3 are combined to form the Regional Image Reconstruction technique. RIR can be utilized with any MREIT algorithm as long as the algorithm permits the regional conductivity reconstruction.

As the first case, simple square geometry with two inhomogeneities inside is analyzed. In this case, when there is no noise, conventional way and RIR perform similar and errors are almost the same. When noise is added, RIR performs better especially in reconstruction of small inner inhomogeneities. When SNR is 13dB, conductivity error produced by RIR for inhomogeneities is half of the conventional approach.

As the second case, Shepp-Logan phantom with real tissue conductivities are studied. Total of $10mA$ current is applied and 8 current injection patterns are utilized. RIR again provides better resulting conductivity image and performs better in terms of error. Performance of RIR is more obvious for image reconstruction of inhomogeneities. When there is no noise, even with small current of $10mA$, bottom small inhomogeneities are easily recognizable from the resulting conductivity image. When noise is added, error performance of RIR is again better than the conventional case especially for inhomogeneities.

To sum up, utilization of current injection principles under the heading of RIR in Chapter 3, improves the quality of resulting conductivity image. Moreover RIR is not dependant on any specific MREIT technique. RIR can provide advantage especially in reconstruction of inner inhomogeneity conductivities.

CHAPTER 6

ANOTHER PERSPECTIVE TO CURRENT INJECTION: PULSE SEQUENCE OPTIMIZATION

6.1.   Introduction

Another aspect of current injection is the pulse sequence, since the current is injected in magnetic resonance pulse sequence. Applying current for longer periods within pulse sequence lets lower currents to be applied. From this point, it is also critical to locate the current pulse within pulse sequence.

In this chapter, gradient echo pulse sequence with current pulse is proposed for MREIT. In the following section, gradient echo sequence for MREIT is proposed and current injection interval is determined. Then spin echo and gradient echo MREIT pulse sequences are compared in terms of their capabilities of decreasing injected current.

6.2.   Gradient Echo Pulse Sequence with Current Pulse for MREIT

In current MREIT conductivity imaging modalities, the amplitude of current injected to the body is high. This prevents MREIT being a medical conductivity imaging modality. Therefore, decreasing the amplitude of injected current is of interest in MREIT. For this purpose, possibility of applying gradient echo pulse sequence is analyzed in this part. Consider the gradient echo pulse sequence shown in Figure 6.1. A RF pulse equal to or smaller than 90° is assumed. Instead of using a 180° RF pulse, a gradient pulse is used for refocusing thus decreasing the total sequence duration. Reduction of flip angle yields shorter time for T_1 recovery. By

this way, duration of the entire imaging time can be reduced. Flip angle of 15° causes a finite induction decay (FID) signal with amplitude corresponding to 25% of the FID amplitude obtained by a 90° RF pulse. Reduction in FID amplitude yields a decrement in current SNR that means there is a trade off between pulse sequence duration and current SNR. In order to compensate for this reduction, applied current should be increased in the same order. If applied current is below safety limits and the purpose is to decrease the entire imaging time, then decreasing flip angle helps. In the reverse case, to obtain smaller current levels, duration of the current pulse and complete echo pulse sequence should be increased.

Due to the refocusing gradient, gradient echo imaging is more sensitive to magnetic field inhomogeneities. On the other hand, spin-echo imaging is less affected by magnetic field inhomogeneities. Perturbations inside a body cause a distortion in current density distribution and so magnetic field created by the current. Gradient echo based MREIT imaging is more affected by this distortion than spin echo pulse sequence. However, gradient echo provides decrement in applied current amplitude and echo time, that limits the effect of magnetic field inhomogeneities on gradient echo based MREIT conductivity imaging.

In the proposed pulse sequence, slice selection, phase encoding and frequency encoding gradients are the same as in a typical gradient echo imaging pulse sequence in MRI. In addition to these time varying magnetic fields, current should be injected in order to obtain the conductivity image in MREIT. "In which time period should current be applied?" is an important question. If current is applied from the beginning of the RF pulse, due to long injection time lower current amplitudes can be applied. However, when current application overlaps with slice-selection or readout gradients, then slice or readout distortions occur [55]. Then current could be applied between slice selection and readout periods.

"How long the current could be applied?" is another question. Injected current creates a magnetic flux density and only the z-component is measured. When current is injected the signal expression of gradient echo is as follows

$$S(t) = \iint M(x,y)e^{j\delta(x,y)}e^{j\gamma B_z(x,y)T_c}e^{-j\gamma G_y ty}e^{-j(\gamma\int_0^t G_x dt')x}\,dxdy \qquad (6.1)$$

where $\delta(x,y)$: systematic phase error.

Equivalently the signal expression in Equation (6.1) can be re-written in k-space as

$$S(k_x,k_y) = \iint M(x,y)e^{j\delta(x,y)}e^{j\gamma B_z(x,y)T_c}e^{-j2\pi(k_x x+k_y y)}\,dxdy \qquad (6.2)$$

with inverse Fourier transform, MR images obtained as

$$M(x,y) = M(x,y)e^{j\delta(x,y)}e^{j\gamma B_z(x,y)T_c} \;. \qquad (6.3)$$

If current is applied once positive and once negative separately, Equation (6.3) can be modified as

$$\overset{+}{M^-}(x,y) = M(x,y)e^{j\delta(x,y)}e^{-j\gamma \overset{+}{B_z}(x,y)T_c} \;. \qquad (6.4)$$

Induced component of the magnetic flux density can be obtained from $\arg(M^+/M^-)$.
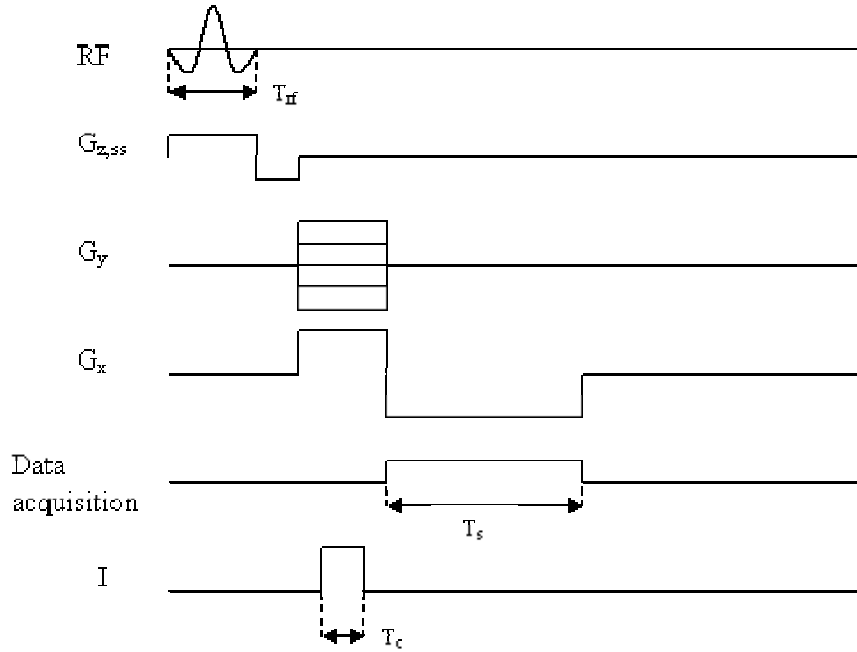
Figure 6.1 Gradient echo pulse sequence for MREIT.

Noise sources in gradient echo pulse sequence are resistance of the receiver coil and magnetic losses caused by conductivity as in spin echo case [55]. Therefore signal to noise ratio (SNR) is defined as in spin echo pulse sequence:

$$SNR = \psi_s \Delta x \Delta y \Delta z \sqrt{NT_s} \, M(x, y) \qquad (6.5)$$

where

ψ_S : system SNR

$\Delta x \Delta y \Delta z$: voxel volume

N : total number of excitations

M is assumed to contain independent and identically distributed complex Gaussian noise.

Standard deviation of measured B_Z for spin echo pulse sequence data was found as

$$\sigma_B = \frac{1}{\sqrt{2}\gamma T_c SNR} \qquad (6.6)$$

by Sadleir et al [51], [52]. Since signal and noise definitions are the same for gradient echo case, Equation (6.6) is equally valid for gradient echo case.

In gradient echo, magnetization is formulated as

$$M(x, y) = \frac{M_z^0 (1 - e^{-\frac{T_R}{T_1}})}{1 - \cos \alpha e^{-\frac{T_R}{T_1}}} \sin \alpha e^{-\frac{T_E}{T_2^*}} \qquad (6.7)$$

where

T_E : echo time

T_2^* : transversal relaxation time.

Therefore

$$SNR \propto \sqrt{T_s} \, \sin \alpha e^{-\frac{T_E}{T_2^*}} \quad \text{when} \quad T_E \ll T_R \ll T_1 \qquad (6.8)$$

Equation (6.6) is re-organized based on Equation (6.8):

$$\sigma_B \propto \frac{1}{T_c \sqrt{T_s} \sin \alpha} e^{\frac{T_E}{T_2^*}}. \qquad (6.9)$$

In order to determine the best duration of current injection strategy, timing diagram of the gradient echo sequence is shown in Figure 6.2 more closely.
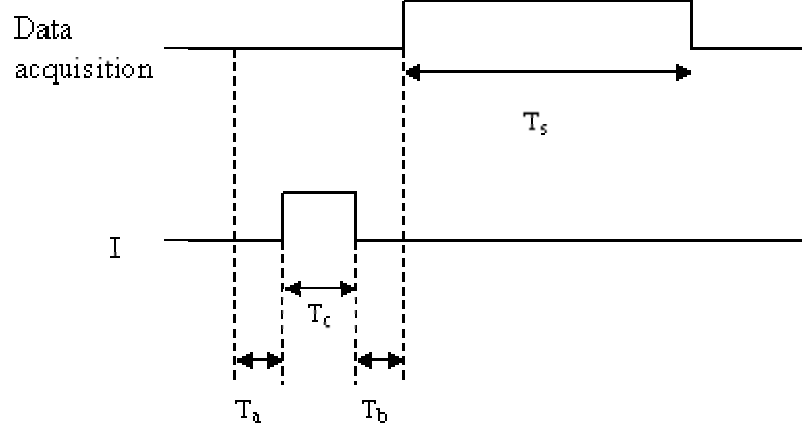
Figure 6.2 Closer look to current injection timing.

Echo time is expressed as

$$T_E = \frac{1}{2}T_{rf} + T_a + T_c + T_b + \frac{1}{2}T_s. \qquad (6.10)$$

From Equation (6.10), T_S can be obtained as

$$T_s = 2(T_E - \frac{1}{2}T_{rf} - T_a - T_b - T_c) \qquad (6.11)$$

and substituted into Equation (6.9). Then derivative of standard deviation expression with respect to T_c is taken to find the optimum current injection duration:

$$T_c^* = \frac{2}{3}(T_E - \frac{1}{2}T_{rf} - T_a - T_b). \qquad (6.12.a)$$

On the other hand, to maximize phase induced by current I, T_c should be as long as possible. Therefore T_a and T_b should converge to zero and therefore

$$T_c{}^* = \frac{2}{3}\left(T_E - \frac{1}{2}T_{rf}\right). \qquad\qquad (6.12.b)$$

Current patient safety regulations set a limit on the maximum amplitude of current that can be injected into a patient. On contrast, in order to obtain better conductivity images from MREIT, higher current values should be injected. To solve this problem, smaller currents for longer durations can be utilized. In spin echo pulse sequence for MREIT, injection of smaller currents with longer durations increases directly the total imaging time which is an unwanted situation in MREIT imaging. Gradient echo pulse sequence can overcome this problem. In gradient echo case without distorting total imaging time, current injection time can be increased as in Figure 6.3. G_x^+ and G_x^- need not to be the same in magnitude. Current is injected during T_x^+, therefore choosing smaller G_x^+ causes longer T_x^+. On contrast, T_x^- is kept smaller in order to keep the total echo time undistorted. Thus larger negative gradient is utilized as G_x^+. Based on these facts an optimization problem is formulated as

$$\text{maximize } T_c = T_x^- \qquad\qquad (6.13)$$

$$\text{such that } G_x^+ T_x^+ = \frac{1}{2}G_x^- T_x^-$$

$T_x^- + T_x^+ \leq T_{\lim it}$ (The sum can also be kept constant. However, keeping smaller than an upper limit is also valid. $T_{\lim it}$ is the boundary just before distorting total echo time. If this criterion is not used, then postponed echo and longer imaging duration is obtained.)

$FOV_x \geq FOV_{\lim it}$ (When manipulating echo sequence, field of view (FOV) should be higher than a determined limit, otherwise region cannot be imaged as a whole.)
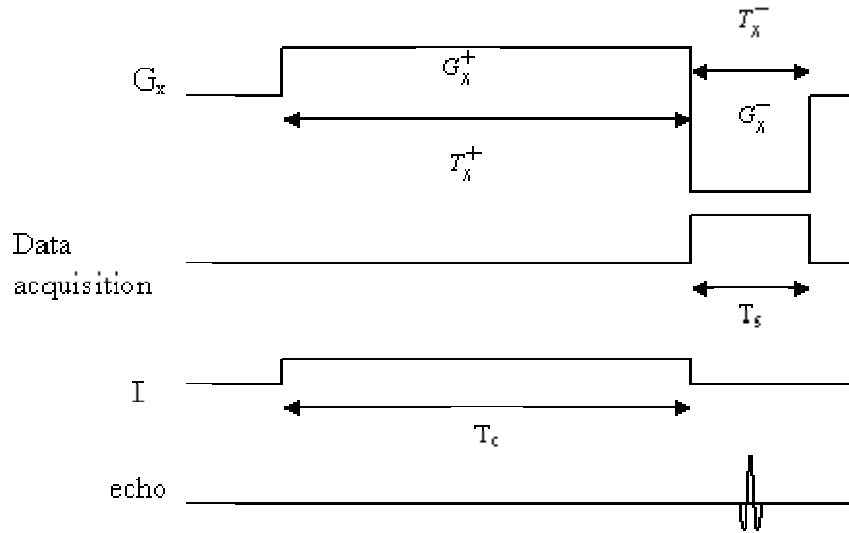
Figure 6.3 Timing diagram for smaller currents.

Field of view is related to bandwidth and applied gradient as

$$FOV_x = \frac{BW}{\gamma G_x}.$$ (6.14)

If G_x^- increases, then FOV decreases. If $T_x^- + T_x^+$ is kept constant, increasing T_x^+ by 10% decreases T_x^- by 10%. This causes an increment of 9% in G_x^- and decrement of 10% in FOV when bandwidth is kept constant.

Another important aspect to keep in mind when changing echo sequence timing is sharp change in the x gradient. When T_x^+ is increased too much, then G_x^- should be increased in the same order which causes a sharper change from G_x^+ to G_x^-. Sharp gradient changes cause eddy currents in the body that is not desired.

6.3. Comparison of GE and SE Based Pulse Sequences for MREIT

In order to see the relative performances of GE and SE in MREIT, typical parameters are considered. The comparison is executed for typical brain tissue parameters measured at 1.5 T [68] as shown in Table 6.1.

Table 6.1 Brain Tissue Parameters (at 1.5T)

Tissue	T_1(ms)	T_2(ms)	Relative spin density (ρ)
White matter	510	67	0.61
Gray matter	760	77	0.69
Cerebrospinal fluid	2650	280	1.00

In order to find conductivity image of brain according to the parameters given in Table 6.1, chosen parameters of GE an SE are shown in Table 6.2. The system signal to noise ratio (SNR) is assumed to be the same for both cases. In gradient echo, flip angle could be between 10-90°. However in this case, in order to compare current injection time with spin echo, longer repetition time (T_R) is required, therefore to compete with signal loss, highest possible flip angle is chosen as 90°. To make comparison under same conditions, the same echo and repetition times are assumed. Moreover other important imaging parameters such as FOV and number of averages (N) are chosen equivalent in both cases. Allowed current peak is also limited to 10mA.

Table 6.2 Gradient Echo and Spin Echo Parameters

Parameter	Gradient Echo	Spin Echo
α (Flip Angle)	90°	90°
T_E (Echo Time)	50ms	50ms
T_R (Repetition Time)	250ms	250ms
FOV (Field of View)	10cm	10cm
N (Number of Averages)	1	1
Thk (Slice Thickness)	5mm	5mm
I (Current Peak)	10mA	10mA
T_{rf} (RF pulse width)	3ms	3ms

Under these conditions, the question is to find current time (T_c). Before solving for T_c, since flip angle and other parameters are the same for both cases, signal expression in frequency domain are the same for both cases and signal in k-space is

expressed as in Equation (6.2). According to Equation (6.12.b), T_c for gradient echo is 32.3 ms, while for spin echo 30.3ms. If the same total current is the constraint on current injection, then gradient echo requires 9.38mA while spin echo requires 10mA. That means for these conditions, by using gradient echo total applied current could be decreased by 6.2%. Moreover, gradient echo gives the chance of making tradeoff between T_c and FOV as mentioned above. This could help researchers in terms of further increasing the length of current injection time or equivalently further decreasing applied current magnitude.

In the above example, T_R and T_E are assumed to be the same and T_2 is used for both spin echo and gradient echo. In gradient echo, instead of T_2, T_2^* weighting factor is used. Echo amplitude is related to T_E and T_2^* as

$$A_E \propto \exp(-\frac{T_E}{T_2^*}). \tag{6.15}$$

Myocardial T_2 is 52ms, while T_2^* is 68ms under 1.5T [69]. Then to keep echo amplitude the same, T_E should also be increased in the same order as 30.7%. For the above case, T_E of gradient echo should be 65.4ms. According to (12.b), T_c is found as 42.6ms. If the same total is the constraint on current injection, then gradient echo requires 7.1mA while spin echo requires 10mA. That means for these conditions, by using gradient echo total applied current could be decreased by 29%. In some cases T_2^* is smaller than T_2, that means, pulse sequence like in Figure 6.3 should be utilized. By this way echo amplitude is preserved and T_E is decreased. However in most of the cases $T_2^* > T_2$, then for most of the tissues above result is not valid.

Another important point is the signal averaging which makes system SNR better according to Equation (6.5). Taking N signal averages improves SNR by $\sqrt{N}$. Therefore when total imaging time period is fixed, then signal averaging as much as possible helps to have better reconstruction. In this case, decreasing echo time (T_E)

and repetition time (T_R) gains importance. At this point gradient echo has the advantage of having shorter echo and repetition times. Therefore more averages can be taken for gradient echo and SNR level could be further increased.

Spin echo and gradient echo are utilized in MREIT with an 11T magnet experimentally by Sadleir *et al* [52]. 60mm homogeneous saline phantom is used. Repetition and echo times for spin echo are as 600 and 200ms respectively. For gradient echo, 300 and 14ms are used for T_E and T_R. Current injection times are 18ms for spin echo and 9ms for gradient echo. Numbers of averages are 1 for spin echo and 4 for gradient echo. SNR in the center is found as 76 and 151 for spin echo and gradient echo. Signal loss of SE is very high when going from center to the edges. On the other hand, GE has some ripples. Since most of the parameters are different and the experiment is just conveyed for single case, concluding SE or GE is superior to the other is not possible. Besides, this experiment shows us GE could also be used in MREIT.

6.4.   Discussion

In this chapter, the Gradient Echo (GE) and Spin Echo (SE) based MREIT pulse sequences are analysed and compared to minimise the applied current amplitude. Current amplitude can be reduced towards safe levels by increasing the duration of current. When all conditions are assumed to be the same for GE and SE, using GE provides 6.2% decrement in current amplitude. When the affect of T_2^* is taken into account, the current amplitude is decreased by %29 in GE. These results encourage usage of GE based pulse sequences in MREIT. Further current minimization could be achieved as proposed in Figure 6.3. By this way, even smaller currents could be obtained. However, by this way sharp gradient changes could occur, that cause eddy currents in the body that is not desirable in real applications.

For the smallest possible amplitude of injected current, current could be injected throughout the echo time. That means current injection period should also cover slice selection and read-out periods. However, in this case, current is applied at the

expense of geometric distortion. This is equally valid for GE and SE pulse sequences.

For a given $T_E - T_R$ pair, current injection duration (T_C) is extended as much as possible and to minimize the current amplitude. Then, for a fixed imaging time, $T_E - T_R$ pair is reduced as much as possible to increase number of averages (N) for an improved SNR. Comparison of SE and GE based on these criteria is summarized in Table 6.3.

SE and GE contain their own advantages for MREIT. In this Chapter, we have analytically showed that GE is also a serious alternative to SE for MREIT techniques. GE was employed in MREIT just a few studies. However, GE usage in MREIT lacks serious experiments to observe its performance.

Table 6.3 Comparison of Gradient Echo and Spin Echo for MREIT

	SE	GE
Signal Expression (in time domain)	$S(t) = \iint M(x,y) e^{j\delta(x,y)} e^{j\gamma B_z(x,y)T_c} e^{-j\gamma G_y ty} e^{-j(\gamma\int_0^t G_x dt')x} \, dxdy$	$S(t) = \iint M(x,y) e^{j\delta(x,y)} e^{j\gamma B_z(x,y)T_c} e^{-j\gamma G_y ty} e^{-j(\gamma\int_0^t G_x dt')x} \, dxdy$
Signal Expression (in k-space)	$S(k_x,k_y) = \iint M(x,y) e^{j\delta(x,y)} e^{j\gamma B_z(x,y)T_c} e^{-j2\pi(k_x x + k_y y)} \, dxdy$	$S(k_x,k_y) = \iint M(x,y) e^{j\delta(x,y)} e^{j\gamma B_z(x,y)T_c} e^{-j2\pi(k_x x + k_y y)} \, dxdy$
SNR	$SNR = \psi_s \Delta x \Delta y \Delta z \sqrt{NT_s}\, M(x,y)$	$SNR = \psi_s \Delta x \Delta y \Delta z \sqrt{NT_s}\, M(x,y)$
Standard deviation of measured magnetic flux density	$\sigma_B = \dfrac{1}{\sqrt{2}\gamma T_c SNR}$	$\sigma_B = \dfrac{1}{\sqrt{2}\gamma T_c SNR}$
Optimum current injection time interval	$T_c^* = \dfrac{2}{3}(T_E - \dfrac{3}{2}T_{rf})$ The Interval begins just after the slice selection gradient and ends just before read-out gradient. Refocusing pulse period is excluded.	$T_c^* = \dfrac{2}{3}(T_E - \dfrac{1}{2}T_{rf})$ The Interval begins just after the slice selection gradient and ends just before read-out gradient.
Advantages for current injection optimization	• Utilization of T_2 makes T_E longer, then longer T_C could be obtained. • A new approach for increasing current injection duration was proposed based on extending current injection to the end of data acquisition under the name of Injection Current Nonlinear Encoding (ICNE) [57]. Extending current injection in this way helps to inject lower currents. • A lot of MREIT algorithms utilized SE, they produced reasonable results. Experience on SE for MREIT is much higher than GE for MREIT.	• Since there is no refocusing gradient, this time period is also included in the current injection interval. • Utilization of T_2^* lets T_E be shorter. Shorter T_E helps to have more signal averaging for a fixed imaging time period and hence better system SNR. • By changing the shape of the gradient as in figure 3, total current injection time can be extended without distorting T_E. • If GE is accepted as an alternative way of current injection in MREIT, then other fast echo sequences could also be applied.

CHAPTER 7

CONCLUSION

7.1. Summary and Conclusions

In this thesis, optimum current injection strategy for Magnetic Resonance Electrical Impedance (MREIT) is studied. As the first step, distinguishability measure based on measured magnetic flux density is defined for MREIT. Since conductivity distributions are reconstructed using magnetic flux density induced by current flow. Two conductivity distributions namely σ_1 and σ_2 are distinguishable with precision ε iff:

$$\left\| \vec{B}(\bullet, \sigma_1, j) - \vec{B}(\bullet, \sigma_2, j) \right\| > \varepsilon . \tag{7.1}$$

This is a general definition and can be applied to 2-D geometries as well as 3-D ones. The background idea behind such distinguishability is the presence of an inhomogeneity causes a change in conductivity distribution and also measured magnetic flux density. If this change is measurable (change in the magnetic flux density is greater than the measurement precision), then MREIT system realizes the inhomogeneity.

As the second step, limit of distinguishability is analytically derived for infinitely long cylinder with concentric inhomogeneity. This limit is compared with the limit based on surface potential (in EIT only surface potential values are measured). When distinguishability limits of MREIT and Electrical Impedance Tomography (EIT) are compared, it is found that MREIT is capable of detecting smaller perturbations than EIT. When conductivities of inhomogeneity and background object are equal to 0.8S and 1S respectively, MREIT provides improvement of %74

in detection capacity. That means MREIT is capable of detecting smaller inhomogeneities inside a body than EIT can do. This outcome is expected, since MREIT collects measurements from all over the field of view whereas EIT collects only surface potential measurements. Analytical distinguishability limit expression is obtained for infinitely long cylinder with eccentric inhomogeneity.

The third step is to find optimum current injection pattern. In this optimization problem, total distinguishability is maximized whereas total injected current is kept constant. For 2-D cylindrical body with concentric inhomogeneity, current injection pattern converges to opposite drive with impulsive current. However, practically impulsive current density could be harmful to the living organism. Hence, it should be approximated as far as the current injection pattern stays within the safety limits. This optimization problem is solved for eccentric geometry as well. In this case, optimum electrode pattern is again opposite with the drive axis passing through the centre of the perturbation. Other optimum electrode geometry is adjacent-like drive. Adjacent-like drive should be applied nearest point of inhomogeneity. By this way, maximum amount of current passes over the inhomogeneity. This condition increases the probability of detecting presence of inhomogeneity.

As the fourth step, distinguishability and current injection optimization are carried to 3-D with a sphere and centrally located inhomogeneity. In order to obtain analytical solution, azimuthal symmetry is assumed. Analytical expression for distinguishability limit is derived. Optimum current injection pattern is again opposite drive.

As the fifth step, above results are summarized as current injection principles
  i.   inject current with opposite drive
  ii.   inject current with small electrodes
  iii. inject current such that drive axis passing through the center of inhomogeneity
Based on these principles Regional Image Reconstruction (RIR) is proposed. In brief, it states that conductivity distribution should be reconstructed for a region

rather than for the whole body. This approach is applied to Equipotential Projection-Based MREIT. When there is no noise applying RIR makes any sense. However, when there is noise RIR provides smaller errors especially in inhomogeneities. For the square geometry, when SNR is 13dB, RIR provides decrement of nearly %50 in conductivity error rate of small inhomogeneity. Therefore this could be helpful to reconstruct perturbations inside a body. Another advantage of RIR is that it is independent of MREIT technique; therefore any MREIT technique can use RIR to provide better inhomogeneity detection.

As the sixth and the last step, pulse sequence optimization is considered. Since injected current in MREIT is part of the pulse sequence therefore optimizing pulse sequence could help MREIT techniques to inject smaller currents. Pulse sequence optimization is done for Gradient Echo (GE) and optimum current injection interval is determined. Gradient Echo and Spin Echo are compared in terms of their advantages in MREIT. On one side, a lot of MREIT algorithms utilized SE, they produced reasonable results. Experience on SE for MREIT is much higher than GE for MREIT. On the other side, there is no refocusing gradient in GE, this time period is also included in the current injection interval. If GE is accepted as an alternative way of current injection in MREIT, then other fast echo sequences could also be applied.

7.2. Future Work

- Regional Image Reconstruction technique and current injection principles could be applied in real experiments and their performance could be observed.
- There is no serious analysis on GE usage in MREIT. Based on the optimum GE pulse sequence for MREIT, experimental performance of GE in MREIT could be analyzed.

REFERENCES

[1]   A. D. Seager, D. C. Barber and B. H. Brown, "Electrical Impedance Imaging," *IEE Pro,* vol. 134 pp.201-210, 1987.

[2]   D. Isaacson, "Distinguishability of conductivities by electric current computed tomography," *IEEE Trans. Med. Imaging,* vol. 5 pp. 91–95, 1986.

[3]   J. C. Newell, D. G. Gisser and D. Isaacson, "An electric current tomography," *IEEE Trans. Biomed. Eng,* vol. BME-35 pp. 828-833, 1988.

[4]   D. G. Gisser, D. Isaacson and J. C. Newell, "Current topics in impedance imaging," *Clin. Phys. Physiol. Meas. & Suppl,* vol. A, pp. 39-46, 1987.

[5]   D. G. Gisser, D. Isaacson and J. C. Newell, "Theory and performance of an adaptive current tomography system," *Clin. Phys. Physiol. Meas,* vol. 9, pp. A35−A41, 1988.

[6]   N. Zhang, "Electrical impedance tomography based on current density imaging," *MSc Thesis,* University of Toronto, Canada, 1992.

[7]   E. J. Woo, S. Y. Lee and C. W. Mun, "Impedance tomography using internal current density distribution measured by nuclear magnetic resonance," *Proc. SPIE* vol. 2299, pp. *377–85,* 1994.

[8]   B. M. Eyüboğlu, R. Reddy and J. S. Leigh, "Magnetic resonance electrical impedance tomography," *Patent* US6,397,095 B1, provisional patent application on 1 Mar 1999, 2002.

[9]   O. Kwon, E. J. Woo, J. R. Yoon and J. K. Seo, "Magnetic resonance electrical impedance tomography (mreit): Simulation study of *j*-substitution algorithm," *IEEE Trans. Biomed. Eng,* vol. 49, pp. 160–167, 2002.

[10] Ö. Birgül, B. M. Eyüboğlu and Y. Z. İder, "Current constrained voltage scaled reconstruction (CCVSR) algorithm for MREIT and its performance with different probing current patterns," *Phys. Med. Biol,* vol. 48, pp. 653-671, 2003.

[11] M. Cheney and D. Isaacson, "Distinguishability in impedance imaging," *IEEE Trans. Biomed. Eng,* vol. 39, pp. 852–860, 1992.

[12] B. M. Eyüboğlu and T. C. Pilkington, "Comments on distinguishability in electrical impedance tomography," *IEEE Trans. Biomed. Eng,* vol. 40, pp. 328–330, 1993.

[13] R. J. Lytle, A. G. Duba and J. L. Willows, "Alternative methods for determining the electrical conductivity of core samples," *Rev. Sci. Instrum,* vol. 50, pp. 611-615, 1979.

[14] R. J. Lytle, "Alternative methods for determining the electrical conductivity of core samples. II," *Rev. Sci. Instrum,* vol. 54, pp. 871-874, 1983.

[15] N. G. Gençer, Y. Z. İder and S. J. Williamson, "Electrical impedance tomography: Induced-current imaging achieved with a multiple coil system," *IEEE Trans. Biomed. Eng,* vol. 43, pp.139–149, 1996.

[16] O. Kwon, J. R. Yoon, J. K. Seo, E. J. Woo and Y. G. Cho, "Estimation of anomaly location and size using electrical impedance tomography," *IEEE Trans. Biomed. Eng,* vol. 50, pp. 89-96, 2003.

[17] R. Plonsey and D. G. Fleming, *Bioelectric Phenomena*, McGraw Hill Press, 1969.

[18] I. L. Freeston and R. C. Tozer, "Impedance imaging using induced currents," *Physiol. Meas,* vol. 16, pp. A257–A266, 1995.

[19] B. M. Eyüboğlu, A. Köksal and B. M. Demirbilek, "Distinguishability analysis of an induced current EIT system using discrete coils," *Phys. Med. Biol*, vol. 45, pp. 1997–2009, 2000.

[20] A. Köksal, B. M. Eyüboğlu and M. Demirbilek, "A quasi-static analysis for a class of induced-current EIT systems using discrete coils," *IEEE Trans. Med. Imaging,* vol. 21, pp. 688–694, 2002.

[21] M. J. Van Burik and M. J. Peters, "Estimation of the electric conductivity from scalp measurements: Feasibility and application to source localization," *Clin. Neurophysiol,* vol. 111, pp. 1514–1521, 2000.

[22] B. M. Eyüboğlu, T. C. Pilkington and R. D. Wolf, "Estimation of tissue resistivity from multiple-electrode impedance measurements," *Phys. Med. Biol,* vol. 39, pp 1-17, 1994.

[23] B. M. Eyüboğlu and U. Baysal, "Incorporating a-priori information in EIT," *IEEE-EMBC and CMBEC,* pp. 565-566, 1995.

[24] T. J. Yorkey, J. G. Webster and W. J. Tompkins, "Comparing reconstruction algorithms for electrical impedance tomography," *IEEE Trans. Biomed. Eng,* vol. 34, pp. 843-852, 1987.

[25] S. G. Webster, *Electrical impedance tomography,* Adam Hilger Press Bristol UK, 1990.

[26] A. D. Seager, "Probing with low frequency electric currents," *Ph.D. Thesis,* University of Canterbury, 1983.

[27] C. C. Bacrie and R. Guardo, "Regularized reconstruction in electrical impedance tomography using a variance uniformization constraint," *IEEE Trans. Med. Imag,* vol. 16, pp. 562-571, 1987.

[28] G. C. Scott, M. L. G. Joy, R. L. Armstrong and R. M. Hankelman, "Measurement of non-uniform current density by magnetic resonance," *IEEE Trans. Med. Imaging,* vol. 10, pp. 362–74, 1991.

[29] J. K. Seo, J. R. Yoon, E. J. Woo and O. Kwon, "Reconstruction of conductivity and current density images using only one component of magnetic field measurements," *IEEE Trans. Biomed. Eng,* vol. 50, pp. 1121-1124, 2003.

[30] Ö. Birgül, B. M. Eyüboğlu and Y. Z. İder, "Experimental results for 2D magnetic resonance electrical impedance tomography (MREIT) using magnetic flux density in one direction," *Phys. Med. Biol,* vol. 48, pp. 3485-3504, 2003.

[31] B. M. Eyüboğlu, R. Reddy and J. S. Leigh, "Measurement of electric current density with magnetic resonance imaging," 1997.

[32] B. M. Eyüboğlu, R. Reddy and J. S. Leigh, "Imaging electrical current density using nuclear magnetic resonance," *Elektrik Turkish J. Electr. Eng. Comput. Sci,* vol. 6, pp. 201–14, 1998.

[33] H. S. Khang, B. I. Lee, S. H. Oh, E. J. Woo, S. Y. Lee, M. H. Cho, O. Kwon, J. R. Yoon and J. K. Seo, "J-substitution algorithm in magnetic resonance electrical impedance tomography (mreit): phantom experiments for static resistivity images," *IEEE Trans. Med. Imaging,* vol. 21, pp. 695–702, 2002.

[34] Y. Z. İder and Ö. Birgül, "Use of magnetic field generated by the internal distribution of injected currents for electrical impedance tomography," *Elektrik Turkish J. Elect. Eng. Comp. Sci,* vol. 6, pp. 215-225, 1998.

[35] Ö. Birgül, O. Özbek, B. M. Eyüboğlu and Y. Z. İder, "Magnetic resonance conductivity imaging using 0.15 tesla MRI scanner," *Proc. IEEE EMBS Conf. CD-ROM,* 2001.

[36] Ö. Birgül, B. M. Eyüboğlu and Y. Z. İder, "Magnetic resonance conductivity imaging," *Proc. IEEE EMBS Conf.(Atlanta, USA),* pp. 1127, 1999.

[37] Ö. Birgül, B. M. Eyüboğlu and Y. Z. İder, "New technique for high resolution absolute conductivity imaging using magnetic resonance electrical impedance tomography (MREIT)," *SPIE Phys. Med. Imaging,* vol. 2, pp. 880–8, 2001.

[38] B. M. Eyüboğlu, Ö. Birgül and Y. Z. İder, "Magnetic resonance electrical impedance tomography (MREIT): a new technique for high resolution conductivity imaging," *2nd EPSRC Engineering Network Meeting: Biomedical Applications of EIT (University College, London),* 2000.

[39] B. M. Eyüboğlu, Ö. Birgül and Y. Z. İder, "A dual modality system for high resolution-true conductivity imaging," *XI Int. Conf. on Electrical Bio-Impedance (Oslo, Norway),* pp 409–13, 2001.

[40] M. Özdemir and B. M. Eyüboğlu, "Novel fast reconstruction algorithm for magnetic resonance electrical impedance tomography," *Proc. Biyomut 8th Annual Conf. (CD-ROM) (Istanbul, Turkey),* 2002.

[41] O. Kwon, J. Y. Lee and J. R. Yoon, "Equipotential line method for magnetic resonance electrical impedance tomography," *Inverse Prob,* vol. 18, pp. 1089–1100, 2002.

[42] O. Özbek, Ö. Birgül, B. M. Eyüboğlu and Y. Z. İder, "Imaging electrical current density using 0.15 tesla magnetic resonance imaging system," *Proc. IEEE EMBS 23th Annual Conf. CD-ROM (Istanbul, Turkey),* 2001.

[43] G. C. Scott, M. L. G. Joy, R. L. Armstrong and R. M. Hankelman, "Rotating frame rf current density imaging," *Magn. Reson. Med,* vol. 33, pp. 355–369, 1995.

[44] Y. Z. İder and L. T. Müftüler, "Use of mri for measuring ac internal currents of eit: a feasibility study," *Proc. IXth Int. Conf. on Electrical Bio-Impedance,* pp 420–422, 1995.

[45] Y. Z. İder and L. T. Müftüler, "Measurement of ac magnetic field distribution using magnetic resonance imaging," *IEEE Trans. Med. Imaging,* vol.16, pp. 617–622, 1997.

[46] Y. Z. İder, S. Onart and W. R. B. Lionheart, "Uniqueness and reconstruction in magnetic resonance electrical impedance tomography (MREIT)," *Phys. Meas,* vol. 24, pp. 591-604, 2003.

[47] C. Park, O. Kwon, E. J. Woo and J. K. Seo, "Electrical conductivity imaging using gradient Bz decomposition algorithm in magnetic resonance electrical impedance tomography (MREIT)," *IEEE Trans. Med. Imag,* vol. 23, pp. 388-394, 2004.

[48] M. S. Özdemir, B. M. Eyüboğlu and O. Özbek, "Equipotential projection-based magnetic resonance electrical impedance tomography and experimental realization," *Phys. Med. Biol,* vol. 49, pp. 4765-4783, 2004.

[49] N. Gao, S. A. Zhu and B. A. He, "New magnetic resonance electrical impedance tomography (MREIT) algorithm: the RSM-MREIT algorithm with applications to estimation of human head conductivity," *Phys. Med. Biol,* vol. 51, pp. 3067-3083, 2006.

[50] Ö. Birgül, M. J. Hamamura, L. T. Müftüler and O. Nalcıoğlu, "Contrast and spatial resolution in MREIT using low amplitude current," *Phys. Med. Biol,* vol. 51, pp. 5035-5049, 2006.

[51] R. Sadleir, S. Grant, S. U. Zhang, B. I. Lee, H. C. Pyo, S. H. Oh, C. Park, E. J. Woo, S. Y. Lee, O. Kwon and J. K. Seo, "Noise analysis in magnetic resonance electrical impedance tomography at 3 and 11 T field strengths," *Physiol. Meas,* vol. 26, pp. 875-884, 2005.

[52] R. Sadleir, S. Grant, S. U. Zhang, S. H. Oh, B. I. Lee and E. J. Woo, "High field MREIT: setup and tissue phantom imaging at 11T," *Physiol. Meas,* vol. 27, pp. S261-S270, 2006.

[53] M. Joy, G. C. Scott and R. M. Henkelman, "In vivo detection of applied electric currents by magnetic resonance imaging," *Mag. Res. Imaging,* vol. 7, pp. 89-94, 1989.

[54] U. Mikac, F. Demsar, K. Beravs and I. Sersa, "Magnetic resonance imaging of alternating electric currents," *Magn. Reson. Imaging,* vol. 19, pp.845-856, 2001.

[55] G. C. Scott, N. L. G. Joy, R. L. Armstrong and R. M. Henkelman, "Sensitivity of magnetic resonance current density imaging," *J. Magn. Reson,* vol. 97, pp. 235-254, 1992.

[56] B. I. Lee, C. Park, H. C. Pyo, O. Kwon and E. J. Woo, "Optimization of current injection pulse width in MREIT," *Physiol. Meas,* vol. 28, pp. N1-N7, 2007.

[57] C. Park, B. I. Lee, O. Kwon and E. J. Woo, "Measurement of induced magnetic flux density using injection current nonlinear encoding (ICNE) in MREIT," *Physiol. Meas,* vol. 28, pp. 117-127, 2007.

[58] O. Kwon, B. I. Lee, H. S. Nam and C. Park, "Noise analysis and MR pulse sequence optimization in MREIT using an injected current nonlinear encoding (ICNE) method," *Physiol. Meas,* vol. 28, pp.1391-1404, 2007.

[59] A. Köksal and B. M. Eyüboğlu, "Determination of optimum injected current pattern in electrical impedance tomography," *Physiol. Meas,* pp. A99-109, 1995.

[60] W. R. B. Lionheart, J. Kaipio and C. N. McLead, "Generalized optimal current patterns and electrical safety in EIT," *Physiol. Meas,* vol. 22, no.1, pp. 85-90, 2001.

[61] Y. Z. İder and S. Onart, "Algebraic reconstruction for 3D magnetic resonance-electrical impedance tomography (MREIT) using one component of magnetic flux density," *Physiol. Meas*, vol. 25, pp. 281-91, 2004.

[62] E. J. Woo, J. K. Seo and S. Y. Lee, *Magnetic resonance electrical impedance tomography (MREIT) Electrical Impedance Tomography: Methods, History and Applications,* Bristol, UK: IOP Publishing, 2005.

[63] B. M. Eyüboğlu, "Magnetic Resonance – Electrical Impedance Tomography in WILEY Encyclopedia of Biomedical Engineering," vol. 4, pp. 2154-2162, 2006.

[64] H. Altunel, B. M. Eyüboğlu, A. Köksal, "Distinguishability for magnetic resonance electrical impedance tomography (MREIT)," *Phys. Med. Biol,* vol. 52, pp. 375-387, 2007.

[65] J. D. Jackson, *Classical Electrodynamics,* John Wiley & Sons, 1998.

[66] L. A. Shepp and B. F. Logan, "The fourier reconstruction of a head section," *IEEE Trans. Nucl. Sci.*, vol. NS-21, pp. 21-43, 1974.

[67] J. Paul, "The modeling of general electromagnetic materials in TLM," *Ph.D. Thesis*, The University of Nottingham, UK, 1998.

[68] Z. P. Liang and Lauterbur, *Principles of Magnetic Resonance Imaging (MRI):A signal processing perspective,* IEEE Press, New York, 1999.

[69] L. J. Anderson, S. Holden, B. Davis, E. Prescott, C. C. Charrier, N. H. Bunce, D. N. Firmin, B. Wonke, J. Porter, J. M. Walker and D. J. Pennell, "Cardiovascular T_2-star (T_2^*) magnetic resonance for the early diagnosis of myocardial iron overload," *Europ. Heart Jour,* vol. 22, pp. 2171-2179, 2001.

APPENDIX A

RELATION BETWEEN CURRENT DENSITY AND MAGNETIC FLUX DENSITY

For the problem mentioned above, following relation between current density and magnetic flux at a point holds

$$B_z(r,\theta) = \frac{\mu_0}{4\pi} \int \frac{J_r(r',\theta')r\sin(\theta-\theta') + J_\theta(r',\theta')(r'-r\cos(\theta-\theta'))}{R^3} ds'$$

This relation can be considered as the limit of the Riemann sum, as

$$B_{z_1} = \frac{\mu_0}{4\pi} \sum_{n=2}^{N} J_{r_n} f(p_1, p_n) + J_{\theta_n} g(p_1, p_n) \tag{A.1}$$

Where p_1 and p_n are the positions of observation and source point relatively. f and g are the position functions and contain the information of relative position of observation and source points. According to the above equation, for a specific observation point, different current density distributions could produce the same magnetic flux density value.

When all of the magnetic flux density values at all points are considered, the following matrix equation can be obtained:

$$
\begin{bmatrix} B_{z_1} \\ B_{z_2} \\ \vdots \\ B_{z_N} \end{bmatrix} = \begin{bmatrix} 0 & f(p_1,p_2) & \cdots & f(p_1,p_N) \\ f(p_2,p_1) & 0 & & \\ \vdots & & \ddots & \\ f(p_N,p_1) & \cdots & & 0 \end{bmatrix} \begin{bmatrix} J_{r_1} \\ J_{r_2} \\ \vdots \\ J_{r_N} \end{bmatrix}
$$

$$
+ \begin{bmatrix} 0 & g(p_1,p_2) & \cdots & g(p_1,p_N) \\ g(p_2,p_1) & 0 & & \\ \vdots & & \ddots & \\ g(p_N,p_1) & \cdots & & 0 \end{bmatrix} \begin{bmatrix} J_{\theta_1} \\ J_{\theta_2} \\ \vdots \\ J_{\theta_N} \end{bmatrix} \qquad (A.2)
$$

in short it can be shown as

$$\mathbf{b} = \mathbf{F.j_r} + \mathbf{G.j} \qquad (A.3)$$

Each element in **F** and **G** matrices contain the position information between different points. The diagonal elements are taken as zero; because at diagonal entries the points of observation and source are the same and the effect of current density on itself is neglected.

F and **G** matrices are non-singular. Therefore when there is a current distribution, then there is only one solution of **b** vector and that means only one magnetic flux distribution.

APPENDIX B

MAGNETIC FLUX DENSITY ON THE SINGULARITY POINT

The small circular region where the center is the observation point is excluded from the magnetic flux density calculation. When uniform current is assumed, the magnetic flux density at the center of the small circular region could be determined by utilizing two different approaches.

In the first approach, magnetic flux density is determined by using Biot-Savart law. The small region can be zoomed to analyze more closely as in Figure B.1.
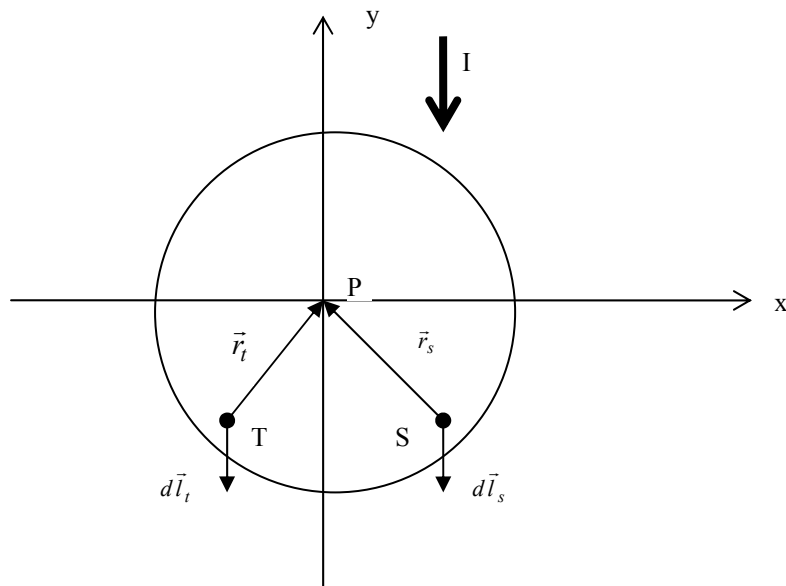
Figure B.1. Inside the singularity region.

Let current to flow in negative y direction. Consider a point S and due to the current flow at this point magnetic flux density is created at the center point, namely P which is actually the observation point. Magnetic flux density created by S is expressed as

$$d\vec{B}_s = \frac{\mu_0}{4\pi} \frac{Id\vec{l}_s \times \vec{r}_s}{|\vec{r}_s|^3} \tag{B.1}$$

$d\vec{B}_s$ is in z direction and its magnitude is expressed as

$$\left|d\vec{B}_s\right| = \frac{\mu_0}{4\pi} \frac{I\left|d\vec{l}_s\right|\left|\vec{r}_s\right|\sin\alpha}{|\vec{r}_s|^3} \tag{B.2}$$

where α is the angle between $d\vec{l}_s$ and $\vec{r}_s$.

There exists a T point that is symmetric of S with respect to y axis. It also creates magnetic flux density at the center point given by

$$d\vec{B}_t = \frac{\mu_0}{4\pi} \frac{Id\vec{l}_t \times \vec{r}_t}{|\vec{r}_t|^3}$$

The magnitude of $d\vec{B}_t$ can be expressed as

$$\left|d\vec{B}_t\right| = \frac{\mu_0}{4\pi} \frac{I\left|d\vec{l}_t\right|\left|\vec{r}_t\right|\sin(2\pi-\alpha)}{|\vec{r}_t|^3} . \tag{B.3}$$

Since S and T are symmetric points the magnitudes of $d\vec{l}$ and $\vec{r}$ vectors are the same. Only different term is sin terms. On the other hand it is known that

$$\sin(2\pi - \alpha) = -\sin\alpha .$$

Therefore T creates magnetic flux density which is equal to the one created by S, however in the opposite direction. Thus these two terms cancel each other. Therefore magnetic flux density created by the right hand side points is canceled by the magnetic flux density created by the left hand side points in this infinitesimally small uniform current density region.

There remain only the points on the y axis. Since $d\vec{l}$ and $\vec{r}$ vectors are parallel for these points. Due to the cross product feature, they are not able to create magnetic

flux density at P. Hence, in the disc shown in Figure B.1, total magnetic flux density created by all points except for P on P is zero. There remains only the effect of point P on itself. Instead of a direct mathematical expression of this effect, it is rather shown as a limit.

Consider a circle with radius r_P and its center is P as shown in Figure B.2. The magnetic flux density of P on itself is the limit of total magnetic flux density created by the points on the circle while r_P goes to zero.
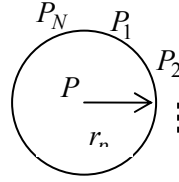
Figure B.2. Near the singularity point.

$$\vec{B}_P = \lim_{r_P \to 0} \sum_{i=1}^{N} \vec{B}_{P_i} = \lim_{r_P \to 0} \sum_{i=1}^{N} \frac{\mu_0}{4\pi} \frac{I d\vec{l} \times \vec{r}_{p_i}}{\left|r_p\right|^3} \tag{B.4}$$

$$\vec{B}_P = \lim_{r_P \to 0} \frac{\mu_0 I}{4\pi} \left(\frac{d\vec{l} \times \vec{r}_{p_1} + d\vec{l} \times \vec{r}_{p_2} + \ldots + d\vec{l} \times \vec{r}_{p_N}}{\left|r_p\right|^3} \right) \tag{B.5}$$

Due to the cancellation effects of symmetrical points, the sum of cross product terms in parenthesis is zero independent of $\left|r_p\right|$ value. Hence when the current is uniform, the magnetic flux density of P on itself converges to zero.

In the second approach vector magnetic potential is used to determine the magnetic flux density at the center. Vector magnetic potential for this problem is represented as

$$\vec{A} = \frac{\mu_0}{4\pi} \int_s \frac{\vec{J}}{R} ds$$

Consider a random P' point inside the source region as in Figure B.3. Since there is only current component flowing in the $-y$ direction, there exists only y component of vector magnetic potential as

$$A_y(r',\theta') = \frac{\mu_0 I}{4\pi} \int_S \frac{1}{\left(r^2 + r'^2 - 2rr'\cos(\theta-\theta') \right)^{\frac{1}{2}}} r\,dr\,d\theta \qquad (B.6)$$
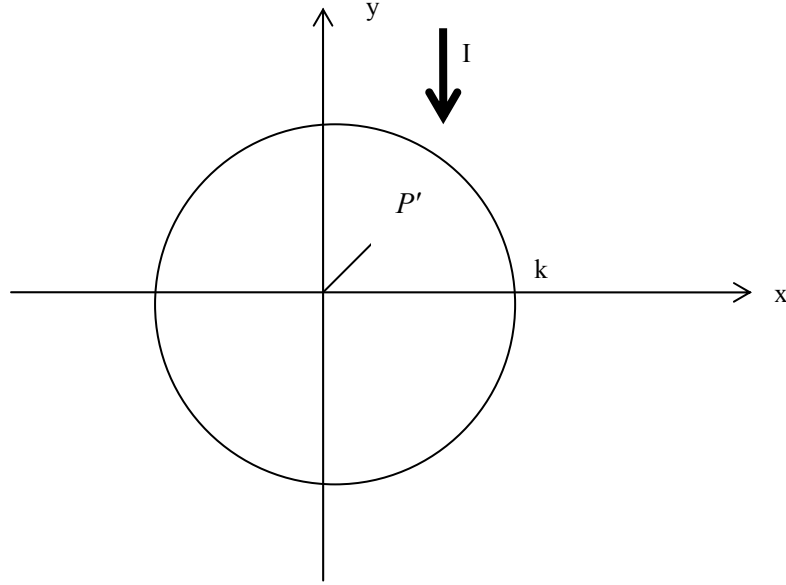
Figure B.3. A random point $P'(r',\theta')$ inside the singularity region.

$$A_y(r',\theta') = \frac{\mu_0 I}{4\pi} \int_{-\pi}^{\pi}\int_0^k \frac{1}{\left(r^2 + r'^2 - 2rr'\cos(\theta-\theta')\right)^{\frac{1}{2}}} r\,dr\,d\theta \qquad (B.7)$$

The integral can be re-written as

$$A_y(r',\theta') = \frac{\mu_0 I}{4\pi} \int_{-\pi}^{\pi}\int_0^k \frac{1}{\left((r+c)^2 + d^2\right)^{\frac{1}{2}}} r\,dr\,d\theta \qquad (B.8)$$

where

$$c = -r'\cos(\theta-\theta')$$

$$d = \mp r'\sin(\theta-\theta')$$

By change of variables, the integral turns into the following form

$$A_y(r',\theta') = \frac{\mu_0 I}{4\pi} \int_{-\pi}^{\pi} \int_{\arctan(\frac{c}{d})}^{\arctan(\frac{k+c}{d})} (d\tan\alpha\sec\alpha - c\sec\alpha)\,d\alpha\,d\theta \qquad (B.9)$$

When the inner integral is solved and the values of c and d are substituted, following expression for the vector magnetic potential of a given point inside the source region is obtained

$$A_y(r',\theta) =$$

$$\frac{\mu_0 I}{4\pi} \int_{-\pi}^{\pi} \left[\left(k^2 - 2kr'\cos(\theta-\theta') + r'^2\right)^{\frac{1}{2}} - r' - r'\cos(\theta-\theta')\ln\frac{r'-r'\cos(\theta-\theta')}{\left(k^2 - 2kr'\cos(\theta-\theta')+r'^2\right)^{\frac{1}{2}} + k - r'\cos(\theta-\theta')} \right] d\theta$$

$$(B.10)$$

On the other hand it is known that

$$\vec{B} = \nabla \times \vec{A} = \begin{vmatrix} \vec{a}_x & \vec{a}_y & \vec{a}_z \\ \dfrac{\partial}{\partial x} & \dfrac{\partial}{\partial y} & \dfrac{\partial}{\partial z} \\ A_x & A_y & A_z \end{vmatrix} \qquad (B.11)$$
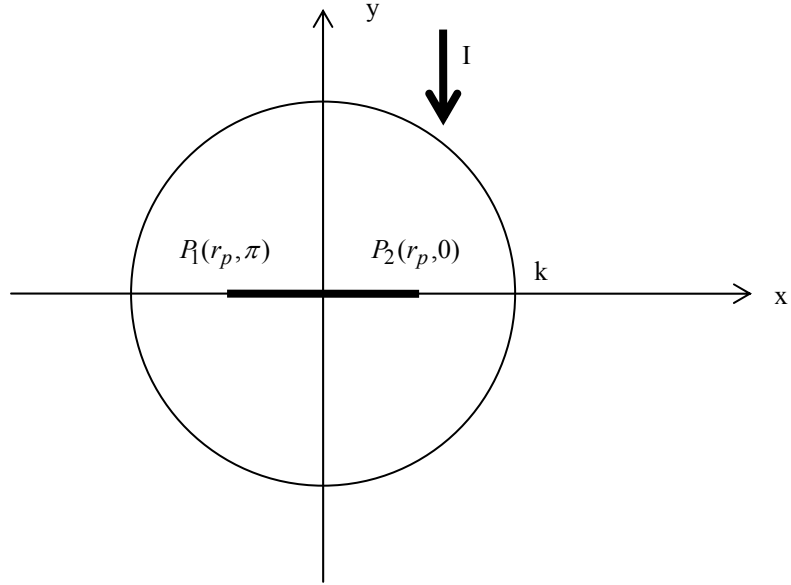
and only $B_z\vec{a}_z$ is required

$$B_z = \frac{\partial A_y}{\partial x} - \frac{\partial A_x}{\partial y} \qquad (B.12)$$

In this case $A_x = 0$, therefore

$$B_z = \frac{\partial A_y}{\partial x} \qquad (B.13)$$

The point of interest is the center point, hence magnetic flux density at the center is the interest, namely $B_z(0,0)$ is required. To formulate the magnetic flux density as the partial derivative of vector magnetic potential, consider two points P_1 and P_2 as in Figure B.4. Then,

Figure B.4. Derivative points of vector magnetic potential with respect to x-axis.

$$B_z(0,0) = \lim_{r_p \to 0} \frac{A_y(P_2) - A_y(P_1)}{2r_p} \qquad (B.14)$$

where

$$A_y(P_2) =$$

$$\frac{\mu_0 I}{4\pi} \int_{-\pi}^{\pi} \left[\left(k^2 + 2kr_p\cos\theta + r_p^2\right)^{\frac{1}{2}} - r_p + r_p\cos\theta\ln\frac{r_p + r_p\cos\theta}{\left(k^2 + 2kr_p\cos\theta + r_p^2\right)^{\frac{1}{2}} + k + r_p\cos\theta} \right] d\theta$$

$$(B.15.a)$$

and

$$A_y(P_1) =$$

$$\frac{\mu_0 I}{4\pi} \int_{-\pi}^{\pi} \left[\left(k^2 - 2kr_p\cos\theta + r_p^2\right)^{\frac{1}{2}} - r_p - r_p\cos\theta\ln\frac{r_p - r_p\cos\theta}{\left(k^2 - 2kr_p\cos\theta + r_p^2\right)^{\frac{1}{2}} + k - r_p\cos\theta} \right] d\theta$$

$$(B.15.b)$$

103

$$B_z(0,0) =$$

$$\lim_{r_p \to 0} \frac{\mu_0 I}{4\pi} \int_{-\pi}^{\pi} \left[\frac{\left(k^2 + 2kr_p\cos\theta + r_p{}^2\right)^{\frac{1}{2}} - \left(k^2 - 2kr_p\cos\theta + r_p{}^2\right)^{\frac{1}{2}}}{2r_p} + \right.$$

$$\left. \frac{\cos\theta}{2} \ln \frac{\left(r_p + r_p\cos\theta\right)\left(r_p - r_p\cos\theta\right)}{\left[\left(k^2 + 2kr_p\cos\theta + r_p{}^2\right)^{\frac{1}{2}} + k + r_p\cos\theta\right]\left[\left(k^2 - 2kr_p\cos\theta + r_p{}^2\right)^{\frac{1}{2}} + k - r_p\cos\theta\right]} \right] d\theta$$

(B.16)

Now, divide the integral into two parts:

$$B_z(0,0) =$$

$$\lim_{r_p \to 0} \frac{\mu_0 I}{4\pi} \int_{-\frac{\pi}{2}}^{\frac{\pi}{2}} \left[\frac{\left(k^2 + 2kr_p\cos\theta + r_p{}^2\right)^{\frac{1}{2}} - \left(k^2 - 2kr_p\cos\theta + r_p{}^2\right)^{\frac{1}{2}}}{2r_p} + \right.$$

$$\left. \frac{\cos\theta}{2} \ln \frac{\left(r_p + r_p\cos\theta\right)\left(r_p - r_p\cos\theta\right)}{\left[\left(k^2 + 2kr_p\cos\theta + r_p{}^2\right)^{\frac{1}{2}} + k + r_p\cos\theta\right]\left[\left(k^2 - 2kr_p\cos\theta + r_p{}^2\right)^{\frac{1}{2}} + k - r_p\cos\theta\right]} \right] d\theta$$

$$+$$

$$\lim_{r_p \to 0} \frac{\mu_0 I}{4\pi} \int_{\frac{\pi}{2}}^{\frac{3\pi}{2}} \left[\frac{\left(k^2 + 2kr_p\cos\theta + r_p{}^2\right)^{\frac{1}{2}} - \left(k^2 - 2kr_p\cos\theta + r_p{}^2\right)^{\frac{1}{2}}}{2r_p} + \right.$$

$$\left. \frac{\cos\theta}{2} \ln \frac{\left(r_p + r_p\cos\theta\right)\left(r_p - r_p\cos\theta\right)}{\left[\left(k^2 + 2kr_p\cos\theta + r_p{}^2\right)^{\frac{1}{2}} + k + r_p\cos\theta\right]\left[\left(k^2 - 2kr_p\cos\theta + r_p{}^2\right)^{\frac{1}{2}} + k - r_p\cos\theta\right]} \right] d\theta$$

(B.17)

By applying change of variables to the second part of integral as $\phi = \theta - \pi$ second integral turns into

$$\lim_{r_p \to 0} \frac{\mu_0 I}{4\pi} \int_{-\frac{\pi}{2}}^{\frac{\pi}{2}} \left[\frac{\left(k^2 - 2kr_p \cos\phi + r_p{}^2\right)^{\frac{1}{2}} - \left(k^2 + 2kr_p \cos\phi + r_p{}^2\right)^{\frac{1}{2}}}{2r_p} - \right.$$

$$\left. \frac{\cos\phi}{2} \ln \frac{\left(r_p - r_p \cos\phi\right)\left(r_p + r_p \cos\phi\right)}{\left[\left(k^2 - 2kr_p \cos\phi + r_p{}^2\right)^{\frac{1}{2}} + k - r_p \cos\phi\right]\left[\left(k^2 + 2kr_p \cos\phi + r_p{}^2\right)^{\frac{1}{2}} + k + r_p \cos\phi\right]} \right] d\phi$$

(B.18)

The terms in the second integral are the same as the terms in the first one, except for the multiplication of a minus (-) sign. Therefore sum of two integral terms is equal to zero independent of r_p, I, k (radius of the circle).

Hence

$$B_z(0,0) = \lim_{r_p \to 0} \frac{A_y(P_2) - A_y(P_1)}{2r_p} = \lim_{r_p \to 0} \frac{\mu_0 I}{4\pi} \left[\int_{-\frac{\pi}{2}}^{\frac{\pi}{2}} F(k, r_p, \theta) d\theta + \int_{-\frac{\pi}{2}}^{\frac{\pi}{2}} -F(k, r_p, \phi) d\phi \right] = 0$$

(B.19)

VITA

PERSONAL INFORMATION

Surname, Name: Altunel, Haluk Altunel

Nationality: Turkish (TC)

Date and Place of Birth: 29 March 1978, Konya

Marital Status: Single

Phone: +90 532 5974017

email: haluk_altunel@hotmail.com

EDUCATION

Degree	Institution	Year of Graduation
MS	Bilkent University Electrical and Electronics Eng.	2002
BS	Bilkent University Electrical and Electronics Eng.	1999
High School	Meram Science High School, Konya	1994

WORK EXPERIENCE

Year	Place	Enrollment
2004-Present	İşnet	Project Leader
2000-2003	Karel	Project Engineer
1999-2000	Bilkent University	Research Assistant

FOREIGN LANGUAGES

Advanced English, Advenced German, Basic Japanese

PUBLICATIONS DURING PH.D. STUDY

- **H. Altunel,** B. M. Eyüboğlu, A. Köksal, "Optimum Current Injection Pattern for Magnetic Resonance Electrical Impedance Tomography" in preparation.

- **H. Altunel,** B. M. Eyüboğlu, A. Köksal, "Current Injection Optimization for Magnetic Resonance Electrical Impedance Tomography (MREIT)," *13th International Conference on Electrical Bioimpedance and 8th Conference on Electrical Impedance Tomography, Graz-Austria,* pp. 504-507 and *IFBME Proceedings* vol. 17, DVD-ROM Springer-Verlag, 2007.

- **H. Altunel,** B. M. Eyüboğlu, A. Köksal, "Distinguishability for magnetic resonance electrical impedance tomography (MREIT)," *Phys. Med. Biol,* vol. 52, pp. 375-387, 2007.

- **H. Altunel,** B. M. Eyüboğlu, A. Köksal, "Manyetik rezonans elektrik empedans tomografisinde (MREIT) ayırt edilebilirlik," *Proc. 3. Scientific Congress of Union Radio Scientifique Turkey Division, Ankara, Turkey,* pp. 189-191, 2006.

- **H. Altunel,** B. M. Eyüboğlu and A. Köksal, "Distiguishability for Magnetic resonance electrical impedance tomography (MREIT)," *Proc. of 7th Conference on Biomedical Applications of Electrical Impedance Tomography, Joint Conference of World Congress on Medical Physics and Biomedical Engineering, Seoul – Korea,* pp.147-150 and *IFMBE Proceedings vol. 14, DVD-ROM Springer-Verlag ISBN 3-540-36839-6,* 2006.

PUBLICATIONS PRIOR TO PH.D. STUDY

- E. Sezer and **H. Altunel,** "Adaptive Decentralized Control of Interconnected Systems," *Dynamics of Continuous, Discrete and Impulsive Systems*, vol. 11, pp. 521-536, 2004.